A Study of Focused Ion Beam Micromachining by Development of a 3-D Computer Simulation and a 3-D Digital Scan Strategy

Hongyu Ximen
B.S., Peking University, Beijing, China, 1985

A dissertation submitted to the faculty
of the Oregon Graduate Institute of Science and Technology
in partial fulfillment of the
requirements for the degree
Doctor of Philosophy
in
Applied Physics

August, 1990

The dissertation "A Study of Focused Ion Beam Micromachining by Development of a 3-D Computer Simulation and a 3-D Digital Scan Strategy" by Hongyu Ximen has been examined and approved by the following Examination Committee:

Jonathan H. Orloff, Advisor
Professor

Richard K. DeFreez
Associate Professor

Anthony E. Bell
Research Associate Professor

Mark Utlaut
Professor, University of Portland

Joseph Puretz
FEI Corporation

Jiye Ximen
Professor, Peking University

To My Parents

ACKNOWLEDGEMENTS

I wish to express my deepest gratitude to my advisor, Dr. Jon Orloff, for his constant encouragement, direction and support during this dissertation research that has proved to be a most valuable thing to my life.

I also owe my debt of gratitude to Dr. Richard DeFreez for his valuable suggestions and support to expedite this dissertation, and for his vast knowledge and physical insight in science from which I have been greatly benefited.

Many thanks are due to Dr. Joseph Puretz for his critical review of this dissertation, and for his friendly understanding and useful discussion.

I would also like to acknowledge Drs. Bell and Utlaut for their comments and examinations of my dissertation.

I would like to dedicate this work to my parents. Their love, patience and support so far have proved to be a main source of the energy and belief in my academic career.

Finally I owe my deepest debt of appreciation to my friend Li Zhou for her help and concern.

Table of Contents

List of Figures

ABSTRACT

A Study of Focused Ion Beam Micromachining by Development of a 3-D Computer Simulation and a 3-D Digital Scan Strategy

Hongyu Ximen, Ph.D.

Oregon Graduate Institute, 1990

Supervising Professor: Jon H. Orloff

Focused ion beam micromachining (FIBM) is a technique capable of forming optical quality surfaces in semiconductor laser materials. A beam of 25 keV Ga^+ ions focused to a 50 to 250 nm spot has been used to sputter materials from wafer surfaces, providing a method for fabricating submicron features such as diode laser output mirrors and coupled cavity oscillator mirrors. To date, all mirrors fabricated by FIBM have been made up of lines or rectangles (i.e. fabricated by straight line scans) and complicated structures have been fabricated by various researchers, using straight line scans. However, straight line scans cannot satisfactorily be used for many kinds of applications.

In this dissertation, a fully-digitized, non-linear, three-dimensional (3-D) and variable-scan-speed scan strategy, which can produce arbitrarily curved structures, has been developed. This scan technique has been implemented by using a FIB system with an IBM-compatible computer to fabricate "V",

micro-"V" and parabolic turning mirrors in GaAs lasers. These turning mirrors could not be machined by connecting straight line segments because, at the junction of the line segments, redeposited material would fill up previously machined sections. When the first attempt at a parabolic mirror was initiated using an ion beam with constant scan speed (in the x or y direction), a mirror with a non-uniform depth profile was produced. Therefore, a strategy which produces constant scan speed along the arc was developed in order to fabricate curved mirrors with a uniform depth profile.

A simple computer simulation of FIBM in 3-D space, which is based upon an assumed Gaussian current distribution of an ion beam, has been developed to visualize the aforementioned 3-D structures. Experimental verifications of the computer simulation have been given. The aim of the 3-D simulation is to produce software support for computer controlled FIB micromachining of various structures on semiconductor materials at a submicron scale.

1. INTRODUCTION

This dissertation research involves a 3-dimensional (3-D) computer simulation of focused ion beam micromachining (FIBM), experimental verifications of the simulation, various examples of FIBM, and some preliminary investigates of focused ion beam induced damage. The computer simulation takes into account a Gaussian current distribution. The simulation also studies the effects of a defocused and astigmatic ion beam on micromachined structures. A 3-D digital ion beam scan strategy has been developed for fabricating various 3-D structures in semiconductor diode laser materials. The actual micromachining has been performed in an FIBM workstation consisting of a liquid metal ion source (LMIS) and an ion column, as shown schematically in Fig. 1.1.

The development of high brightness ion sources has grown very rapidly for the past two decades. Among various types of ion sources[1], such as high-current gaseous ion sources, Philips-Ionization-Gauge (PIG) ion sources, Freeman ion sources, Electron Cyclotron Resonance (ECR) ion sources, microwave ion sources, electron beam ion sources, beam-plasma ion sources, laser ion sources, metal vapor vacuum arc ion sources, and negative ion sources, the liquid metal ion sources (LMIS)[2-10] are unique as they can be easily fabricated, and can produce high current density and finely focused ion beam.

As shown in Fig. 1.1, a typical ion column that consists of a three-cylinder asymmetric einzel lens and an octopole stigmator/deflector[11,12] is very much analogous to a series of optical lenses which may focus light rays

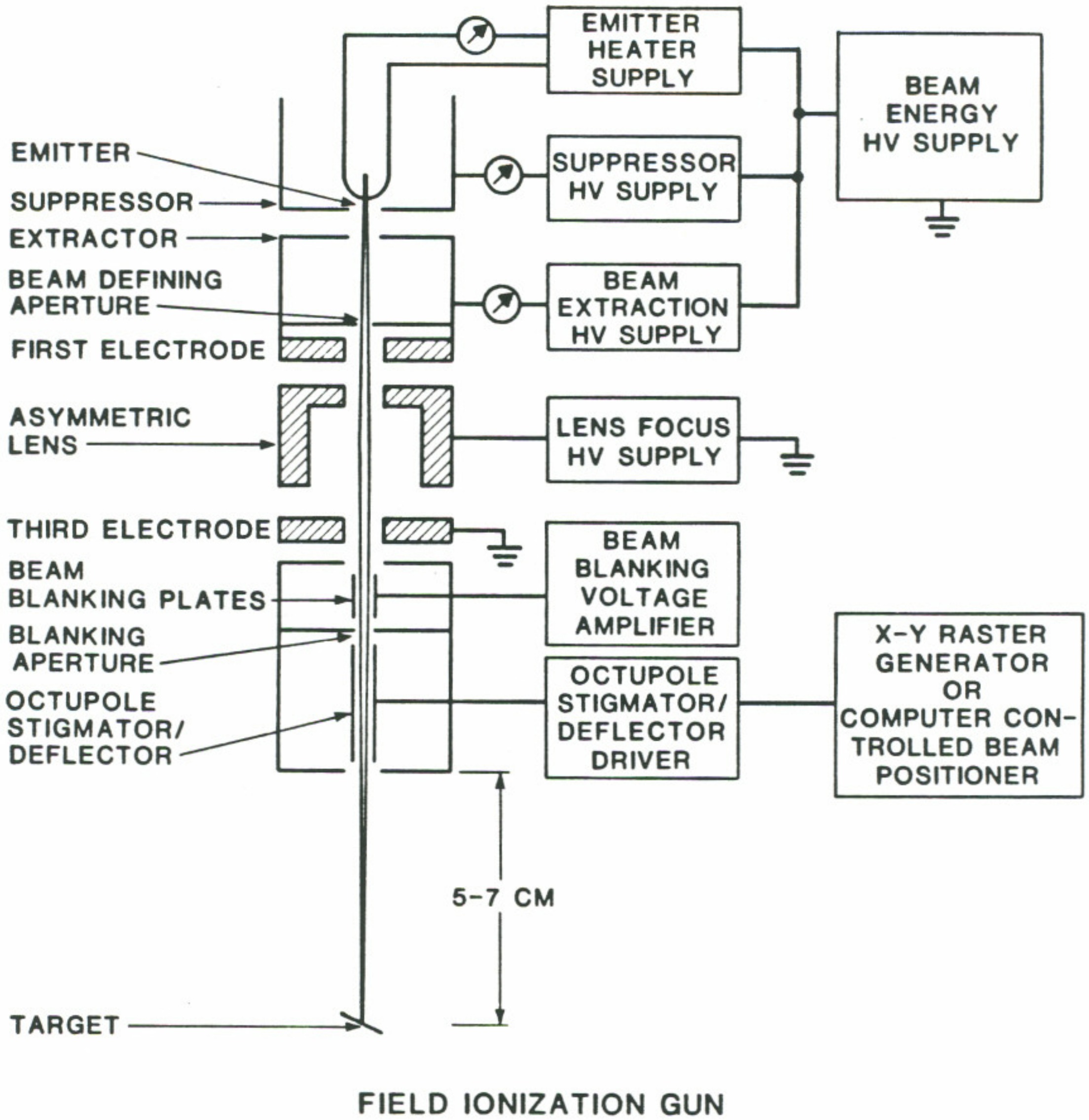

Figure 1.1 Schematic diagram of an FIBM workstation consisting of a liquid metal ion source, a three-element asymmetric einzel lens, and an octopole stigmator/defector, for which an ion beam can be focused and deflected by computer controlled DAC's or raster generators.

emitted from a source in one plane onto another plane. In electron microscopes and electron beam (e-beam) lithography machines the magnetic lenses are usually used to bend the paths of electrons. For focused ion beam system, since the ions are more massive and travel more slowly. electrostatic lenses are commonly used, which consist of three (or more) very precisely machined cylindrically symmetric electrodes at different potentials. The beam passing through ion lenses is focused and and accelerated by the electric fields. Since electrostatic fields are cylindrically symmetric about the axis of the beam, and since the focusing of the beam by the electric field is proportional to the distance from the axis, a lens-like operation results.

Surface interactions initiated by high energy ions on materials will result in many effects in the original materials such as ion implantation and sputtering, as shown schematically in Fig. 1.2. The sputtering process has been a topic of interest for more than twenty years[13]. The mechanism of the sputtering process has been studied by many researchers both theoretically and experimentally[14-31]. Some Monte Carlo computer programs for simulating the sputtering process were developed, such as TRIM.SP[32,33] and Marlowe[34].

In the past several years OGI's surface physics group and optoelectronics group have pioneered in the development of new techniques utilizing micromachining with focused ion beams, where the sputtering process has been explored to be used explicitly in removing materials at submicron scale. For example, focused ion beam micromachining has been used for various purposes on semiconductor diode lasers[35], such as the fabrication of laser mir-

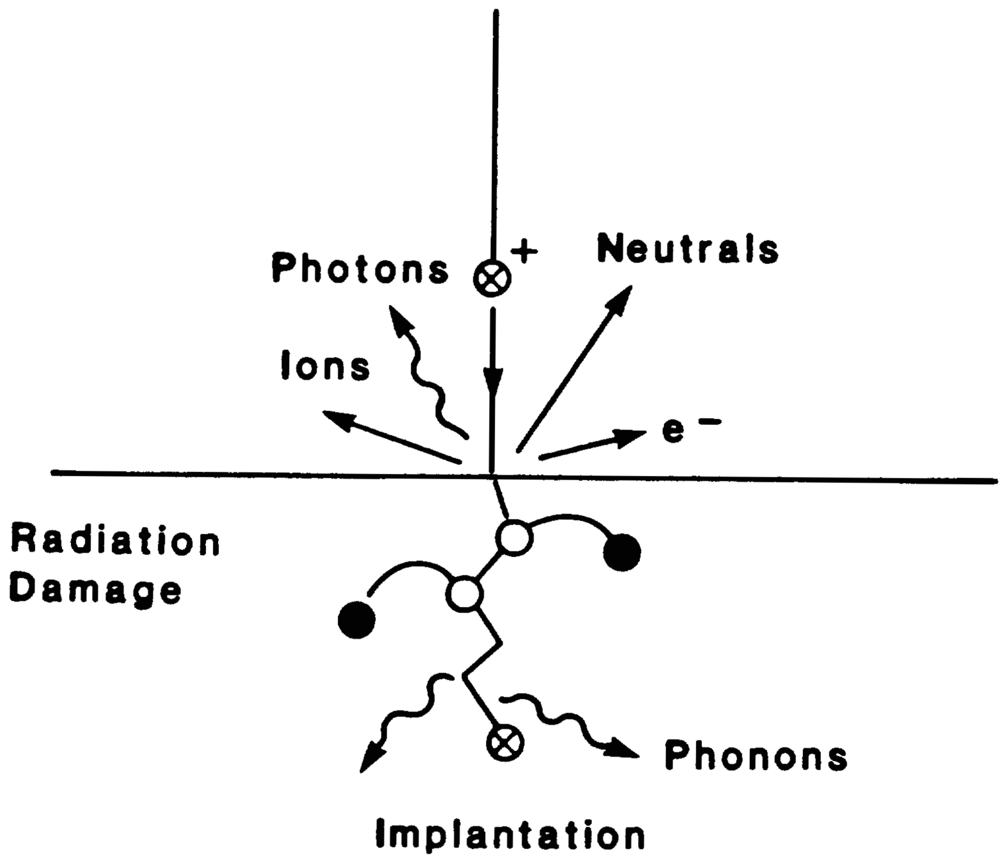

Figure 1.2 Schematic diagram of some ion/solid interactions initiated by a high energy ion such as implantation, sputtering, secondary electron/ion emission, and radiation damage.

ror facets[36], production of coupled-cavity lasers[37], fabrication of 45° deflecting mirrors for surface-emitting diode lasers[38] and formation of serpentine[39] and ring[40] distributed Bragg reflector (DBR) grating surface emitting (GSE) laser arrays.

In this dissertation, a simple computer simulation of FIBM in 3-D space, which is based upon an assumed Gaussian current distribution for the focused ion beam, has been developed (see chapter 2) in order to visualize FIB micromachined structures. The aim of the 3-D simulation is to provide software support for the computer controlled FIB micromachining of various structures on semiconductor diode laser devices.

In the process of fabricating the aforementioned structures by traditional FIBM, the ion beam was scanned along straight lines with constant scan speeds in two orthogonal (x and y) directions, and variable dwell time scan strategy was also reported[41]. However, for some applications the ion beam has to be scanned along a curved path in order to make 3-D non-linear features. Although, some attempts have been made at fabricating 3-D features using FIBM[41], applications of straight line scans are limited. A new, 3-D digital scan strategy developed to fabricate non-linear 3-D features by scanning the ion beam along a curved path has been studied in chapter 3. As a result of this strategy, several 3-D features have been micromachined, including "V" and micro-"V" mirrors designed to enhance coupling between adjacent laser stripes in semiconductor diode laser arrays and parabolic mirrors designed to produce unstable resonator ring lasers in diode laser arrays. Also the 3-D computer simulation could be used to investigate such complicated 3-D structures.

All experiments conducted in this dissertation research (see chapter 4) were accomplished at an FIBM workstation consisting of an AMRAY 1830 SEM, and an ion gun manufactured by FEI Co. with a 25 keV Ga^+ ion beam focused into a 500Å to 0.25μm diameter spot. The position of the ion beam has been controlled by an IBM-compatible computer though 12-bit DACs in such way that the ion beam is scanned according to certain scan strategies. Several special features have been FIB micromachined in order to verify the computer simulation. Some of them had been designed to improve the performance of diode laser devices, such as 45° turning mirrors used to form ring lasers, "V" and micro-"V"s mirrors designed to enhance coupling between laser stripes and parabolic turning mirrors designed to achieve unstable resonator ring lasers. However, only ring lasers, using 45° turning mirrors, have, to this point, demonstrated some improvements[39,40].

2. THREE-DIMENSIONAL MODEL OF COMPUTER SIMULATION FOR FIB MICROMACHINING

2.1 Introduction

The main objective of a computer simulation for FIB micromachining is to predict shapes of structures that need to be fabricated, before carrying on the actual micromachining, in order to prevent any mistakes in the machining process. The aim of this 3-D simulation is to provide software support for the computer controlled FIB micromachining of various 3-D structures on semiconductor diode laser devices.

A 2-D simulation method for FIBM[42], commercial software[43] and a 3-D simulation method for static and broad (usually 2mm in diameter) ion beam etching[44] have been developed by various workers. However, in literature, 3-D simulations for focused and scanned ion beam micromachining have not been reported yet. For that reason, an attempt to do at such a 3-D simulation for FIBM in cooperation with a 3-D digital scan strategy for the FIB system has been initiated in OGI. The 3-D simulation will be discussed in this chapter and the scan strategy in next chapter.

A computer simulation can also provide helpful information for one who performs FIB micromachining of a structure for the first time. One can simulate the FIB micromachining on a computer first, to estimate whether the structure is the one which he or she is expecting with 3-D display and then carry out the actual FIBM correspondingly. A computer simulation of FIBM based upon an assumed Gaussian current distribution will be discussed in section 2.3.3.

For a 3-D feature, one cannot inspect the actual machined structure from a cleaved cross-section because the cross-sections will be different as the cleaved facets are changed to different locations. Therefore, an effective way to investigate any FIB micromachined 3-D structure is extremely important for fully understanding the FIBM technique. One straightforward way is the computer simulation of FIBM in 3-D space, which would reflect the actual micromachined structure. An initial attempt to do such a 3-D simulation has been made based upon an assumed Gaussian current distribution of the ion beam.

2.2 Background

The essence of a computer simulation is to find a function, discrete or continuous, which represents a physical phenomenon of interest (under certain assumptions), based upon the nature of the physical phenomenon. In the case of ion beam sputter etching, it is to find functions which represent the surface of a wavefront (i.e. etching-front); then to plot the functions in a 2-D or 3-D display. Although the physical conditions are known for ion beam sputter etching, there are many uncertainties about how to approach the evolution of the surface under ion bombardment. There have been several approaches, including characteristic line analysis and string line segments algorithm.

2.2.1 Simulation using a characteristic line analysis

R. Smith *et al* have developed a fairly complete computer simulation theory[44-46] taking into account some secondary effects[47-50], such as the sputtering yield angular dependency, ion beam reflection, and redeposition, based upon characteristic line analysis for homogeneous etching using a static and broad ion beam (usually 2 millimeters in diameter). To determine the direction of propagation surface contours, at first they solve the differential equation describing erosion in the surface normal direction,

$$\frac{\partial r_n}{\partial t} = -\frac{\phi}{N} S(\theta)\cos\theta,$$

where S is the sputtering yield, ϕ is the incident ion flux (ions cm$^{-2}s^{-1}$), θ is incident angle of the ion beam, and r_n is distance in the normal direction. This means the x and y etching components have been taken into account implying that homogeneous etching has been simulated. Then equations which represent the propagation of the wavefront, can be obtained as follows,

$$x'_i = x_i - S'/S \cos^2\theta \frac{\sigma_x}{\sigma_z(\sigma_x{}^2+\sigma_y{}^2)^{1/2}} t_1,$$

$$y'_i = y_i - S'/S \cos^2\theta \frac{\sigma_y}{\sigma_z(\sigma_x{}^2+\sigma_y{}^2)^{1/2}} t_1,$$

$$z'_i = z_i + \left\{ \frac{1}{\sigma_z} + S'/S \, \frac{(\sigma_x{}^2+\sigma_y{}^2)^{1/2}}{\sigma_x{}^2+\sigma_y{}^2+\sigma_z{}^2} \right\} t_1,$$

where S' is the first derivative of S with respect to θ, t_1 is the total propagation time, and the $(\sigma_x,\sigma_y,\sigma_z)$ is a constant spatial vector along the characteristic lines determined by the ion flux ϕ and the sputtering yield S. A new wavefront (x'_i,y'_i,z'_i) thus solved propagates along the characteristic lines at a certain angle with respect to the existing wavefront (x_i,y_i,z_i), i.e. by solving the differential equation, a set of spatial functions of time has been obtained to describe the advance of the wavefront. Furthermore, with a beam several millimeters in diameter, broad ion beam etching has often been described in terms of the surface evolution of an initial surface contour, but the conventional FIBM is used to create larger-size structures than the ion beam spot itself, by scanning the focused ion beam.

Comparing with other simulations, the characteristic line analysis has its own problems with respect to the mathematical approaches to describe corners and edges. Especially, if the initial contour is a smooth curve, then surface gradient discontinuities can arise when characteristics intersect, so that care has to be taken when computing an eroded surface to remove points which occur after characteristic intersections.

2.2.2 String line segments algorithm

Meanwhile, attempts to simulate the sputter etching process have been carried out[51-54], and some groups have taken into account secondary effects[55-59]. Among them, a commercial program (SAMPLE) using a "string line segments algorithm" by Neureuther *et al*[43,60], has been developed. This algorithm treats the cross-section of an etched depth profile as a string of line segments in two dimensional space. Evidently, a new etching position of a point is calculated by assuming the adjacent line segments advance as planar fronts to form a new intersection, rather than advancing in the direction of the perpendicular bisector of the adjacent segments at the rate for that direction. However, this simulation is for homogeneous etching processes. Rangelow *et al*[61] have gone a step further, exploring the potential of the "string line segments algorithm" to develop a computer simulation including secondary effects.

Another 2-D simulation program named COMPOSITE[62], which allows the simulation of all important processing steps occurring in typical sequences involved in the fabrication of integrated circuits such as doping, oxidation, lithography, etching and layer deposition, has been developed extensively based upon the SAMPLE. Using the COMPOSITE program, Mueller *et al* have developed a fairly accurate two-dimensional computer simulation to describe the repair of X-ray mask structures with focused ion beams ($0.1 - 0.3\ \mu m$ in diameter), by using a semi-empirical approach to the redeposition effect[42,63]. As a different approach to advance the etching wavefront, they note that "The ion beam, which is assumed to be homogeneous in usual ion milling, was confined in one direction (x-direction)". Moreover they indeed mentioned that the theory could apply for three-dimensional cases. However, "because the numerical effort for calculating three-dimensional effects is extremely high, a simple analytical model has been developed, which reduces the problem to a two-dimensional one". Therefore, this 2-D computer simulation has been one of the most promising approaches in the 2-D simulation of FIB techniques.

In the late '80s, both Smith and Mueller *et al* had stopped their theoretical research on computer simulations of FIB techniques, while the reactive gas assist focused ion beam etching (RGAFIBE) technique has grown rapidly. More and more, people have intended to overcome the secondary effects experimentally, rather than theoretically. It seems that the theoreticians have not kept on developing of RGAFIBE technology, although modern computer power has already provided the complete possibility.

2.3 Three-dimensional computer simulation

2.3.1 Assumptions

We will put forward three basic assumptions to describe the sputtering process in conjunction with a variable-scan-speed ion beam scan strategy throughout chapter 2 and 3. The first assumption is that the ion beam at the target is of a Gaussian current distribution[64], although actually the ion beam current distribution is a quasi-Gaussian one with a long non-Gaussian tail[65-69]. The second one is that, for each incident ion there will be a fixed amount of atoms sputtered off the substrate, and the recession of the surface is along the incident beam direction[42,63], because FIB micromachining is a sputtering process where sputtering occurs mainly along the incident beam direction. The third one is that, if the ion beam current and spot size are kept constant in an experiment, the volume of removed material is linearly proportional to the ion beam dwell time.

Based upon the above assumptions, a Gaussian shaped crater will be machined by the Gaussian beam itself. Experimental evidence of such Gaussian shaped craters[68] has been observed (see section 4.2.1 for details). It could be deduced that a Gaussian depth profile in 3-D space should be a good approximation[70,71] of the etching surface in the first order simulation of FIB micromachining. We can then derive the smallest volume element dv removed by this Gaussian beam as follows,

$$dv = \int_{-\infty}^{+\infty} \int_{-\infty}^{+\infty} \frac{K}{2\pi} \exp\left(-\frac{x^2+y^2}{2\sigma^2}\right) dx\ dy\ dt = K\ \sigma^2\ dt, \tag{2.1}$$

where 2σ is the Gaussian beam diameter, dt is the minimum achievable dwell time and K is the etch rate. K can be experimentally determined by carefully machining a series of simple patterns, (for example, rectangles or straight lines), on a given material with different ion doses. The depth of cross-section divided by the dwell time dt times the number of scans is the etch rate K in μm per second per scan. A pre-determined etch rate K can then be used in the simulation program. With our present FIB workstation, when the ion beam is focused to $0.25\mu m$ in diameter and with a total beam current of about 290pA, the term $K \bullet dt$ is approximatively $0.001\mu m$ for GaAs materials. Typically, the dwell time dt ranged from several μs to several ms for standard 12-bits DAC's. Therefore, in real FIB micromachining experiments the ion beam will have to be scanned thousands of times in order to machine a crater with a depth of several micrometers.

A focused Ga^+ ion beam will mostly sputter materials inside a region of the Gaussian distribution with a radius of three or four beam radii. However, we can extend the above Gaussian integration to ($-\infty$ to $+\infty$), because the integral of a Gaussian or an error function is dominated in the region, where x or y range $(-4\sigma, +4\sigma)$. due to the nature of a Gaussian or an error function. For the sake of mathematical simplicity, we will keep using Gaussians (i.e. error functions), rather than truncated Gaussians. It is evident that the crater depth will not practically be affected by part of the Gaussian function outside the $(-4\sigma, +4\sigma)$ region.

2.3.2 Limitations

What is the limitation of this simulation? All the secondary effects, namely sputtering yield angular dependency, ion beam reflection, and redeposition, have not been taken into account! Therefore the present simulation will apply to cases for which the depth aspect ratio is small, while the non-Gaussian tail effect and secondary effects are not very pronounced.

These secondary effects have bothered everyone in the FIB field, since the invention of FIB system. Much effort has been made for understanding or solving both theoretically and experimentally these secondary effects. However, in about the last decade a most promising new technique in FIB has been developed by various groups[72-78], which is the reactive gas (Cl_2) assisted FIB. Evidence of high sputtering yield and negligible influence of secondary effects have been observed[79]. U-shaped grooves with nearly vertical side walls are formed by reactive gas assisted FIB, rather than the V-shaped grooves with slanted side walls of several degrees, which are believed due to the redeposition and/or self-focusing (ion reflection) effects.

As far as we know, up to date, the simulation of the effects of reactive gas assisted ion beam etching in three-dimensional space has not been reported in literature. However, due to the above-mentioned efficient technique, the simulation should be easy to do, because all secondary effects have effectively disappeared. Therefore, the present simulation using Gaussian depth profile, could be accurate enough for the simulation of reactive gas assisted ion beam etching because the secondary effects, such as redeposition and/or ion reflection, are unremarkable. For this simple Gaussian beam approach, we will apply our simulation not only to the depth profile, but also to introduce the concept of roughness of a FIB micromachined crater, in order to explain the mechanism of FIB micromachining from an experimental point of view.

This simulation does have one interesting feature, i.e. the etch rate K can be a function of x,y,z. This is very useful for the simulation of fabrication of various diode laser devices, or for performing failure analysis on IC devices, which often have different materials in different layers in a sandwich structure.

2.3.3 Gaussian depth profile

By analogy with digging a trench shovel by shovel, the FIB micromachining process can be simulated by sputtering (digging) material from a semiconductor diode laser or IC device (the ground) with an ion beam (the shovel) to machine a structure (the trench). The total structure is constituted by many small Gaussians (shovels) gradually. Therefore, the surface of this structure is not mathematically smooth, and has a certain roughness, discussed in section 2.3.6. Based upon the above-mentioned two assumptions, for a first order simulation of FIBM, a Gaussian depth profile in 3-D space is appropriate. Therefore, the following simulation will be exactly accurate only for very shallow craters where these secondary effects can be ignored, or for reactive gas (Cl_2) assisted FIB etching technique.

From Eqn. (2.1), the depth of a crater, machined by a Gaussian beam with minimal dwell time dt, is $\frac{K}{2\pi}\exp(-\frac{x^2+y^2}{2\sigma^2})\ dt$. Experimentally, to create a structure, this small Gaussian beam has to be placed (scanned) in an area many many times, according to a certain beam scan strategy. Therefore, the simulated FIBM etching depth $Z(x,y)$ of a crater is represented by the following equation,

$$Z(x,y) = N \sum_{x_p, y_p} \frac{K}{2\pi} \exp\left(-\frac{(x-x_p)^2+(y-y_p)^2}{2\sigma^2}\right) \omega(x_p,y_p)\ dt, \qquad (2.2)$$

where $Z(x,y)$ is the crater depth at point (x,y), and N is the total number of beam scans. $\omega(x_p,y_p)$ is a weighting factor in multiples of the minimum achievable dwell time dt at each scan point (x_p,y_p), which could be used to simulate scan strategies with variable dwell time. $Z(x,y)$ is summed over a set of discrete points (x_p,y_p) as a sub-set of a 4096×4096 pixel space (because we are using 12-bit DAC's), determined by a beam scan strategy as described in the next chapter.

In a real FIB micromachining experiment, to machine a crater the material will be gradually removed one small volume element at a time. The temporal location (x_p,y_p) of the ion beam can be varied for different applications based upon a beam scan strategy with constant dwell time dt[80]. Also for a given scan strategy, i.e. a fixed set of (x_p,y_p), one can vary the dwell time function $\omega(x_p,y_p)$, to gain more freedom in control of depth profiles[41,81].

Normally only a top view of any FIBM structure will be seen under SEM examination, and depth profiles of these structures cannot be obtained directly by SEM observation. Therefore, one would usually cleave a sample and then inspect a cross-section of the structure with a SEM in order to obtain the depth profile. But this is possible only if the structure has been machined by straight line scans and the cleaved line is perpendicular to the scan direction. In cases of more complicated 3-D structures in which the ion beam is scanned along curved paths, there are no directions along which one can cleave the sample to obtain a general cross-section of the depth profiles. Therefore a 3-D simulation of the FIBM is useful for "viewing" the depth profiles of such 3-D features, by inverting the z axis.

3-D normal and inverted views of a simulated FIB micromachined circular crater are shown in Fig. 2.1, where a non-uniform depth profile has been produced by scanning a simulated ion beam at a constant x scan speed, but a variable y scan speed according to an equation of a circle. Obviously, a more sophisticated beam scan strategy is needed to fabricate a 3-D structure with a uniform depth profile, which is desired for certain applications.

2.3.4 Single scan approach

According to Eqn. (2.2), materials are always removed in the same fashion with a fixed scan strategy and dwell time function. In other words, the Gaussian beam is scanned by a fixed set of (x_p, y_p) and a fixed function $\omega(x_p, y_p)$ of dwell time dt for N times. On the other hand, for certain applications of interest the ion beam has to be scanned differently for each pass of the ion beam; thus a simple multiplication by N cannot handle these special cases[41,80]. Therefore a single scan approach were developed.

As we know, the removal rate per scan is about a few nanometers in the z direction using a 0.3nA, 25 keV Ga^+ ion beam with a 0.25μm spot size. Thus, to fabricate a 3-D structure with several micrometers depth, the ion beam will need to be scanned many times in order to achieve a desired depth profile. At the $n+1^{th}$ scan, the etching depth $Z_{n+1}(x,y)$ is represented by the

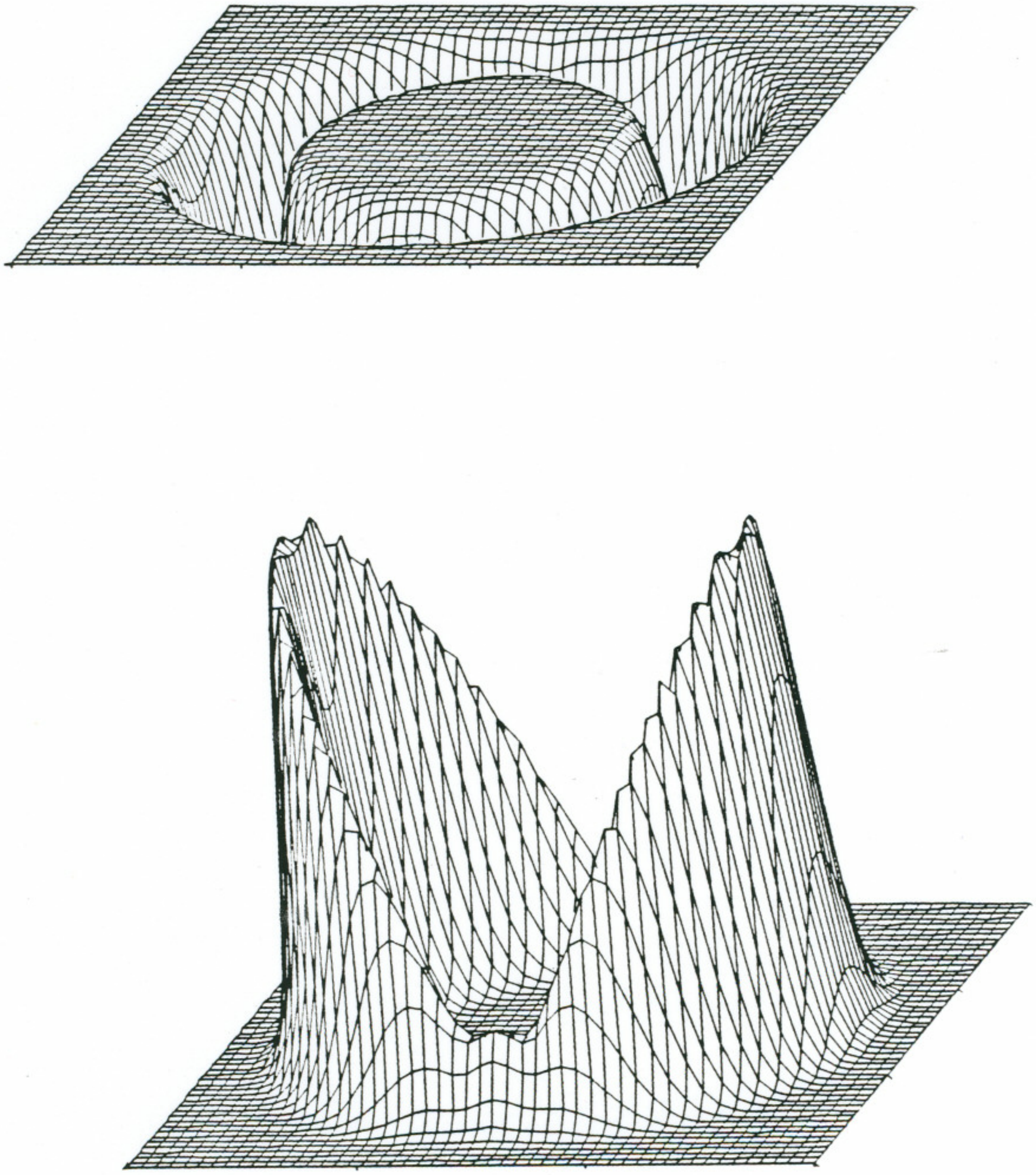

Figure 2.1 3-D normal and inverted views of a simulated circular crater. A non-uniform depth profile, as shown in the inverted view, has been produced by scanning a simulated ion beam at a constant y scan speed.

following equation,

$$Z_{n+1}(x,y) = Z_n(x,y) + \sum_{x_p,y_p} \frac{K}{2\pi} \exp\left(-\frac{(x-x_p)^2+(y-y_p)^2}{2\sigma^2}\right) \omega(x_p,y_p)\, dt, \quad (2.3)$$

where $Z_n(x,y)$ is the depth profile of the previously micromachined structure, so-called a single scan approach. Evidently, (x_p,y_p) and $\omega(x_p,y_p)$ do not have to be the same at each sweep of the Gaussian beam. Some applications of this single scan approach have been used to fabricate a 45° or a parabolic deflecting mirror[35,38], machining them into diode laser waveguides to make surface emitting laser devices. This was done by shrinking the rectangular scan area with each pass of the beam. Also the dwell time function $\omega(x_p,y_p)$ could be varied as well[41]. In section 2.3.5, we will discuss the simulation of etch rate K as a function of z, which is made possible by this single scan approach. The computer implementation and source code will be described in detail in Appendix B.

2.3.5 Etch rate as a function of depth (z)

For many applications of focused ion beam techniques, such as the fabrication of various semiconductor diode laser devices, repair of X-ray masks, and failure analysis on integrated circuits, the substrate which needs to be micromachined usually has different kinds of materials in different layers. Therefore the etch rate K has to recognize such differences. Because Eqn.

(2.2) determines the depth profile of FIB micromachined structure for a single component substrate, Eqn. (2.2) cannot treat the cases for which the substrate has more than one component. However, if we use the single scan approach, then the etch rate K can be made a function of depth z. Eqn. (2.3) is rewritten in the following way,

$$Z_{n+1}(x,y) = Z_n(x,y) + \sum_{x_p,y_p} \frac{K(Z_n(x,y))}{2\pi} \exp\left(-\frac{(x-x_p)^2+(y-y_p)^2}{2\sigma^2}\right) \omega(x_p,y_p)\, dt, \tag{2.4}$$

where K is now a function of $Z_n(x,y)$.

Because the etching-front $Z_n(x,y)$ will advance a few nanometers per scan, along the incident ion beam direction, i.e. z direction, the error of the different etch rate K, introduced by this single scan approach, will be about a few nanometers in the calculation of depth profiles at the interfacial plane of two different material layers. For example, when the smallest Gaussian is sputtering away one half volume of materials from the present layer and the other half volume of materials from next layer during one sweep of the beam, in the interfacial plane, the error of the different etch rate K will be magnified by the factor of $\frac{K_2}{K_1}$, where K_1 is the etch rate of the present layer, and K_2 is the next layer. But the etching-front $Z_{n+1}(x,y)$ has no knowledge about which actual etching-front was already in the next layer with a different etch rate K_2.

To eliminate this type of error, a split scan approach has been introduced exclusively for the sandwich structures, i.e. where the etch rate K as a function of $Z_n(x,y)$. Of course, if one is not concerned about the errors, one does not have to spend extra computing time to gain a small improvement in accuracy. However, to complete the simulation of the etch rate K as a function of $z(x,y)$, we introduce such a split scan approach as the following.

Defining $A_l(x,y) = \sum_{x_p,y_p} \frac{1}{2\pi} \exp\left(-\frac{(x-x_p)^2+(y-y_p)^2}{2\sigma^2}\right)\omega(x_p,y_p)\,dt,$

and $Z_{poss}(x,y) = Z_n(x,y) + K_1 A_l(x,y),$

where $Z_{poss}(x,y)$ represents possible new etching-front. If $Z_{poss}(x,y) \le H_K$, where H_K is the depth of the interfacial plane, then Eqn. (2.4) is used. Otherwise,

$$\begin{aligned} Z_{n+1}(x,y) &= Z_n(x,y) + K_1 A_l(x,y) \\ &\quad - (Z_n(x,y) + K_1 A_l(x,y) - H_K) \\ &\quad + \frac{K_2}{K_1}(Z_n(x,y) + K_1 A_l(x,y) - H_K) \\ &= Z_{poss}(x,y) + \frac{(K_2 - K_1)}{K_1}(Z_{poss}(x,y) - H_K). \end{aligned} \tag{2.5}$$

Therefore, during each pass of the Gaussian beam, the simulation program will check the possible new etching-front $Z_{poss}(x,y)$ whether it exceeds H_K or not. The following algorithm is implemented into the computer simulation program,

if ($Z_{poss}(x,y)$ .le. H_K) then

$$Z_{n+1}(x,y) = Z_{poss}(x,y)$$

else

$$Z_{n+1}(x,y) = Z_{poss}(x,y) + \frac{(K_2 - K_1)}{K_1}(Z_{poss}(x,y) - H_K).$$

To illustrate this split scan strategy, assuming the depth H_K of the interfacial plane for a two-layer wafer is equal to $0.5\mu m$, and $K_1 = 1.0$, $K_2 = 2.0$ in Fig. 2.2(a), $K_2 = 0.5$ in Fig. 2.2(b), the first curve, in both figures, represents an existing crater machined into first layer of the wafer. In Fig. 2.2(a), if K_1 is still used as the etch rate, then the second curve will be the new etching-front, which is shallower than the real one, because $K_1 < K_2$. On the other hand, if K_2 is chosen, then the deepest (fourth) curve will be the new etching-front; it is deeper and wider than the real one because part of the crater should be in the first layer. However, by introducing the split scan strategy, the third curve is obtained, for which part of the crater below the first layer belongs to second curve, and the other part beyond the first layer is magnified by $\frac{K_2}{K_1}$. By contrast, in Fig. 2.2(b) the second curve with K_2 is too

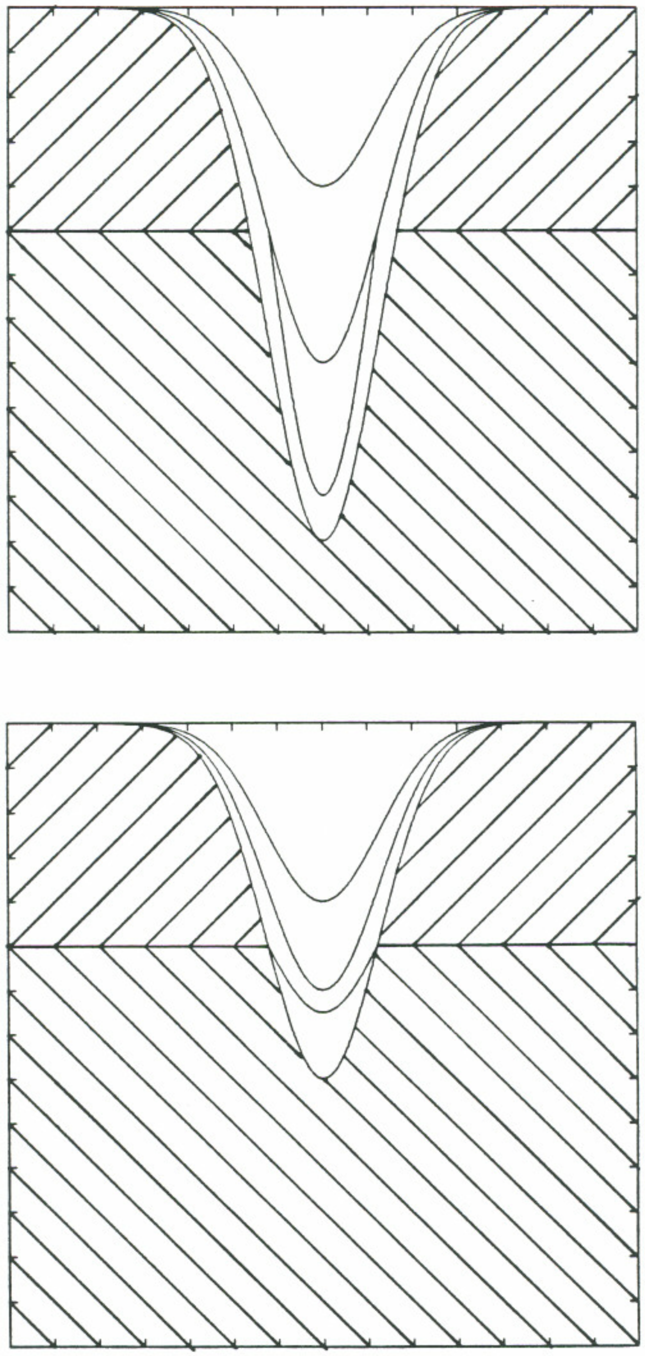

Figure 2.2 Cross-sections of simulated grooves using the split scan strategy. (a) Upper: sputtering yield of the FIRST layer material is equal to one half of the yield of the SECOND layer. (b) Lower: sputtering yield of the SECOND layer material is equal to one half of the yield of the FIRST layer.

shallow, and the fourth one with K_1 is too deep, while using the split scan strategy the third curve is laid between the second and fourth, reflecting the fact that $K_1 > K_2$.

Obviously, this scan approach can only be used when the etch rate K is a step function of $z(x,y)$. Furthermore, we only check $Z_{poss}(x,y)$ against H_K, but not each basic small Gaussian element, that implies we only consider an average effect over one full sweep of the Gaussian beam. On the other hand, the split scan approach reflects the real micromachining more closely than the single scan approach when the substrate has a sandwich structure (see section 4.3.1 for details). In case of K as continuous functions of $z(x,y)$, Eqn. (2.4) is used.

2.3.6 Roughness of a micromachined surface (RN)

Since an ion beam is scanned in a discrete manner, i.e. a digital scan, the roughness has to be investigated in order to choose an adequate scan strategy to FIB micromachine a 3-D structure with optical quality surfaces. If the ion beam is scanned in such fashion that two adjacent scan points are more than one beam diameter apart, then a non-uniform depth profile and crater wall would be produced. On the other hand, if one wants to make optical diffraction gratings or quasi-sinusoidal surface contours, the separation of two adjacent scan points has to be greater than one beam spot size. By introducing the concept of "roughness of a micromachined surface", one can get a clear picture of this discrete digital scan, while an optically smooth micromachined surface can be obtained by choosing the adjacent scan points less than one beam radius. However, for an ion beam with uniform current distribution, one can obtain a uniform micromachined surface if the ion beam is scanned such that the separation of two adjacent scan points is less than one beam diameter.

If we assume that the Gaussian beam is scanned along the x axis, where $y_p = 0$, in such way that the separation of two adjacent scan points will be $\frac{2\sigma}{d}$, where d is a positive number and greater than unity, and that the etch rate K is constant, then after N scans, the depth profile of this simulated groove can be derived from Eqn. (2.2), when $\omega(x_p, y_p) = 1$,

$$Z(x,y) = \frac{NK}{2\pi}\sum_{i}^{I}\exp\left(-\frac{(x-2i\sigma/d)^2+y^2}{2\sigma^2}\right) dt, \tag{2.6}$$

where I is the number of total scan points in the straight line. A simulated groove, with $I = 11$ and separation equal to σ, is shown in Fig. 2.3 for 3-D normal and inverted views. Note that the side wall is smooth and the depth is uniform.

In fact, according to Eqn. (2.6), we just simply sum over all the small Gaussians at scan points (x_p, y_p), then multiply the sum by N and finally obtain a micromachined crater. In mathematics, we can also leave the Gaussian beam at one point (x_p, y_p) for the dwell time Ndt, then move it on to next point, which will give a same final structure as the previous machining method. However, in experiment, we want to scan the ion beam as fast as we

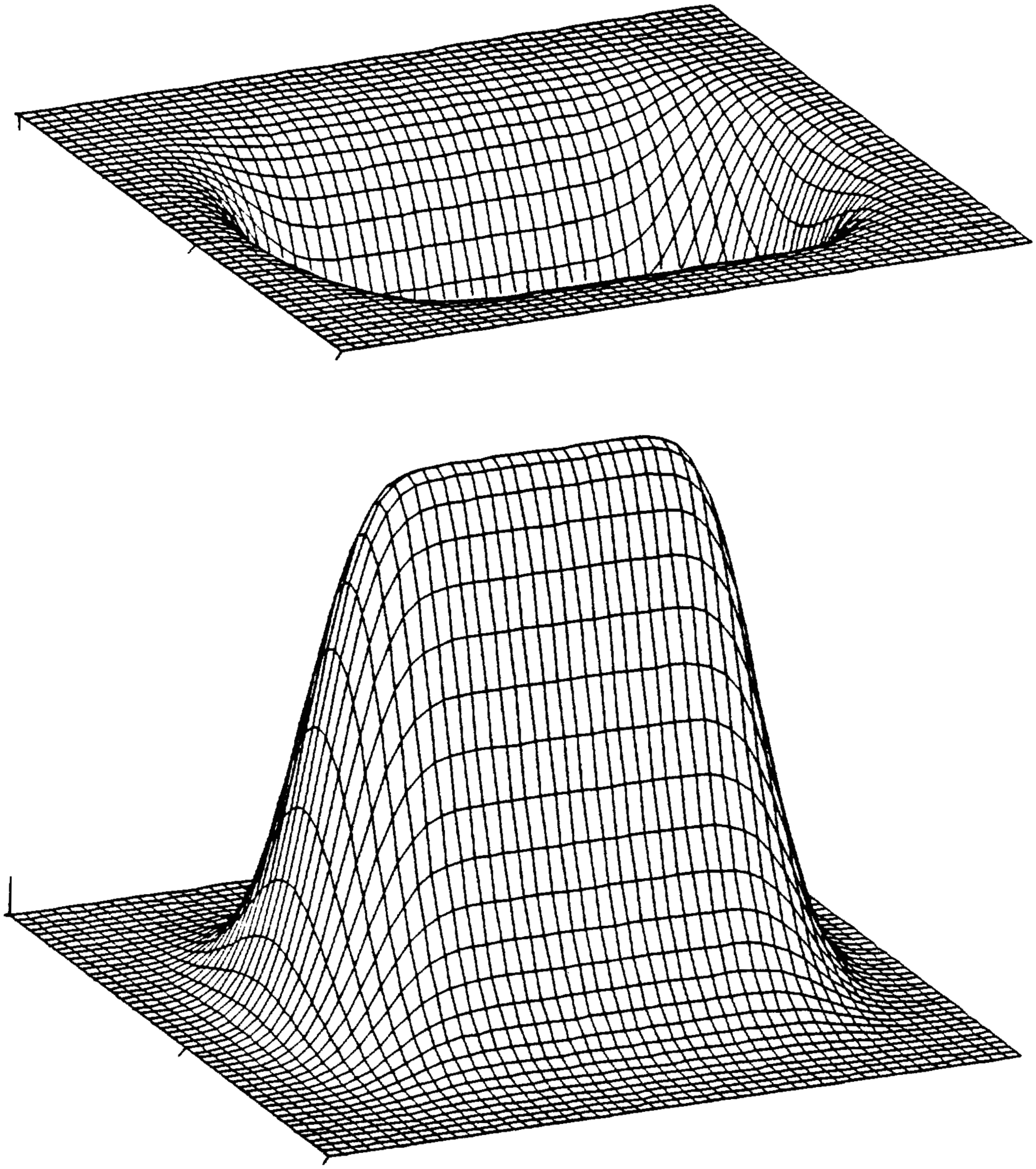

Figure 2.3 3-D normal and inverted views of a simulated groove. The groove with a uniform depth profile and smooth walls has been produced by digitally scanning a simulated ion beam along a straight line, where the separation of two adjacent scan points is σ (one half of spot size).

can, i.e. remove as little material as possible per scan, in order to eliminate all the secondary effects, mainly including sputtering yield angular dependency, ion beam reflection, and redeposition.

Therefore, to estimate the roughness of a micromachined crater using a Gaussian beam in a special case, we will machine a large Gaussian crater Ndv first, then machine another one at a scan point $\frac{2\sigma}{d}$ away from the previous scan point. In mathematics, this will give the same final crater as if the Gaussian beam is scanned back and forth between these two scan points separated by $\frac{2\sigma}{d}$. A dramatic crater machined by two large Gaussians, with a large separation 3σ, has been used for illustrating non-uniformity effects, as shown in Fig. 2.4 for 3-D normal and inverted views. Note that a non-uniform side wall and depth profile have been created. The equation of the large Gaussian crater is given as follows:

$$Z(x,y) = \frac{N\ K\ dt}{2\pi}\exp\left(-\frac{x^2+y^2}{2\sigma^2}\right), \tag{2.7}$$

where the height of the Gaussian is $\frac{N\ K\ dt}{2\pi}$. At a plane $z=C$, the cross-section of one large Gaussian crater is a circle, which is defined as,

$$x^2 + y^2 = 2\sigma^2 \ln\left(\frac{NKdt}{2\pi C}\right). \tag{2.8}$$

We define the roughness of the micromachined wall as $RN = R - H$, where

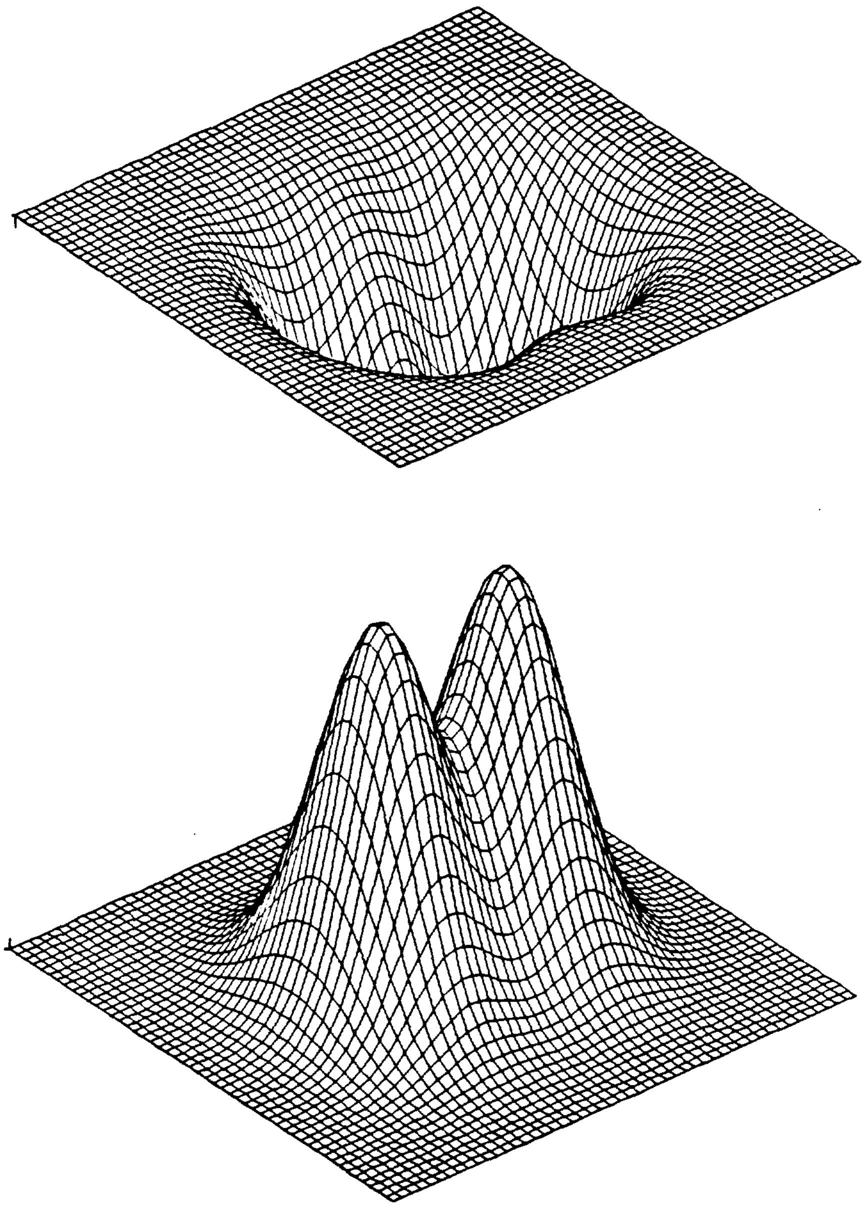

Figure 2.4 3-D normal and inverted views of a simulated structure. The structure with a non-uniform depth profile and rough walls has been produced by digitally scanning a simulated ion beam between two scan points with a separation of 3σ.

R is the radius of the circle and H is the distance from the intersection point of two circles to the axis of the simulated groove shown in Fig. 2.5. Therefore, we obtain

$$R^2 = 2\sigma^2 \ln\left(\frac{NKdt}{2\pi C}\right), \tag{2.9}$$

and

$$H^2 = R^2 - \left(\frac{\sigma}{d}\right)^2, \tag{2.10}$$

where $\frac{\sigma}{d}$ is one half of the separation of two adjacent scan points. Finally, from Eqns. (2.9) and (2.10) we can obtain the roughness of the side walls of this straight line groove, $RN = R - H$.

To evaluate the roughness RN as a function of the beam separation $\frac{2\sigma}{d}$, we recall that the definition of the etch rate K in μm per second per scan, which is the depth of cross-section divided by the product of the dwell time dt and the number of scans N. In other words, the final depth Z, i.e. the depth of cross-section of the crater, is equal to $\frac{N\ K\ dt}{2\pi}$. Therefore we can study RN as a function of the separation $\frac{2\sigma}{d}$, as well as the depth of the crater, $z = C = h\ Z$, where $0 \leq h \leq 1$. Then Eqn. (2.9) becomes,

$$R^2 = 2\sigma^2 \ln\left(\frac{1}{h}\right). \tag{2.11}$$

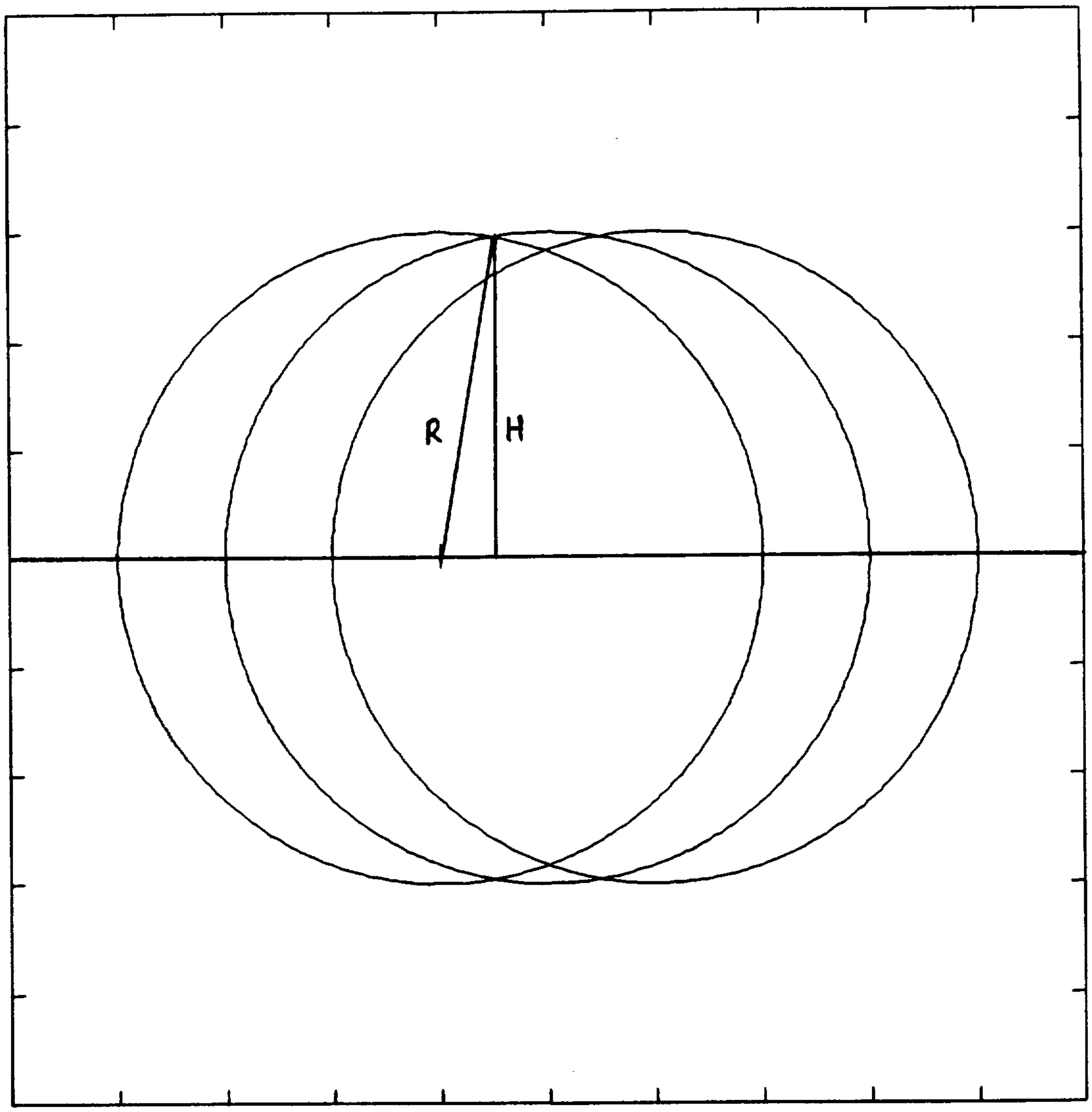

Figure 2.5 The definition of the roughness $(R - H)$ of micromachined walls is illustrated, where three overlapped circles represent a Gaussian beam at three adjacent scan points for the same dwell time. R is the radius and H is the distance.

By means of Eqn. (2.10), the normalized roughness is given by,

$$\frac{RN}{\sigma} = \sqrt{2\ln(\frac{1}{h})} - \sqrt{2\ln(\frac{1}{h}) - \frac{1}{d^2}}. \tag{2.12}$$

We can thus plot the $\frac{RN}{\sigma}$ with respect to normalized separation $\frac{2}{d}$ at different normalized depths h, as shown in Fig. 2.6.

Therefore, for separation of $\frac{\sigma}{2}$, the roughness RN is equal to about 0.03 σ when the depth goes from 0.1 Z to 0.6 Z. As an extreme case with a separation of 2 σ, (d = 1), h has to be less than or equal to 0.6 in order to make Eqn. (2.12) valid. On the other hand, if the separation is equal to $\frac{\sigma}{2}$, then the roughness RN is equal to 0.074 σ at h = 0.9. In other words, if an ion beam is scanned in such a way that the separation of two adjacent scan points is one quarter of a beam diameter, then the roughness of a side wall of a micromachined structure is not greater than 3.7% of one beam diameter, when the depth goes to 90% of the crater's full height. For an ion beam with 0.25μm spot size, when the separation is 0.0625μm, the roughness RN = 92.5 Å at h = 0.9, and RN = 37.5 Å at h = 0.6, which is 0.47% of a typical wavelength of AlGaAs semiconductor diode lasers (about 8000 Å).

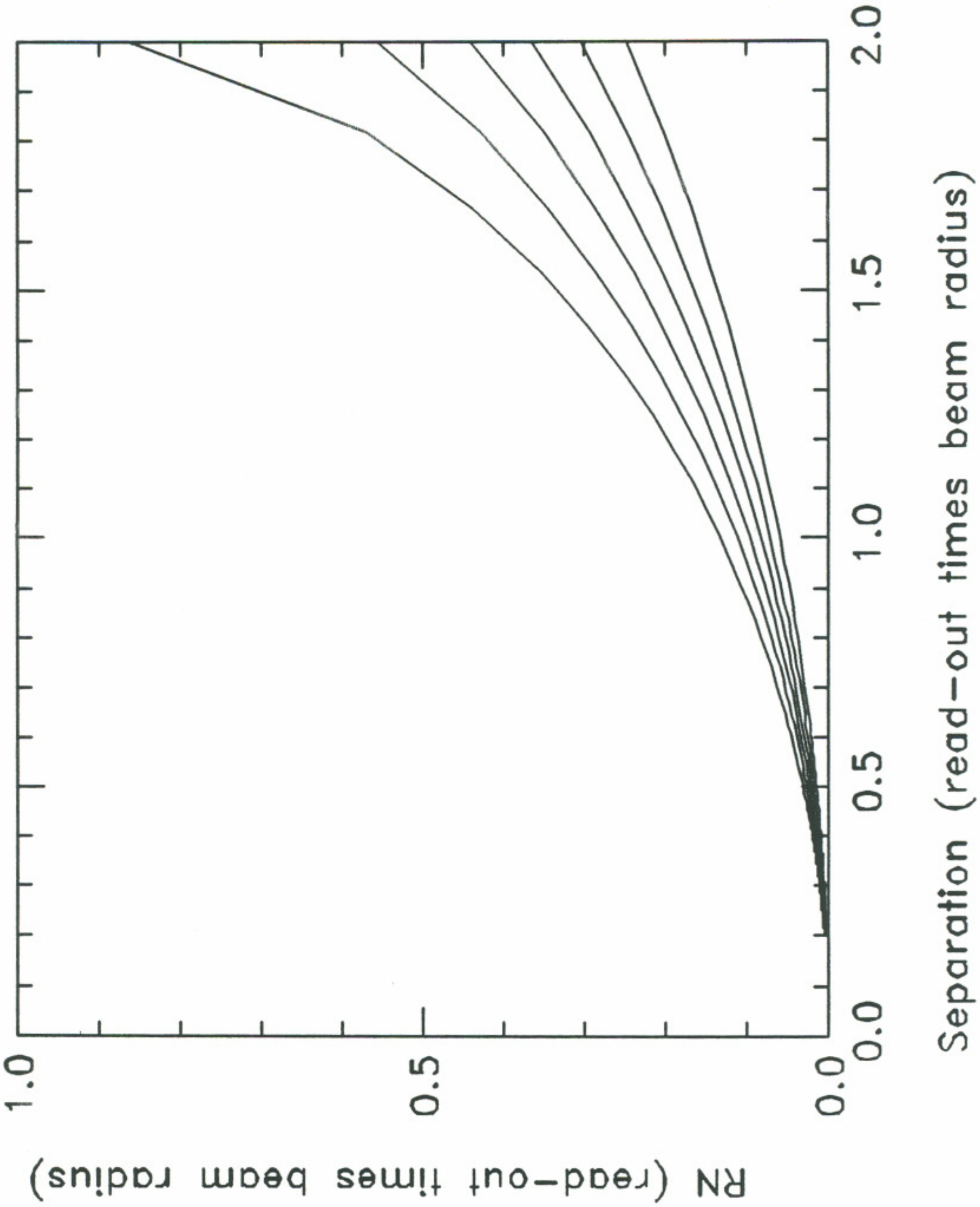

Figure 2.6 Roughness of micromachined walls vs. normalized separation of adjacent scan points is plotted at different normalized depth of micromachined structures. The normalized depth is varied from 0.1 to 0.6 in 0.1 intervals for the curves from the bottom to the top. The greater the depth toward the bottom of the structure, the higher the roughness of the side walls.

2.4 Conclusions

Under three basic assumptions, (1) the current distribution of an ion beam is Gaussian; (2) the sputtering occurs mainly along the incident beam direction; and (3) the volume of removed material is linearly proportional to the ion beam dwell time; the Gaussian depth profile micromachined by the simulated ion beam can thus be derived. With these assumptions, a fairly complete three-dimensional (3-D) computer simulation of focused ion beam micromachining has been developed. By this simulation several practical phenomena and some interesting problems have been investigated, which include the single scan approach for fabricating 45° or parabolic deflecting mirrors; the split scan approach for etch rate K as a function of depth z; and the introduction of roughness RN of a micromachined surface to provide a basic strategy of the ion beam digital scan.

Although this 3-D simulation did not take into account secondary effects, (i.e. sputtering yield angular dependency, ion beam reflection or self-focusing, and redeposition effects), this simulation will apply to cases where the depth aspect ratio is small, less than 2:1, or reactive gas (Cl_2) assisted focused ion beam etching is employed and the influence of all secondary effects is unremarkable. With all the above-mentioned features, this simulation computer program should be user-friendly, easy to use, and useful to an FIB operator who does not have to have extensive knowledge about FIB techniques. In other words, this 3-D simulation could provide a software support system built into any FIB micromachining system to give a visual 3-D picture of an expected 3-D structure rather quickly before the actual FIB machining.

A more accurate 3-D simulation taking into account all secondary effects such as redeposition, sputtering yield angular dependency and self-focusing, and providing more precise and efficient representations of a 3-D surface is extremely challenging. Unlike 2-D simulation such as string line segments algorithm[42, 43, 60, 63], the aforementioned 3-D simulation needs all information of surface locations including positions and orientations. For whatever approaches may be used, the final surface element must be less than one ion beam diameter, which will boost the requirement of a host computer. The key in this dissertation is to explain the concept of the 3-D simulation of FIBM by a simple model rather than complicated mathematical calculation.

3. ION BEAM SCAN STRATEGY FOR FABRICATING 3-D STRUCTURES

3.1 Introduction

In conventional FIB micromachining, a focused ion beam is always scanned along straight lines to machine narrow grooves or rectangular craters in order to fabricate submicron devices such as diode laser output mirrors and coupled cavity oscillator mirrors has been demonstrated[35,41,80,81]. However straight line scans cannot be satisfactorily used for some applications. Although the possibility of fabricating such 3-D structures has been briefly mentioned in the literature, no results have yet been reported. Moreover, the depth profiles of these above-mentioned 3-D structures can be non-linear, by altering dwell time or changing the width of rectangular scan regions, but boundaries or shapes of side walls are still straight lines.

However, curved or non-linear side walls are of particular interest for making unstable resonator lasers. A need for fabricating more sophisticated 3-D structures has arisen for certain applications. Therefore, a fully-digitized, non-linear, three-dimensional and variable-scan-speed scan strategy has to be developed in order to produce desired structures with arbitrarily curved paths in a plane and arbitrary depth profiles. This strategy has been implemented using a FIB system with an IBM-compatible computer to fabricate various kinds of 3-D structures. Due to certain specificities of the nature of FIB micromachining, where the x and y scan speeds determine depth profiles in the z direction, and the positions of the ion beam determine shapes of 3-D structures in the $x-y$ plane, the approach of this 3-D scan strategy will consist of two parts. One is to obtain the desired depth profile by scanning the ion beam along certain scan points (see section 3.3). The other is to achieve the desired depth profiles by selecting appropriate arc-scan-speeds (see section 3.4).

In general, there are two basic methods to scan an ion beam, one is continuous scan using analog signals from ramp signal generators, the other one is a discrete scan using discrete voltage signals from DAC's. The applications of continuous scan will be described extensively in section 3.2, and the variable-scan-speed strategy in both analog and discrete forms will be discussed in section 3.3 and 3.4.

3.2 Various structures machined by raster scans

Although various ion beam scan strategies has not been thoroughly discussed in literature, except variable dwell time strategy[41,81,82], there is indeed a need for a more sophisticated and more flexible scan strategy, especially for fabrication of semiconductor diode laser devices and for possible microsurgery on integrated circuits.

The position of an ion beam is usually controlled by a set of deflecting electrodes, in both x and y directions. Given definite values of deflection voltages, the ion beam will stay in a certain place, until a change of deflection voltages occurs. Therefore, different methods for changing deflecting voltages will result in different scan paths of the ion beam.

3.2.1 Non-linear path functions

In mathematics, a trajectory in the xy plane can be expressed by a set of x and y parametric functions of time t, $x = x(t)$ and $y = y(t)$. For example, a circle can be drawn by $x = a \cos(t)$ and $y = a \sin(t)$, where a is the radius of circle, and the center of circle is at origin. By analogy, a circular path function for the ion beam can be controlled by a set of deflection voltage functions of time t, i.e. ramp signals, $V_x = A \cos(t)$ and $V_y = A \sin(t)$, where V_x and V_y are the deflection voltages in the x and y channels, respectively, and A is the amplitude of the waveforms. By shrinking A after each complete revolution, a set concentric circles could be machined by the ion beam, which could be used as circular gratings in DBR-GSE diode lasers, or by applying different amplitude to the x and y channels, an ellipse could be produced. Also for mathematicians' fantasy, Lissajous path functions can be obtained by changing the frequencies of the ramp signals, i.e. $x = a \cos(mt)$ and $y = a \sin(nt)$, where m and n are integers. In Fig. 3.1, Lissajous path functions with various m and n have been shown, in principle, which could be machined by the ion beam, but are doubtfully of any practical value.

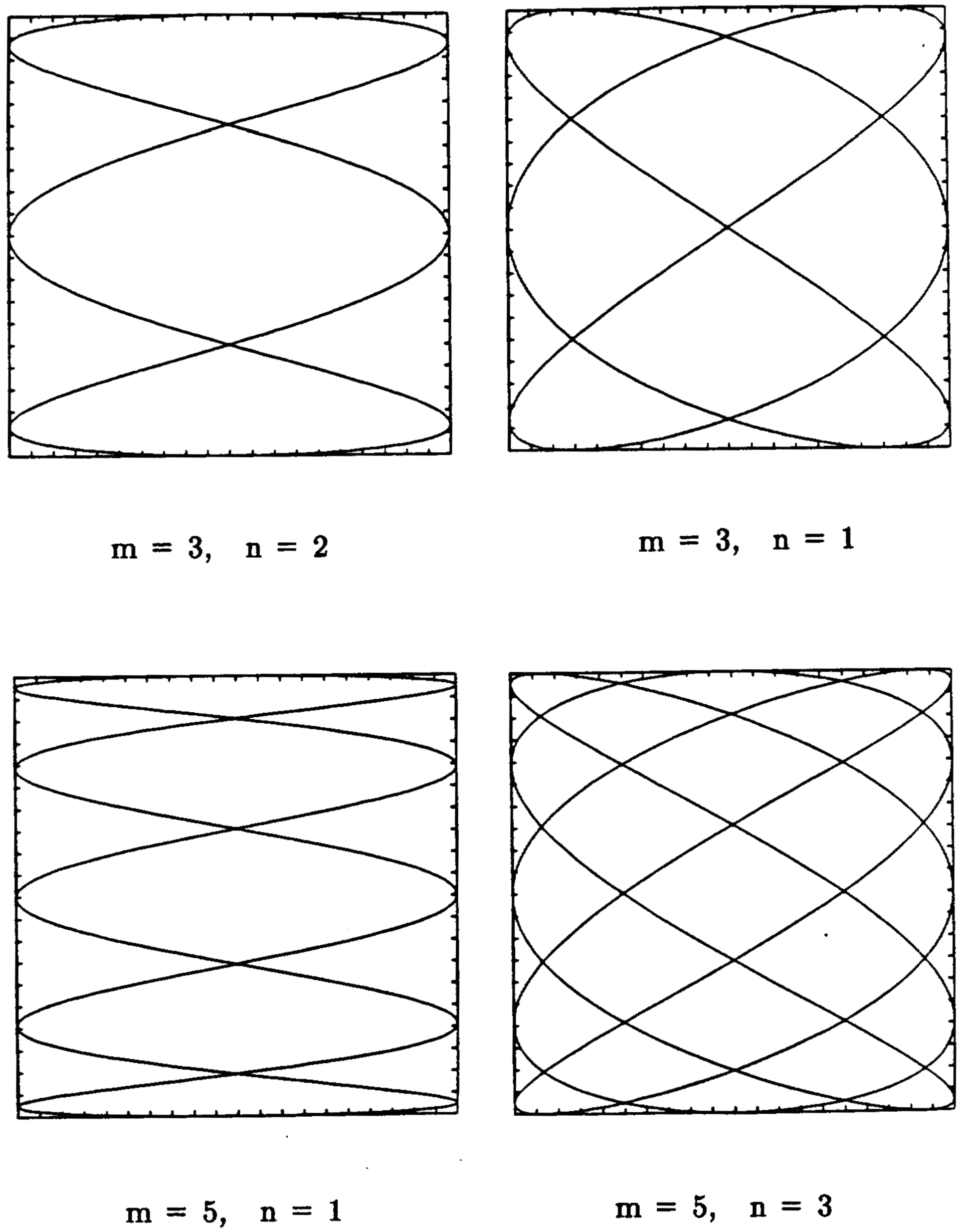

Figure 3.1 Possible trajectories of different path functions, in the xy plane, are generated using sinusoidal functions with different periods, $x = a \cos(mt)$ and $y = a \sin(nt)$.

3.2.2 Straight lines and rectangles

Saw-tooth and square waveforms are indeed valuable for fabricating diode laser devices and for analyzing failures of integrated circuits. Combinations of these two waveforms will provide a variety of straight line structures, including straight lines with or without slopes, rectangles, and squares. Based upon the nature of different ramp functions, we will break these features into two categories: one covers straight lines, the other rectangles and squares. With the same frequency in both x and y channels, a straight line function will be achieved, while with different frequencies, rectangles and squares can be made.

3.2.2.1 Straight lines

Within one period, waveforms can be written as $x = at$ and $y = bt$, where a and b are the slopes of the ramp. Therefore, the equation of this straight line in the xy plane is $y = \frac{b}{a}\, x$, i.e. a straight line with slope $\frac{b}{a}$. In other words, by varying the values of a and b, the ion beam can be scanned in a straight line with a variable slope $\frac{b}{a}$. For example, if $a = b$, a 45° line will be produced. If we want a straight line parallel to either axis, a square waveform can be simply applied to the other axis.

To select the starting and ending points of straight lines, certain off-set voltages are added to the ramp signal. Because an ion beam can be scanned practically by only a certain range of deflection voltages, which limits the field of view of the ion beam at certain magnification settings, a set of deflection voltages from the x and y channels is associated with a point in the field of view. Although the slope of the waveforms can be kept constant, the starting point will be different, if the initial deflection voltage is different.

Straight line scans can also be created. By changing the length of scan lines, some 3-D craters with non-linear boundaries can be machined with straight line scans. For example, varying the length of scan lines based upon desired boundary functions, a circular crater or disk can be produced, by placing scan lines either inside of the circular boundary or outside, respectively. The trace of the scan lines is shown in Fig. 3.2.

3.2.2.2 Rectangles

If we choose the frequencies of the x and y ramp signals differently, for instance, the frequency in x channel is 100 times as high as the one in y, then the ion beam will be scanned along x axis 100 times faster than along y axis, and the size of the line will be dependent upon the voltage swinging in the ramp signal. In other words, the ion beam will be scanned across a certain distance along the x axis, while the y position is increased a little, and after the ion beam is scanned across 100 lines along x axis with 100 different y values, the y waveform has completed one frame. If the voltage swings are the same in both x and y channels, then a square pattern will be obtained.

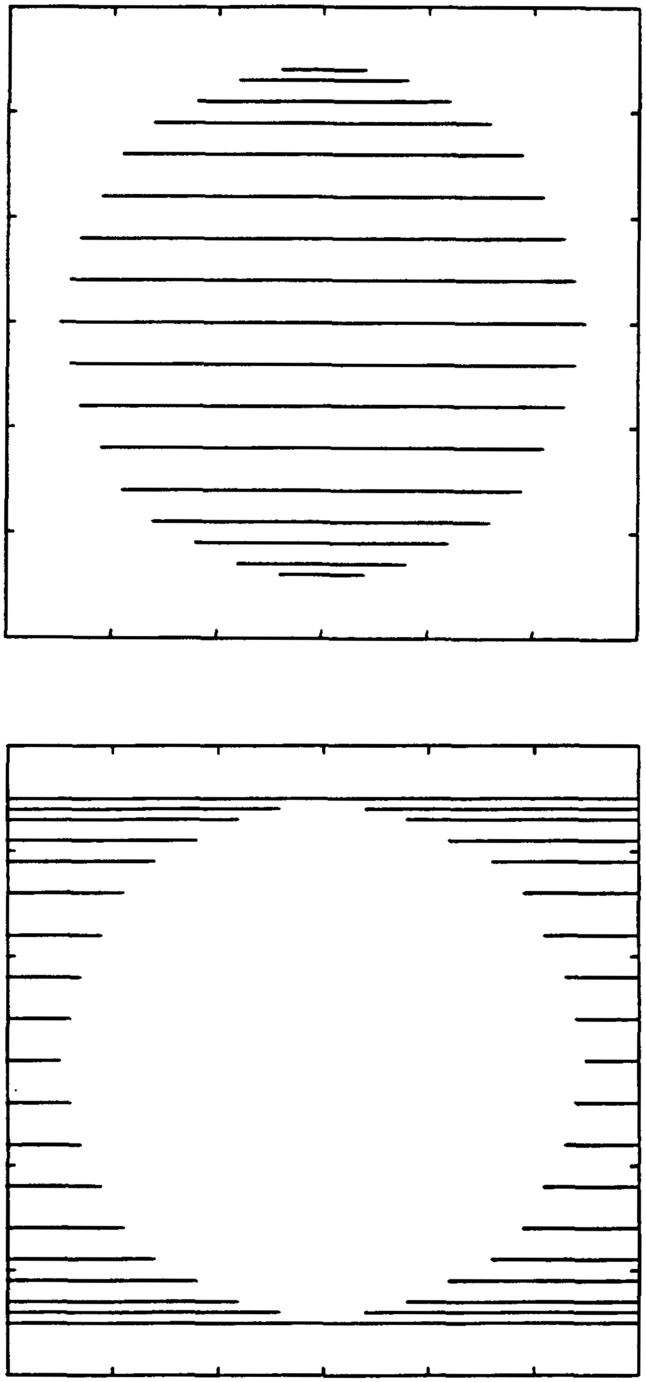

Figure 3.2 By altering the width of straight scan lines, 3-D structures, with arbitrary boundaries based upon desired boundary functions, can also be created, such as (a) Upper: a circular crater and (b) Lower: a circular disk.

In order to machine this rectangular crater with a uniform depth profile, the space between those scan lines must be less than one ion beam radius (0.125 μm), i.e. for a $12.5\mu m \times 12.5\mu m$ square machined crater with a uniform depth profile, x and y frequencies must be at least 100 times different. As shown in Fig. 3.3, the first saw-tooth line is the x ramp waveform, the second triangular line is the y ramp waveform, which are plotted in time abscissa and voltage ordinate, respectively, and the third part of this diagram is the actual scan trace of the ion beam in x and y spatial coordinates which will, in principle, machine a rectangular crater with a uniform depth profile. Note that voltage swings from highest to lowest level are extremely fast compared to the voltage changes from lowest to highest level. Thus, in the retrace of the ion beam from one end of scan lines to the start of the next line, removed material by the ion beam should be negligible. This must be true as well for the end of the last line to the start of the first line.

Furthermore, by altering the width of narrow rectangular scan regions, 3-D structures, with arbitrary boundaries based upon desired boundary functions, can also be created. As the narrow rectangular scan regions show in Fig. 3.4(a) and (b), a circular crater and disk can be machined.

3.2.3 Non-linear depth profiles

A natural way to make a surface emitting semiconductor diode laser is to fabricate a 45°, "V" or parabolic deflecting mirror in the laser waveguide, which could deflect the laser light out from the wafer surface. On the other

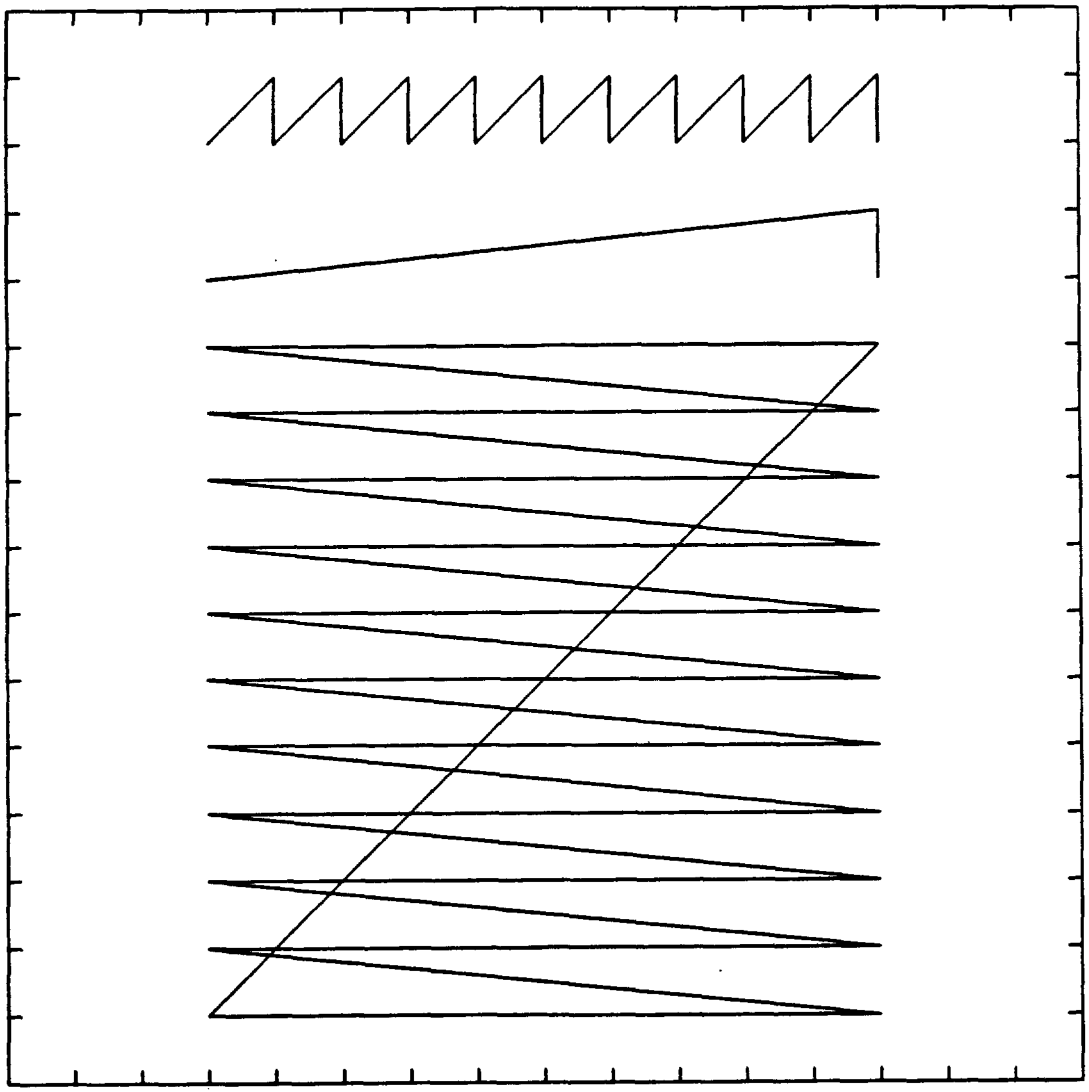

Figure 3.3 A rectangular crater could be produced using ramp signals with different frequencies in the x and y channels. The frequency of the x ramp signal (first curve from the top) is 10 times as high as the y signal (second curve from the top). And the third curve is the trajectory of the path function in the xy plane.

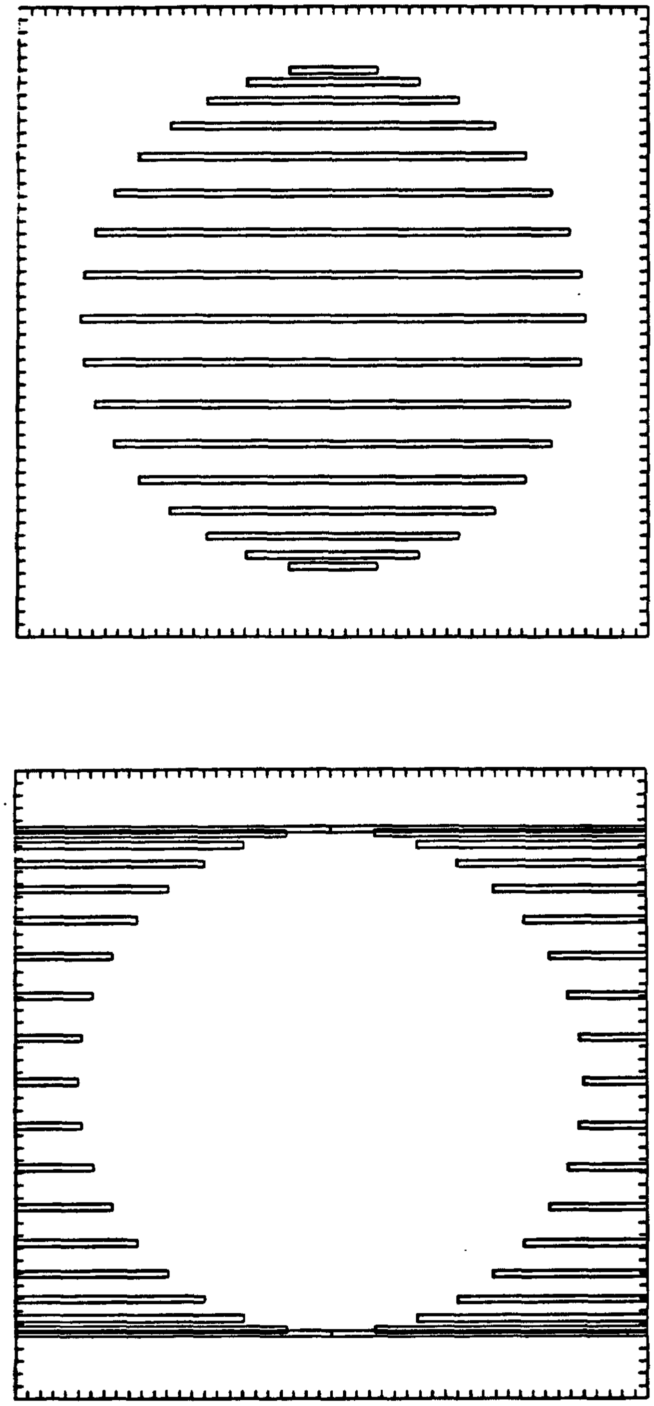

Figure 3.4 By altering the width of narrow rectangular scan regions, 3-D structures, with arbitrary boundaries based upon desired boundary functions, can also be created, such as (a) Upper: a circular crater and (b) Lower: a circular disk

hand, the focused ion beam has the ability to sputter any materials literally. Therefore, for this type of application, there is a need for machining a crater with a desired depth profile, other than a flat bottomed one. As various researchers have suggested[38,80], the ion beam should be scanned in a series of successively narrower overlapping rectangular regions. By only shrinking one side of these rectangles, a 45° deflecting mirror could be made. Meanwhile, by shrinking both sides of the rectangles, a "V" or parabolic deflecting mirror could be fabricated, too[35].

As we know from the previous chapter, the depth of a crater is also proportional to the ion beam dwell time. Therefore, by altering the dwell time according to certain patterns, arbitrary depth profiles could also be produced.

3.2.4 Discussion

Using ramp signals generated by any signal generators, an ion beam can be scanned along a fairly wide selection of path functions by varying the waveforms, frequencies, and voltage swings. Because the frequency of the ramp signals is so high, of the order of 100 kHz, it is impossible to change any setting of the waveforms frame by frame. Therefore, this raster scan technique is limited by the intrinsic functions of the signal generators: once the signals are applied, the ion beam will be scanned according to the preset waveforms. In contrast, there is no such problem in the digital scan, although digital scan has its own problems, such as lack of accuracy, nonuniformity, and etc., see next section.

In addition, by altering the dwell time, structures with fairly arbitrary surface contours can also be produced. However, altering the dwell time will result in local non-uniformity of depth profiles, which will enhance the secondary effects[83-85].

3.3 Scan Positions Determined by a Given Path Function

3.3.1 Introduction

To scan an ion beam along a curved path, one has to change positions of the ion beam according to the path function. In other words, we have to find a set of scan points (x_p, y_p) for a given path function, as described in our computer simulation (chapter 2). As mentioned earlier, there are two scan methods commonly used to control the ion beam positions, i.e. the digital (discrete) scan by discrete voltage signals from DAC's, and the continuous scan by analog voltage signals from ramp generators. Due to the fact that deflection voltages in both x and y channels are the only controllable variables in most FIB systems, a scheme of scanning the ion beam along any curved path, controlled by x and y deflecting voltages, has to be chosed according to the path function.

In the digital scan mode, the ion beam can be easily scanned along any path function, because of the ability of individually addressing the ion beam. Naturally, the ion beam could be scanned by stepping uniformly in the x

direction and non-uniformly in the y direction, according to the path function. However, a non-uniform scan speed along the arc would be produced by the above scan strategy, which would result in a non-uniform depth profile along the arc, due to the fact that the non-uniformity of the separations between scan points would result in non-uniformity of the ion dose when slopes of the path function were not uniform throughout the ion beam scan region. In other words, the adjacent scan points would be closer at lower slope region of the path function than at higher slope region. Therefore a strategy of scanning ion beam, which can uniformly move the ion beam along a curved path, needs to be established.

In the continuous scan mode, the input deflecting voltages are varyed continuously, because the analog ramp signals from any signal generator are continuous functions of time, in contrast to digital scan for which the voltages are changed in a discrete manner. Thus the changes of deflecting voltages in time, i.e. the ion beam scan speeds, are the only controllable parameters. To scan the ion beam along any curved path, we have to change the arc scan speed, according the path function, by superposing x and y scan speeds instantly. Therefore, the arc-scan-speed of the ion beam has to be derived in terms of the x and y scan speeds.

3.3.2 Derivation

At first we will derive a general formula for arc-scan-speeds as functions of x and y scan speeds and then derive equations for both digital scan and continuous scan cases from this general formula. Because arc-scan-speeds are governed by slopes of a path function at any point along the path, the path function has to be differentiable, at least in the first order approximation. In other words, the first order derivative of the path function must exist. For any differentiable path function $y = f(x)$, the arc scan speed $\frac{ds}{dt}$ is controlled by choosing appropriate values for $\frac{dx}{dt}$ and $\frac{dy}{dt}$.

Let

$$f'(x) \equiv \frac{dy}{dx}, \tag{3.1}$$

$$ds = \sqrt{dx^2 + dy^2}, \tag{3.2}$$

$$ds = \sqrt{1+(f')^2}\,dx, \tag{3.3}$$

therefore,

$$\frac{dx}{dt} = \frac{ds/dt}{\sqrt{1+(f')^2}}, \tag{3.4}$$

$$\frac{dy}{dt} = \frac{f'\,ds/dt}{\sqrt{1+(f')^2}}, \tag{3.5}$$

where $\frac{dx}{dt}$ and $\frac{dy}{dt}$ are the actual scan speeds in the x and y directions. Therefore the x and y scan speeds are determined by the arc-scan-speed $\frac{ds}{dt}$ and the first order derivative f' of the path function. Note that even if we keep $\frac{ds}{dt}$ constant, i.e. making uniform depth profiles, but $\frac{dx}{dt}$ and $\frac{dy}{dt}$ will not be constant, and will change point by point according to f', i.e. the path function. The Eqns. (3.4) and (3.5) are ready to be used in continuous scan mode.

With 12-bit DAC's, one can program the ion beam with 4096 $\times$ 4096 resolution, allowing a fairly arbitrary path to be used to produce a complicated 3-D feature. In digital scan mode, the definition of the scan speeds has to be modified in order to reflect how the ion beam is scanned digitally. The computer usually issues two instructions to DAC's in the x and y channels to deliver a pair of deflection voltages. Until the next series of instructions is issued, i.e. after a dwell time dt, the ion beam will stay in a position associated with the initial voltage settings. The beam then moves to the next point; the time spent on issuing or receiving any instructions is negligible compared to the dwell time dt. Therefore the scan speed should be defined as the ratio of the separation of two adjacent scan points Δs to the dwell time Δt spent on each scan point.

With a new definition of scan speeds, in the digital scan mode, the equations for x and y scan speeds as a function of the arc-scan-speed, can be rewritten as the following,

$$\frac{\Delta x}{\Delta t} = \frac{\Delta s/\Delta t}{\sqrt{1+(f')^2}}, \tag{3.6}$$

$$\frac{\Delta y}{\Delta t} = \frac{f'\Delta s/\Delta t}{\sqrt{1+(f')^2}}. \tag{3.7}$$

By multiplying both sides of Eqns. (3.6) and (3.7) by Δt, we can cancel the effect of dwell time in our present scan strategy,

$$\Delta x = \frac{\Delta s}{\sqrt{1+(f')^2}}, \tag{3.8}$$

$$\Delta y = \frac{f' \, \Delta s}{\sqrt{1+(f')^2}}. \tag{3.9}$$

In other words, we do not have to alter the dwell time at each scan point, but only change the separation of adjacent scan points Δs, so as to machine structures with desired depth profiles, as explained in the next section. Obviously, if we want to create features with uniform depth profiles, we have to keep the separation between scan points Δs constant, as the case for the fabrication of most semiconductor diode laser devices and for failure analysis on IC's.

Keeping the separation Δs constant is equivalent to stepping the ion beam with equal distance along the curved path, which is the actual implementation of the digital scan strategy in our FIB system. Thus a set of scan points (x_p, y_p) can be obtained for computer simulation or for scanning the real ion beam as follows,

$$x_{p_{i+1}} = x_{p_i} + \frac{\Delta s}{\sqrt{1+(f')^2}}, \tag{3.10}$$

$$y_{p_{i+1}} = y_{p_i} + \frac{f' \, \Delta s}{\sqrt{1+(f')^2}}, \tag{3.11}$$

where (x_{p_i}, y_{p_i}) is the scan point along any path function $y = f(x)$.

3.3.3 Discussion

A look-up table of $\frac{dx}{dt}$ and $\frac{dy}{dt}$ in continuous scan mode, or (x_p, y_p) in digital scan mode, will be respectively generated by Eqns. (3.4) and (3.5) or (3.10) and (3.11), prior to the actual FIB micromachining. Then the ion beam will be scanned according to this look-up table.

The drawback of the digital scan is that the ion beam has to be scanned in a discrete manner, for which the accuracy is limited by the resolution of DAC's. On the other hand, the digital scan is easy to use and to be implemented on any computer with good resolution DAC's.

Although the continuous scan seems to be mathematically impressive, changing the shape of ramp waveforms instantly along the curved path is very difficult to implement.

3.4 Depth Profile as a Function of Scan Speeds

3.4.1 Introduction

Now we come to the second part of the variable-scan-speed ion beam scan strategy. In the previous section, we have derived the equations for scan speeds $\frac{dx}{dt}$ and $\frac{dy}{dt}$, as functions of arc-scan-speed $\frac{ds}{dt}$. Changing these scan speeds we can scan the ion beam along any curved path. However, for certain applications, non-uniform depth profiles may be desirable. For instance, shaped gratings can be used to improve the characteristics of the DBR-GSE lasers. Therefore, $\frac{ds}{dt}$ as a function of desired depth profiles will be derived, which can be used to micromachine real three-dimensional structures.

3.4.2 Derivation

From Eqn. (2.1), smallest volume dv of sputter-removed material is equal to $dv = K\sigma^2 dt$, which is the basic element of any machined structures. In other words, to create a structure by a focused ion beam, we have to remove material element by element. Furthermore, the total volume of any micromachined structure by this Gaussian beam is equal to $NIdv$, where N is the number of scans and I is the number of small Gaussians in one scan. The separation of each small Gaussian Δs will determine the shape of the machined crater. After all, the structures machined by the Gaussian beam, and equivalently by the real ion beam, cannot be mathematically flat. We have to take our simulated structures as the sum of many small Gaussians, and then derive some useful and meaningful strategies to guide our actual FIB micromachining. To develop a scan strategy for machining structures with desired (arbitrary) depth profiles, we will first study scan strategies for machining features with uniform depth profiles, then derive the scan strategy that can be applied to general cases.

3.4.2.1 Overlapping Gaussians

By uniformly overlapping many small Gaussians, the sum of them will yield a structure with a fairly uniform depth profile, if the overlap is sufficient. As described in section 2.3.6, if we assume that the Gaussian beam is scanned along the x axis (where $y_p = 0$) in such way that the separation of two adjacent scan points is Δs, and that the etch rate K is constant, then after N scans the depth profile of this simulated straight line groove will be

$$Z(x,y) = \frac{NK}{2\pi}\sum_{i}^{I}\exp\left(-\frac{(x-i\Delta s)^2+y^2}{2\sigma^2}\right)\,dt, \tag{3.12}$$

where I is the number of total scan points in the straight line. Therefore the total volume of this simulated crater is $NIdv$, where dv is the volume element.

Because of restrictions of constant length and uniform depth profile, we have to keep the total volume constant, and keep the separation Δs less than one beam radius σ in order to achieve the uniform depth profile. However, changing Δs means that the number of scan points I is going to be changed, thus NI has to be constant in order to keep the total volume constant. Although, structures with constant height and length can be machined when applying different scan strategies, the shapes are not exactly the same. As shown in Fig. 3.5, four different separation values Δs (i.e. 2σ, $\frac{3}{2}\sigma$, σ and $\frac{\sigma}{2}$) have been used. Therefore, altering the separation Δs is a measure for creating 3-D structures with desired (arbitrary) depth profiles.

3.4.2.2 Separation of scan points Δs

In order to avoid the non-uniformity caused by insufficient overlapping Gaussians, we will restrict the separation Δs to less than $\frac{3}{2}\sigma$. Because under this condition a uniform depth profile has been produced, as shown in Fig. 3.5. According to the analysis in the previous section, it is possible to machine structures with arbitrary depth profiles by combining different values of separation Δs. To study the relation between separation of scan points Δs and depth profiles $z(s)$, we have to know how Δs affects the shape of machined craters.

The equation of a cross-section of the small Gaussian at $z = \dfrac{K\ dt\ e^{-1/2}}{2\pi}$ is given as follows,

$$(x - x_p)^2 + (y - y_p)^2 = \sigma^2, \tag{3.13}$$

where the volume of this cylinder is close to one half volume of the small Gaussian dv. The area scanned by the Gaussian beam is equal to twice the

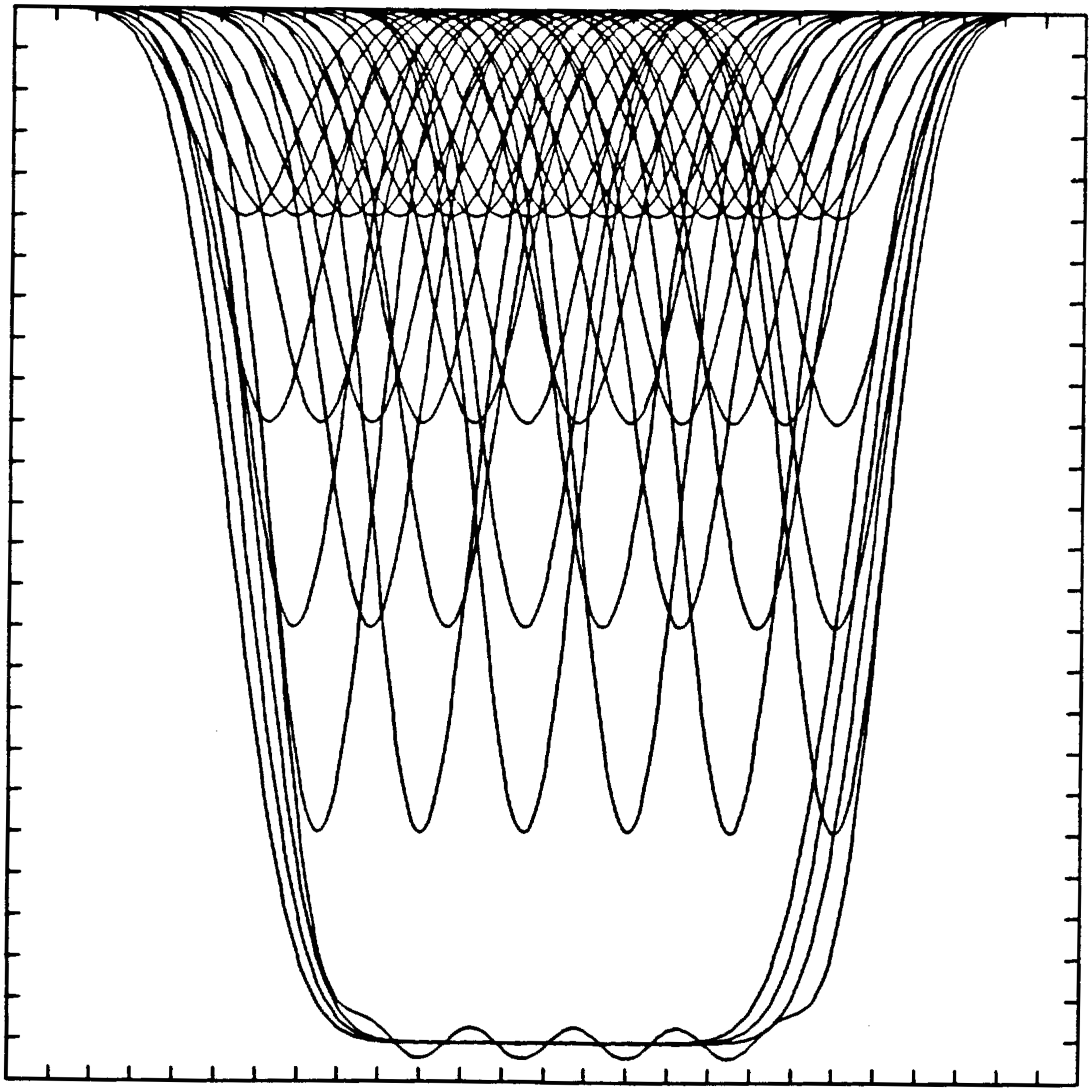

Figure 3.5 Cross-sectional depth profiles of simulated grooves by scanning a Gaussian beam with different separations between adjacent scan points for different dwell time. Small Gaussians represent locations of the scan points. The greater the depth of small Gaussians, the longer the dwell time, and the larger the separations, in order to keep the average depth of the simulated grooves constant. The separations for the small Gaussians (from shallow to deep) are varied from $\frac{\sigma}{2}$ to 2σ in $\frac{\sigma}{2}$ intervals.

area of the two circles minus the overlapped area. The overlapped area is equal to $\sigma^2 \left[2\cos^{-1}(\frac{\Delta s}{2\sigma}) - \frac{\Delta s}{\sigma}\sqrt{1 - (\frac{\Delta s}{2\sigma})^2} \right]$. If two circles are separated for four different separation values: $\frac{\sigma}{2}$, σ, $\frac{3}{2}\sigma$ and 2σ, then the overlapped areas are 2.15, 1.23, 0.45 and 0. (multipled by σ^2), respectively. However, from Fig. 3.5, we have seen that having sufficiently overlapping small Gaussians, $\Delta s \le \frac{3}{2}\sigma$, the depth profiles were fairly uniform. Therefore, we choose the separation $\Delta s = \sigma$ as a basic value. In machining different depth profiles, for deeper craters we choose $\Delta s < \sigma$, and for shallower ones we use $\Delta s > \sigma$. As a matter of fact, we also use this basic separation value to scan the ion beam on unknown materials in order to calibrate the etch rate K. Thus a small volume cell ΔV of removed material (at the shortest scan distance, where the depth profile is approximatively uniform for such short scan distance) is a function of dwell time Δt. According to Eqn. (2.1), we obtain:

$$\Delta V = (2\pi - 1.23)\, \sigma^2\, Z(s) = N\, K\, \sigma^2\, \Delta t, \tag{3.14}$$

where $(2\pi - 1.23)\, \sigma^2 = A_\sigma\, \sigma^2$ is the scanned area for separation $\Delta s = \sigma$, and N is the total number of scans, (i.e. the total number of smallest volume elements)r, A_σ is an overlap factor. When A_σ increases (i.e. less overlap), the depth $Z(s)$ decreases, if the total volume is constant. By substituting $z(s) = \frac{Z(s)}{N}$, we have,

$$A_\sigma \, \Delta s \;\, z(s) = K \, \sigma \, \Delta t, \tag{3.15}$$

$$\frac{\Delta s}{\Delta t} = \frac{K \, \sigma}{A_\sigma \, z(s)}. \tag{3.16}$$

According to the modified definition of scan speed along arc in section 3.3.2, one may derived a semi-empirical approach to scan speed along arc $\frac{ds}{dt} = \frac{\Delta s}{\Delta t}$ as a function of depth profile $z(s)$. In principle, this semi-empirical approach can be used in both continuous scan and digital scan modes, but we will restrict its usage in digital scan mode.

By defining $\frac{ds}{dt}$ as a function of $z(s)$, see Eqn. (3.16), and $\frac{dx}{dt}$, $\frac{dy}{dt}$ as functions of $\frac{ds}{dt}$, see Eqns. (3.4) and (3.5), a 3-D digital scan strategy can be obtained to machine any 3-D structures with desired path functions and depth profiles.

$$\frac{dx}{dt} = \frac{K \, \sigma}{A_\sigma \, z(s) \sqrt{1+(f\,')^2}}, \tag{3.17}$$

$$\frac{dy}{dt} = \frac{f\,' \, K \, \sigma}{A_\sigma \, z(s) \sqrt{1+(f\,')^2}}, \tag{3.18}$$

where $s = \int_{x_0}^{x_1} \sqrt{1+(f\,')^2} \, dx$, according to Eqn. (3.3).

A look-up table of x and y scan speeds generated by Eqns. (3.17) and (3.18), can be used to scan the ion beam, while x and y deflection voltages are controlled by ramp generators. On the other hand, the deflecting voltages can also be controlled by DAC's, and thus digital scans can be achieved. In digital scan mode, because positions of the ion beam are the controllable variables, while the scan speeds are not, changes have to be made in Eqns. (3.17) and (3.18).

$$\Delta x = \frac{K \, \sigma \, \Delta t}{A_\sigma \, z(s) \sqrt{1+(f\,')^2}}, \tag{3.19}$$

$$\Delta y = \frac{f\,' \, K \, \sigma \, \Delta t}{A_\sigma \, z(s) \sqrt{1+(f\,')^2}}, \tag{3.20}$$

Therefore, we obtain

$$x_{i+1} = x_i + \frac{K \, \sigma \, \Delta t}{A_\sigma \, z(s) \sqrt{1+(f\,')^2}}, \tag{3.21}$$

$$y_{i+1} = y_i + \frac{f\,' \, K \, \sigma \, \Delta t}{A_\sigma \, z(s) \sqrt{1+(f\,')^2}}, \tag{3.22}$$

where (x_i, y_i) is the position address of the DAC's and Δt is dwell time per pixel. At OGI's present FIBM workstation we have employed 12-Bit DAC's to control x and y deflecting voltages, which enables us to generate a map of 4096 x 4096 pixels in the xy plane, and to produce a complicated 3-D feature along a fairly arbitrary path. For example, a circular path in a 50 $\times$ 50 grid is illustrated in Fig. 3.6 to explain this concept.

In the case of simulation, a Gaussian beam can also be scanned by varying the position (x_p, y_p) according to the look-up table, as described in the previous chapter, to simulate the FIB micromachining of these 3-D structures.

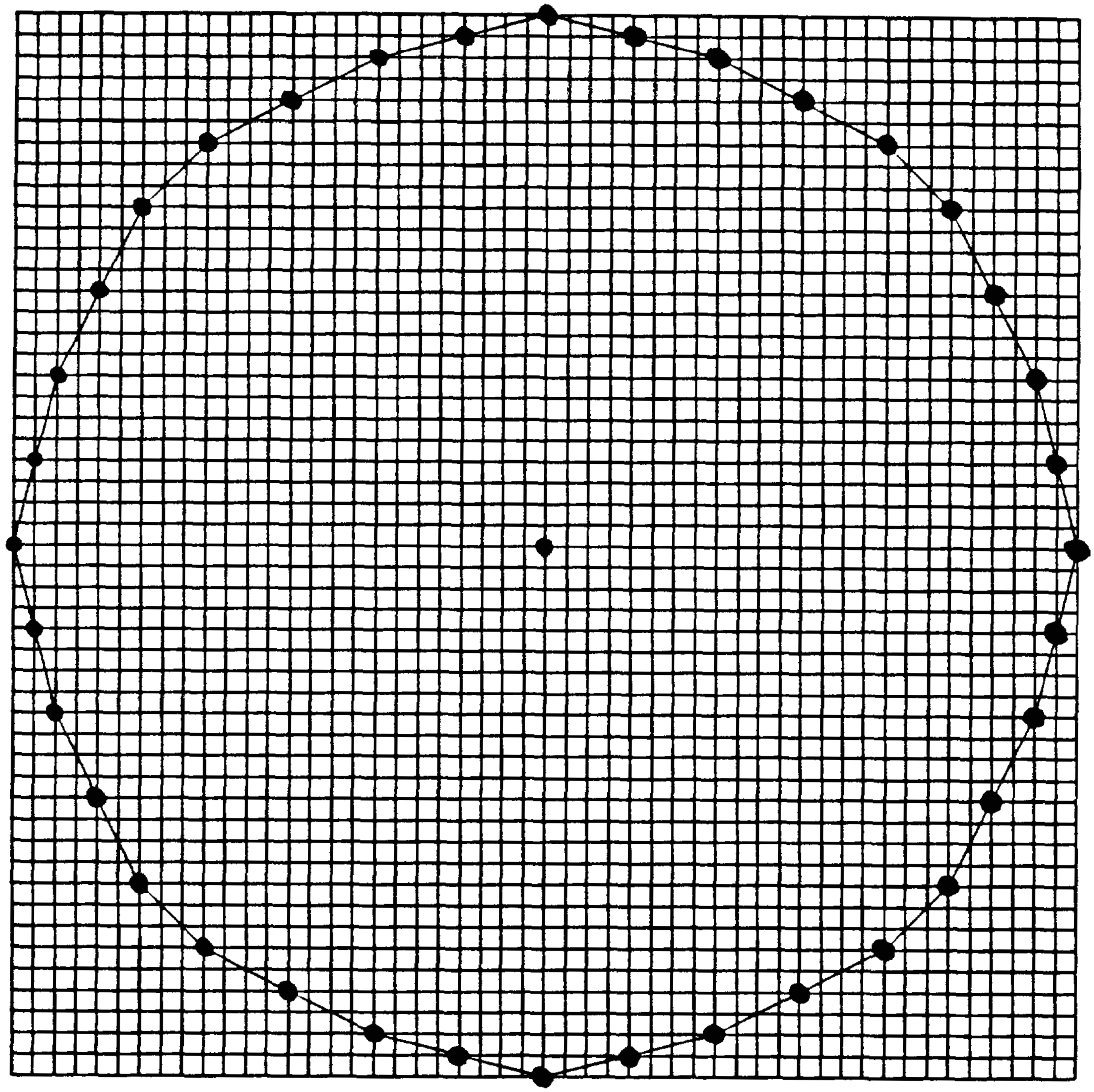

Figure 3.6 A sequence of solid dots, in a down-scaled DAC's bit map of 50×50, represents the bit address of scan points, in the xy plane, to produce a circular crater.

As a comparison to the constant-scan-speed strategy, a simulated FIB micromachined circular crater with a *uniform* depth profile produced by a constant arc scan speed strategy, is illustrated in Fig. 3.7 for top view and inverted view. Furthermore, a 3-D circular crater with a sinusoidal depth profile, $z(s) = \sin(s) + 2 > 0$, has been simulated by choosing a variable arc scan speed $\frac{ds}{dt}$, as shown in Fig. 3.8. Such a 3-D simulation of FIBM can avoid any mistake in the ion beam scan strategy and can simulate any FIB micromachined structure before machining real devices.

3.4.3 Discussion

By changing the separation Δs based upon Eqn. (3.16), three-dimensional structures with arbitrary depth profiles $z(s)$ can be produced. A Gaussian beam has been scanned along the x axis using the same scan strategy to produce the crown shape as shown in Fig. 3.8, and the cross-section of this structure is shown in Fig 3.9, where non-uniformly distributed scan points have been indicated by many small Gaussians. The smaller Gaussians are crowded together, the greater the depth which will be produced. However, just like other ion beam scan approaches, this semi-empirical approach has its own limitation.

First of all, $z(s)$ must be greater than *zero* throughout the entire scan region, because of the micromachining is a process of removing material from substrates, rather than accumulating it in a deposition processes.

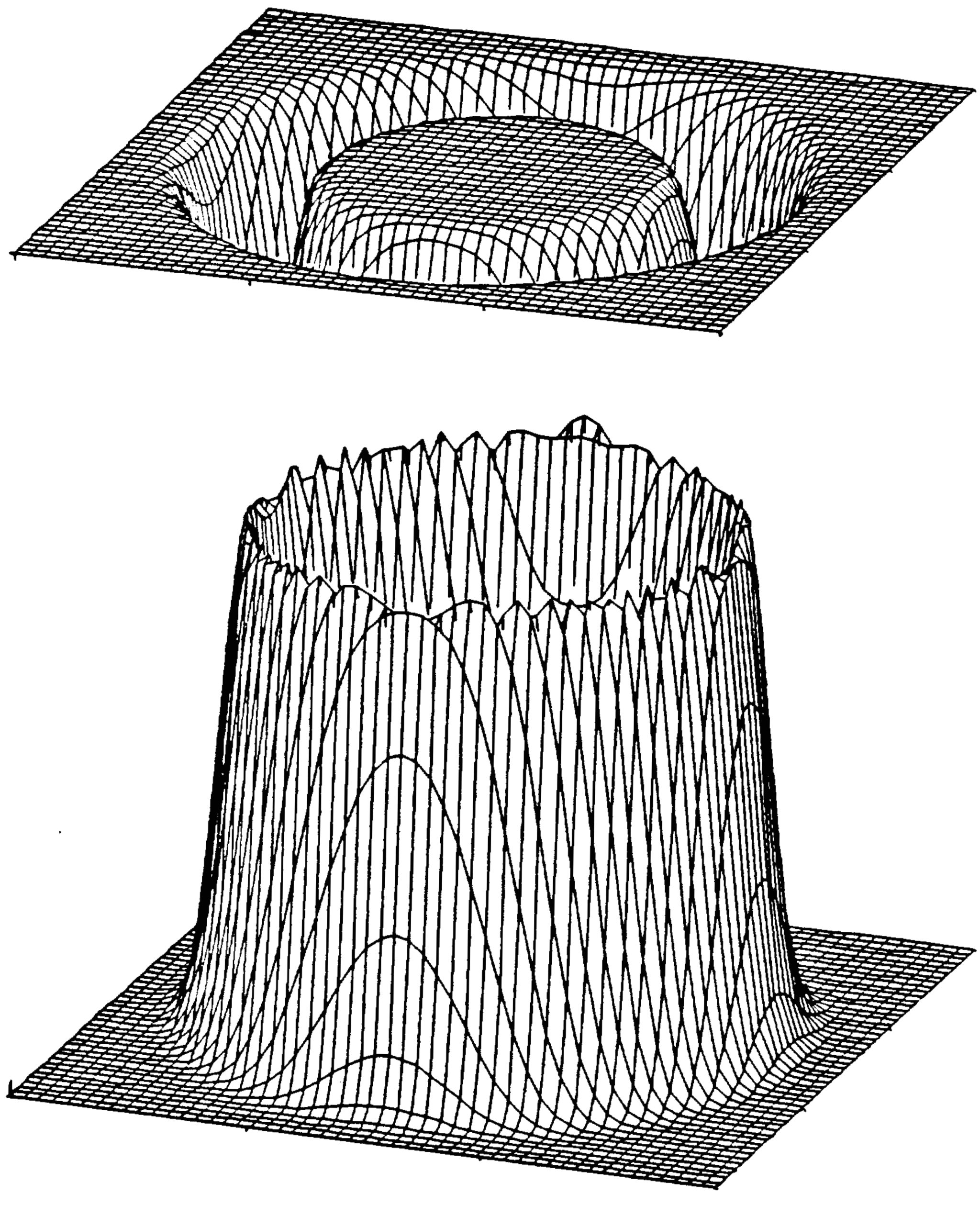

Figure 3.7 3-D top and inverted views of a simulated circular crater with a uniform depth profile, produced by constant scan speeds along the arc.

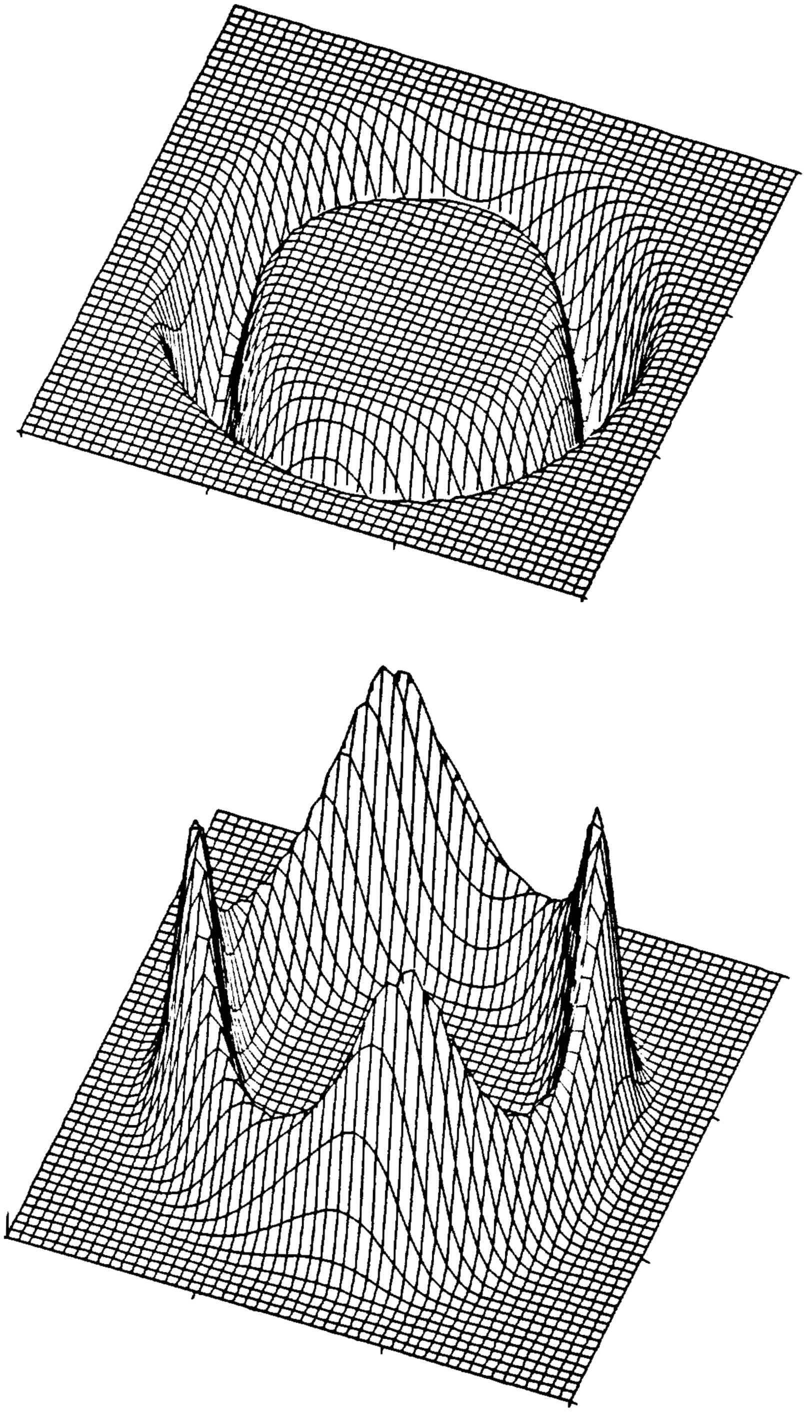

Figure 3.8 3-D top and inverted views of a simulated circular crater with a sinusoidal depth profile, produced by variable scan speeds along the arc.

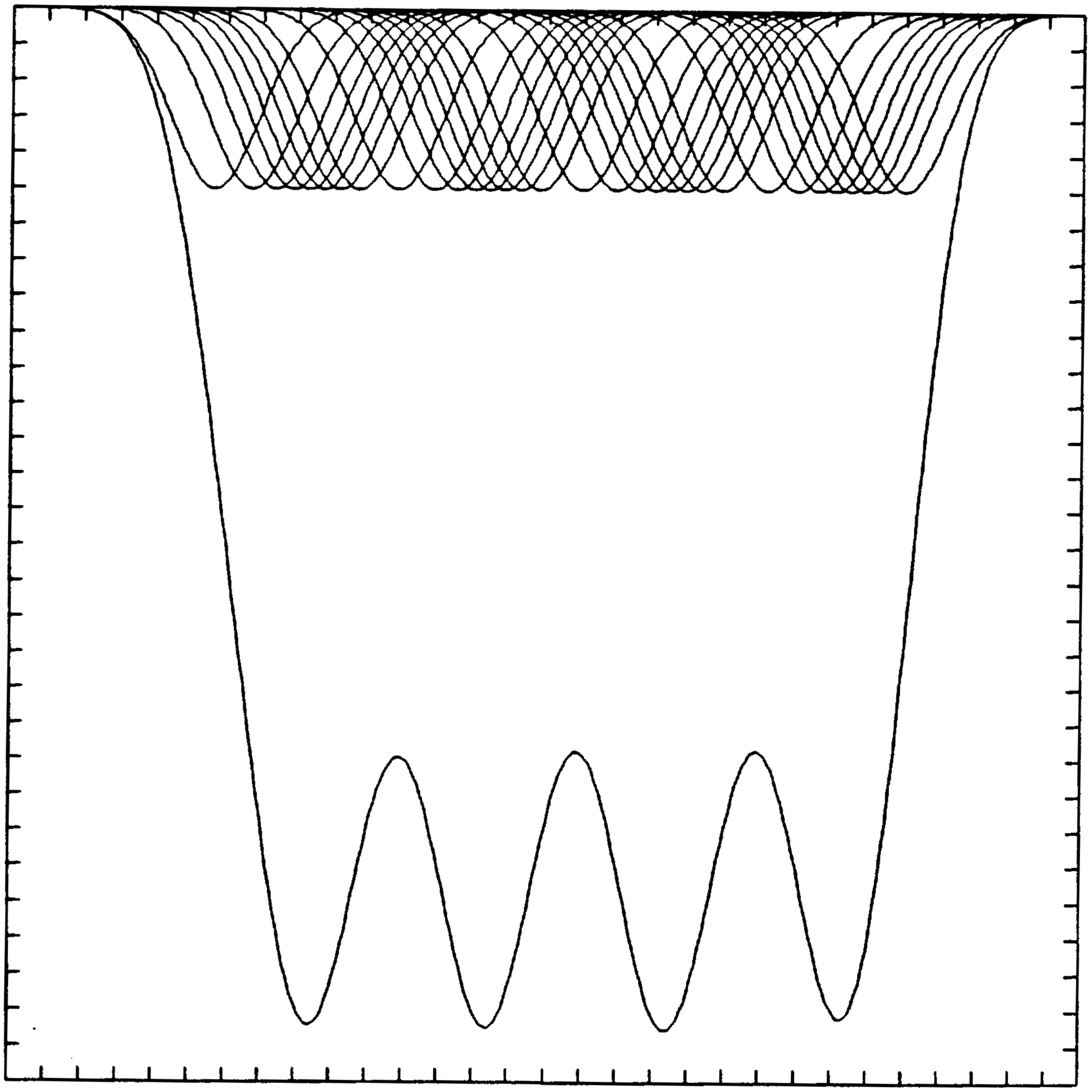

Figure 3.9 The depth profile along the arc of the crown structure (as shown in Fig 3.8) is shown, where small Gaussians represent the Gaussian beam at scan points (x_p, y_p) with variable separations.

Second, because the depth profile function $z(s)$ is one of the denominators in Eqn. (3.16), $z(s)$ cannot be close to *zero*, for example, if $z(s)$ is equal to 0.01 at some scan points, then Δs is equal to 100 σ approximatively, i.e. the ion beam would go outside the present machining area. An attempt to develop a scan strategy for the fabrication of 45° laser deflecting mirrors was put forward by using a depth profile $z(x) = 3.1 - x$ where $0.0 < x < 3.0$. However, the structure machined by the Gaussian beam with a cross-section shown in Fig. 3.10 was not exactly matched to the given depth profile. If the beam was moved in increments of 2.97σ, then the 45° slanted facet was curved near the shallow end of the crater. Furthermore, if the Gaussian beam were started at the shallow end of this crater, then this structure could not be machined, because at $x = 3.0$ the separation $\Delta s = 10\sigma$ would move the beam right into the middle of the crater.

Third, because the smallest volume element is of a Gaussian shape, no sharp corners can be machined by the beam. In fact, any depth profile function $z(s)$ with sharp corners (i.e. with discontinuous points in first order derivative of $z(s)$ function) will result in confusions in the scan strategy. In other words, such sharp corners will be fitted by the Gaussians, which will produce round corners with continuous first order derivative. Furthermore, as shown in Fig. 3.10, there was no right angle corner formed at the deep end of the 45° deflecting mirror structure. And a sharp 45° corner at the bottom of the crater appeared to be rounded out by the Gaussians. In spite of round corners formed by the Gaussian beam, by scanning the Gaussian beam in a series of successively narrower overlapping rectangular regions of one beam

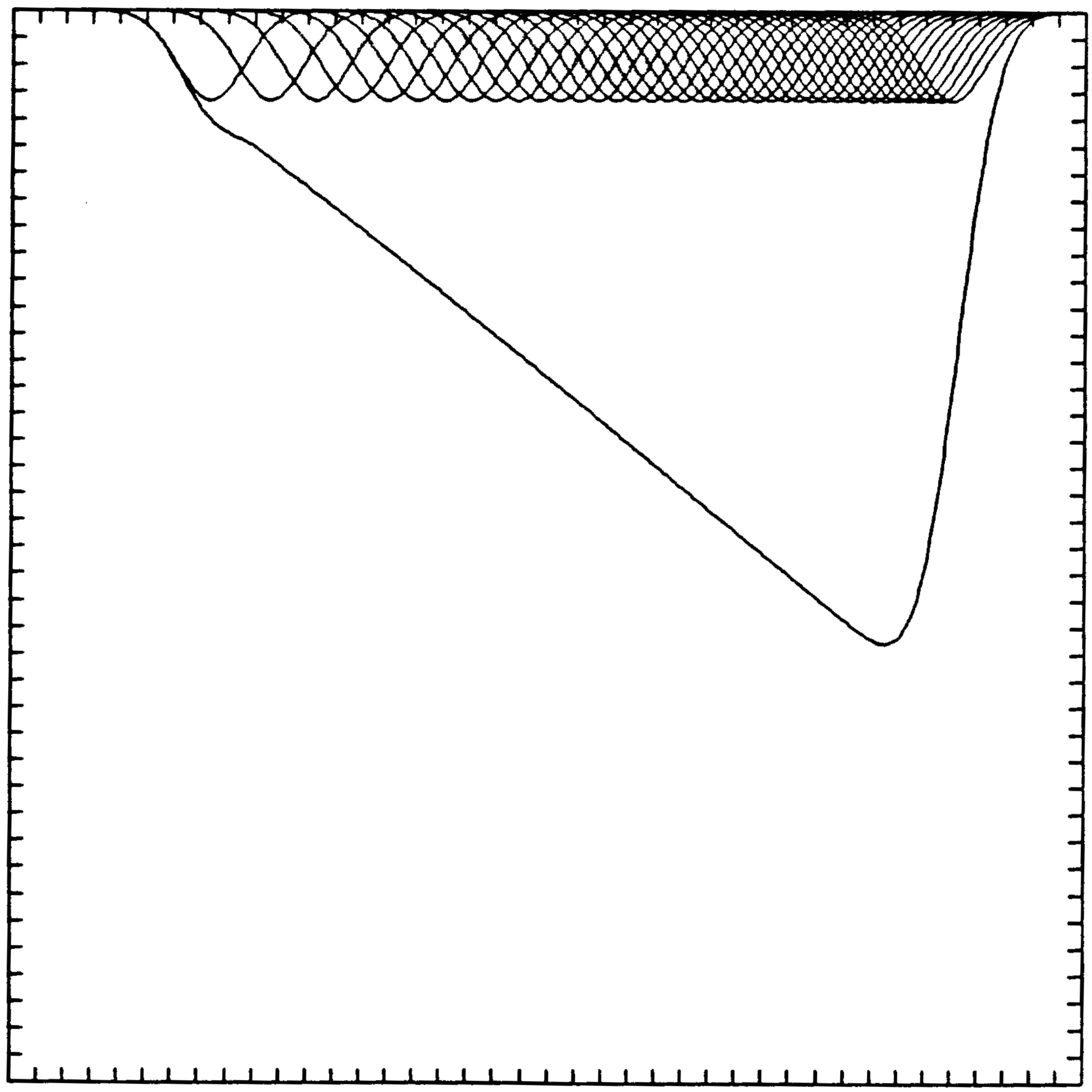

Figure 3.10 A simulated structure with a slanted surface has been produced by variable scan speeds, where small Gaussians represent the Gaussian beam at scan points with variable separations.

radius σ per rectangle, the 45° slanted structure will be machined closer to reality, as for the cross-section shown in Fig. 3.11. Note that in mathematics, shrinking the width of the rectangular scan areas is equivalent to increasing the dwell time at appropriate scan points. But for the purpose of eliminating secondary effects, we still recommand removing less material at each scan, i.e. shrinking the width of rectangles, rather than creating local non-uniformity in the depth profile, as in the variable dwell time scan strategy.

Finally, using such a scan strategy, some unsymmetrical structures will be made by symmetric depth profiles, because the scan strategy will choose the next scan point based upon the knowledge of depth function and derivative of the path function at present point; thus the scan point will most likely pass the symmetric center without being aware of it. For instance, using variable-scan-speed strategy, i.e. scanning the Gaussian beam based upon a depth profile

$$z(x) = \begin{cases} x + 2.5 & -2.0 < x < 0. \\ -x + 2.5 & 0. < x < 2.0 \end{cases}$$

one could machine a right angle "V" crater with two 45° slanted facets. As for the cross-section shown in Fig. 3.12, an unsymmetrical structure has been produced. As an alternative of creating such symmetric structures, by equally shrinking the width of rectangular scan areas at both end of rectangles one beam radius σ per scan, one could machine a nice symmetric "V" structure by using the Gaussian beam; the cross-section of this structure is shown in Fig. 3.13.

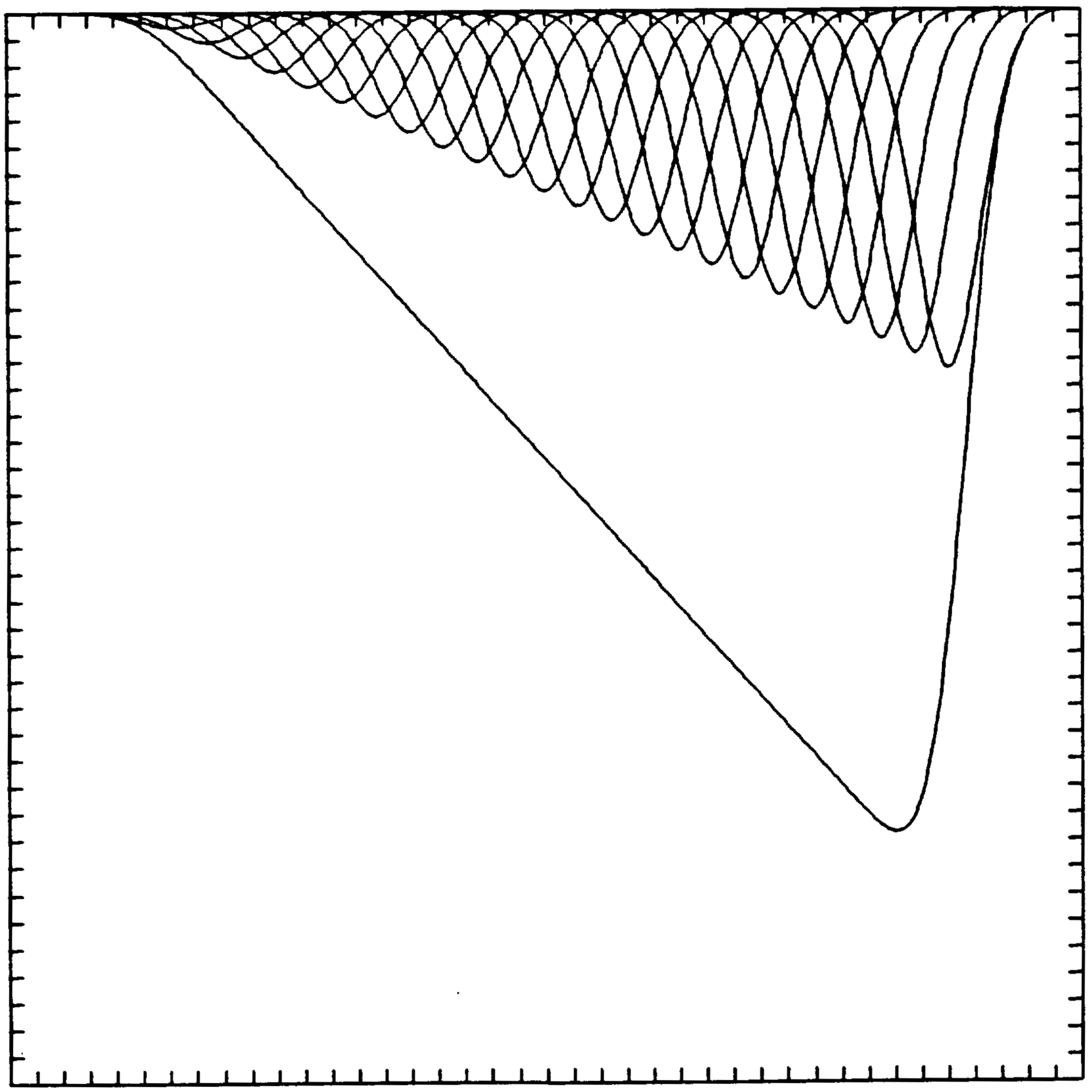

Figure 3.11 A simulated structure with a slanted surface has been produced by variable dwell time, where small Gaussians with different depths represent the Gaussian beam at scan points with constant separations, but for different dwell time.

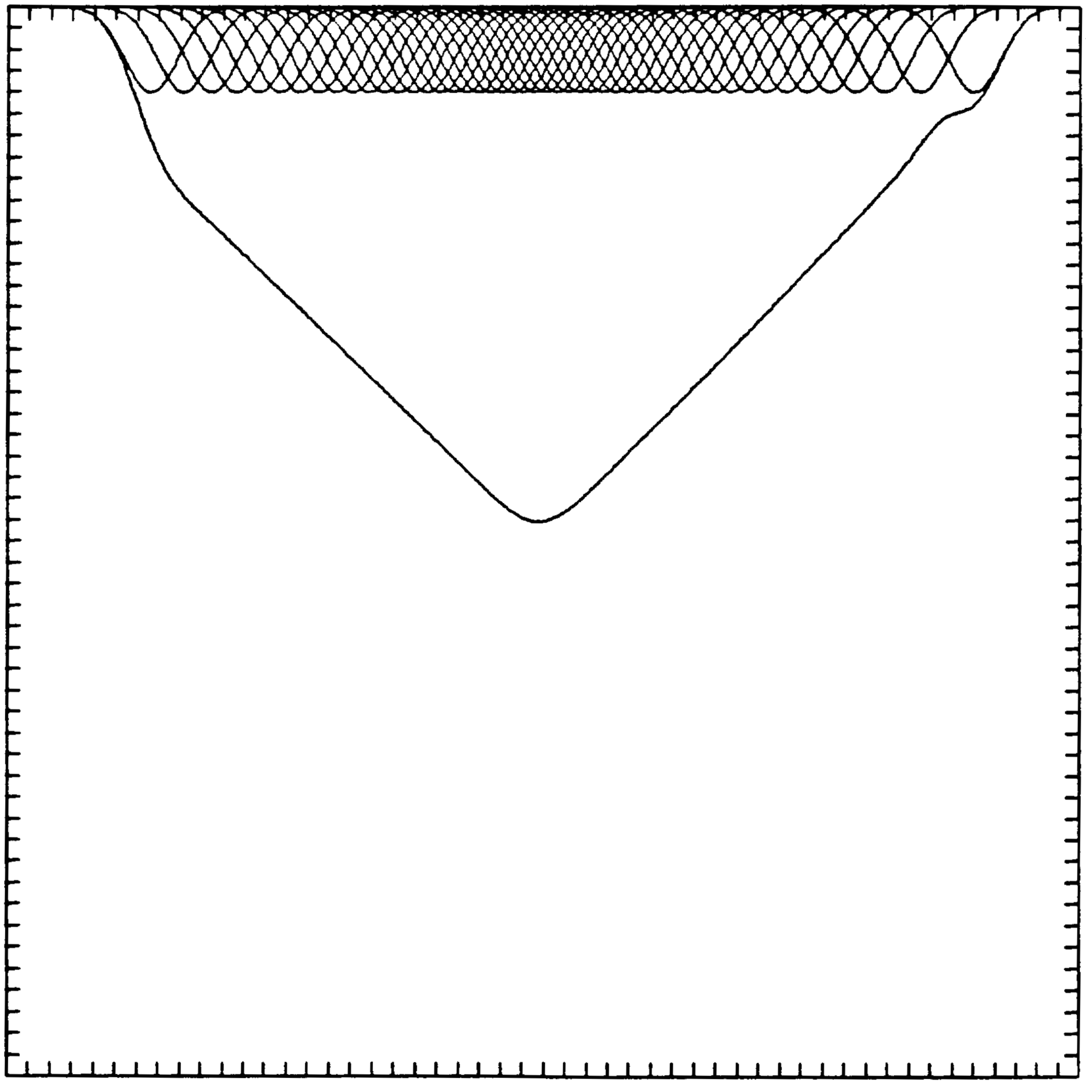

Figure 3.12 A simulated "V" groove has been produced by variable scan speeds, where small Gaussians represent the Gaussian beam at scan points with variable separations.

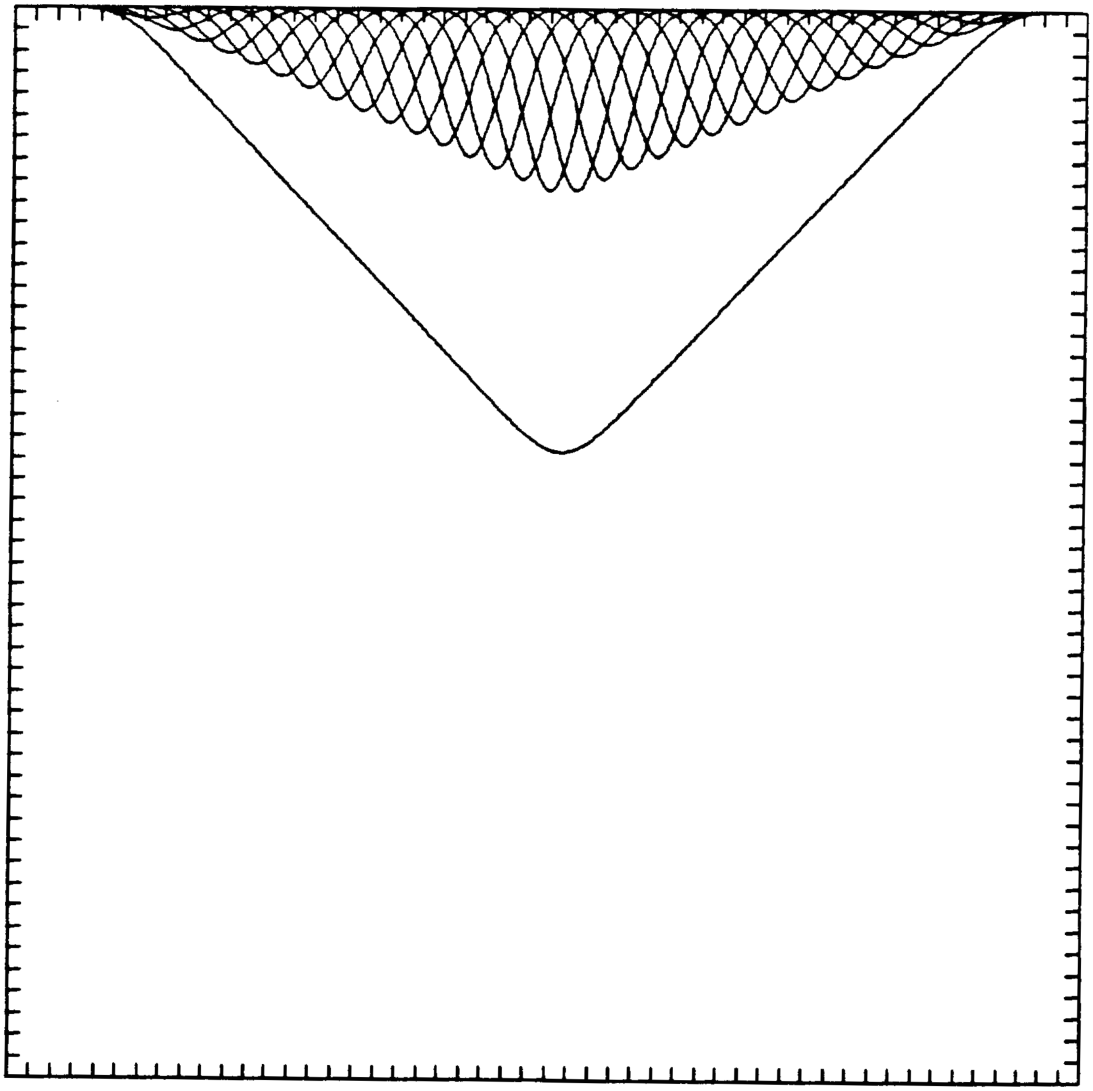

Figure 3.13 A simulated "V" groove has been produced by variable dwell time, where small Gaussians with different depths represent the Gaussian beam at scan points with constant separations, but for different dwell time.

In conclusion, with continuous first order derivative, any depth function can be used in the 3-D scan strategy to produce structures with depth profiles fairly close to the real one. Also by using the straight-line-scans strategy, i.e. scanning the Gaussian beam in a series of successively narrower overlapping rectangular regions, certain advantages for the fabrication of structures with symmetric depth profiles, (such as 45° slanted and "V" shaped profiles) could be achieved.

3.5 Conclusions

Various ion beam scan strategies, in both continuous and digital scans, have been studied extensively for fabricating a variety of semiconductor diode laser devices and for performing failure analysis on integrated circuits. Several examples have been investigated to show that to use improper or incorrect scan strategy would result in different depth profiles. One often wants laser reflecting mirrors with uniform depth profiles, because laser light can leak out in mirrors with non-uniform depth profiles. Electrical isolation grooves with non-uniform depth profiles are also undesirable.

Possibilities of creating three-dimensional structures for different applications have been explored. Based upon the variable-arc-scan-speed scan strategy, x and y scan speeds are the only controllable parameters in most FIB systems. Before the actual FIB micromachining a look-up table of the velocities $\frac{dx}{dt}$ and $\frac{dy}{dt}$ has to be calculated, and then the ion beam will be scanned correspondingly according to the desired path functions and depth profiles.

Advantages and disadvantages of continuous and digital scans have been investigated. The variable-scan-speed can be realized by continuous scans, which is difficult to be achieved practically by changing amplitudes, slopes, frequencies and shapes of ramp waveforms frame by frame. Therefore, the continuous scan technique is limited by the intrinsic waveforms of the signal generators. Even though arbitrarily curved scan paths can be easily traced out by digital scans, the accuracy is limited by the resolution of the DAC's.

The variable-scan-speed scan strategy has been derived under two major assumptions made in chapter 2, but more sophisticated computer simulations which take into account all secondary effects are still worth to be considered. Therefore, the main reason for developing different scan strategies is to explore the potential of FIB micromachining in order to create various 3-D structures for different applications.

4. VARIOUS FIB MICROMACHINED STRUCTURES

4.1 Introduction

In various applications of semiconductor device microfabrication, there has been increasing interest in focused ion beam (FIB) technology. In this chapter, we will discuss experimental aspects of FIB micromachining, such as the verification of the 3-D computer simulation, and the fabrication of various semiconductor diode laser devices, (based upon our 3-D variable-scan-speed strategy and described in chapter 3), and the limitation of the 3-D computer simulation.

A focused Ga^+ ion beam with less than $0.25\mu m$ diameter, has been used to fabricate structures with optically smooth surfaces[86], which serve as various laser mirrors[35], e.g. laser output mirrors[36], coupled-cavity oscillator mirrors[37], and laser deflecting mirrors[38]. All these mirrors have been made by using straight lines or rectangles with conventional 2-D raster scans, namely straight line scans. However, positioning the ion beam by both raster scans and digital scans is far more sophisticated than just making straight lines and rectangles (see chapter 3). By taking advantage of the 3-D computer simulation, one can "perform" FIB micromachining on a computer monitor to investigate the simulated structures, and then carry out the actual micromachining task on real devices by using the beam scan strategy produced by the computer simulation.

Therefore, we will start out this chapter with a verification of the previously described computer simulation of FIBM, and then will introduce various FIB micromachined structures which can be produced by the 3-D digital scan strategy. In section 4.2 the verification of computer simulations of FIBM techniques is described. In section 4.3, we will explain the fabrication process of several 3-D structures FIB micromachined by the 3-D digital scan strategy on OGIST's FIBM workstation, such as 45°, "V", micro-"V" and parabolic turning mirrors.

4.1.1 Description of hardware

FIB micromachining experiments (to be described later in this chapter) have been conducted in three in-house FIBM workstations and a FEI prototype FIB workstation employed with a two-lens ion gun. A schematic diagram of such FIBM workstation was illustrated in Fig. 1.1. In the FIBM workstation I, the model number of the ion beam deflector is 83-01, the high voltage power supply 83-02, and the single-lens ion gun 83. In FIBM workstation II, the model number of the ion beam deflector is 83-01, the high voltage power supply 83-02I, and the single-lens ion gun 83I. In FIBM workstation III, the model number of the ion beam deflector is 1D2, the high voltage power supply 2L1, and the two-lens ion gun 83-TLI/POST. Positions of the ion beam are controlled by a Heathkit (H-207) computer with a 12-bit 4-channel D-A converter (AOM-12).

4.1.2 Description of software

The operating system of the Heathkit computer is Z-Dos V1.10. The "C" compiler is OPTIMIZING C86 V2.10. Programs used to scan the ion beam in an arbitrary fashion will be described with source code in Appendix B. The basic structure of these programs is the following: the bit addresses of the 12-bit DAC's were calculated according to certain beam scan strategies, then two instructions would be issued by the computer to the 12-bit DAC's, which could send appropriate voltage signals to the x and y channels of the ion beam deflector. The instructions used to control the DAC's are the only machine dependent commands in the above-mentioned programs.

4.2 Structures micromachined by straight line scans

FIB micromachined structures now being successfully used in many applications, are made with straight line scans. This is because straight line scans are sufficient for many applications including the fabrication of integrated optical devices and microsurgery on integrated circuits. Straight line scans are easy to produce with either ramp generators or digital methods.

The simple straight line scans provide an excellent test of whether the assumption of a Gaussian depth profile is valid, because depth profiles are uniform along the scan lines. Such line profiles, obtained by cleaving wafers perpendicular to the direction of scan lines, will directly reflect the depth profile of the basic volume element as introduced in chapter 2, rather than the combination of scan effects discussed in chapter 3. Due to the nature of FIB micromachining, shapes of micromachined craters are strongly dependent upon the shape of the ion beam and the method of generating scans, in particular the separation between two adjacent scan points.

The etch rate K could be experimentally obtained by measuring the micromachined depth of shallow structures, such as single scan lines, gratings and rectangular craters. First, the term $K\Delta t$ would be set to unity in the simulation program, where Δt is the dwell time. The simulated structure was then calculated by using the same scan strategy as in the FIB micromachining. Second, the term $K\Delta t$ would be equal to the depth of the actual structure divided by the product of the depth of the simulated one and the total number of beam scans. Thus, the etch rate K could be derived for the DAC's used in the FIB micromachining experiment.

4.2.1 Verification of computer simulation by fabricating gratings

As in chapter 2, a Gaussian depth profile should be machined by a focused ion beam with a Gaussian current distribution when the depth aspect ratio of the crater is small. One way to ascertain the profile of the beam is to machine shallow grooves with single line scans with a small ion dose, then to cleave the substrate perpendicular to the line scan direction. Cross-sections of these grooves will give information about the shape of the basic volume element. For example, such an experiment has been carried out on GaAs. Using a focused ion beam with 25 keV energy and $0.25\mu m$ diameter in FIBM workstation II, we have micromachined a series of straight lines by single line scans in order to make grooves with the narrowest possible groove width. The cross-sections of these cleaved straight line grooves are shown in an SEM micrograph Fig. 4.1(a). In Fig. 4.1(b), the spot size (2σ) was varied from $0.15\mu m$ to $0.4\mu m$ in $0.05\mu m$ intervals for the simulated cross-sections, where σ represents the beam radius. The crater wall shape is steeper when $2\sigma = 0.15\mu m$, and more round when $2\sigma = 0.4\mu m$. This calibrated spot size ($0.25\mu m$) was used for the Gaussian beam to simulate micromachined structures. However, the cross-sections of the first two shallow grooves are wider than the cross-sections simulated by the Gaussian beam with a beam diameter of $0.25\mu m$. It is likely that these two grooves were accidently micromachined with a badly focused ion beam, because the focusing condition of the ion beam had changed, when the position of the wafer was altered in order to select different area where FIBM was needed. Thus, refocusing the ion beam would be required, if specimen stage was moved manually.

The depth of the first groove in Fig. 4.1(a), on the right side, is $0.73\mu m$, and the full width at half maximum is close to $2\sigma = 0.25\mu m$. A pseudo depth aspect ratio may be defined as the depth divided by the full width at half maximum, which in this case has a value of 2.9:1. Therefore, a conservative depth aspect ratio of less than 2:1 should be a safe limit for this computer simulation.

It is worthwhile considering whether shallow grooves micromachined by single line scans are of any real value for actual FIBM techniques. In fact, we can use this Gaussian beam approximation to simulate real FIB

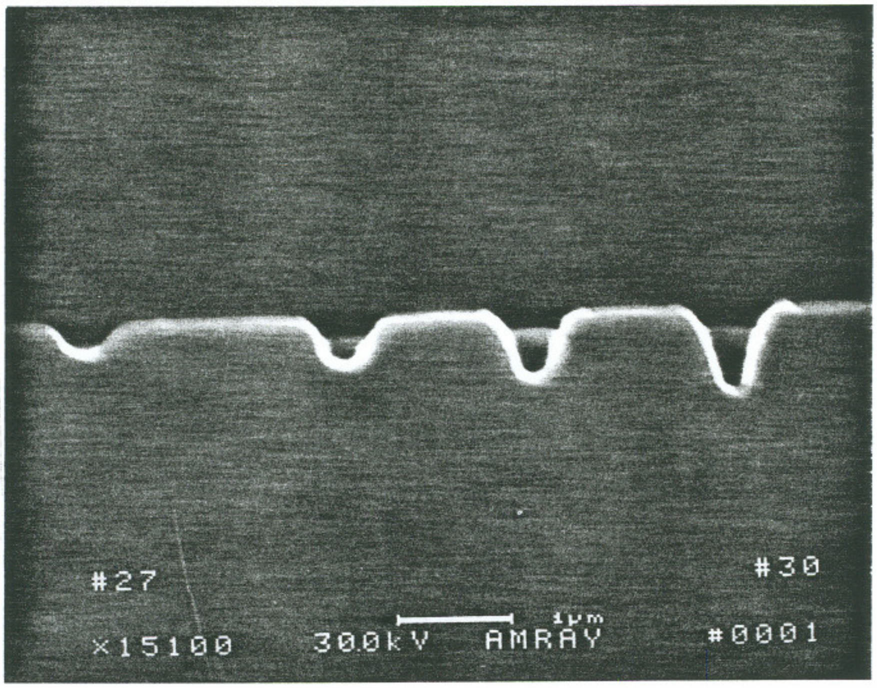

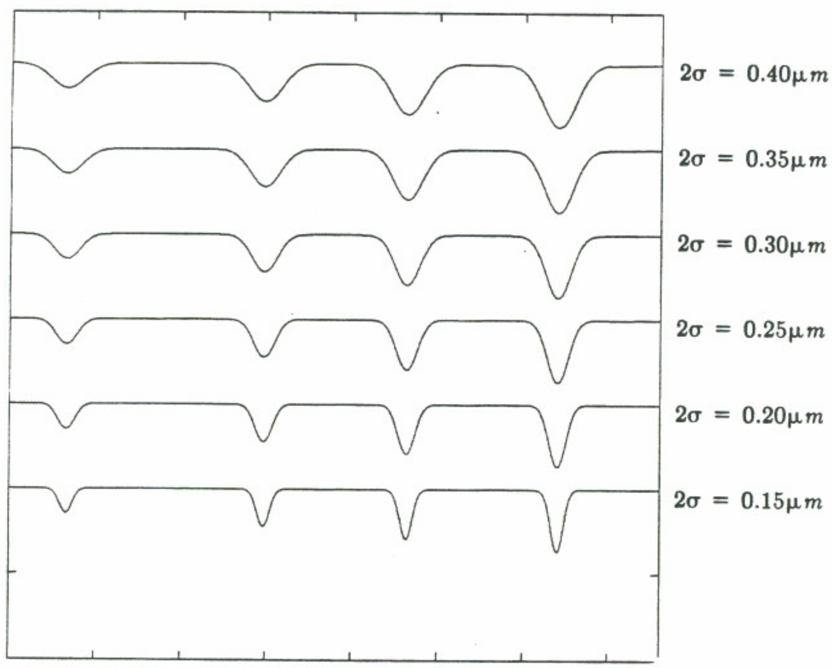

Figure 4.1 (a) Upper: SEM micrograph of cross-sections of FIB micromachined shallow grooves by single line scans on GaAs substrate. (b) Lower: a cross-sections of simulated shallow grooves by a Gaussian beam with different spot sizes. The spot size are varied from $0.15\mu m$ to $0.4\mu m$ in $0.05\mu m$ intervals for the simulated curves from bottom to top.

micromachined gratings. As far as we know, this could be the only opto-electronic application, to which the computer simulation could apply with a reasonable accuracy. The motivation of fabricating gratings is that gratings with line spacing less than $0.25\mu m$ may be valuable in DBR or DFB applications, for which first or second order DBR gratings require line spacing about $0.12\mu m$ or $0.25\mu m$, respectively. However, from FIB induced damage studies (see Appendix A for details), we have learned that the damage would destroy active regions of diode lasers underneath the machined gratings. Thus, the FIB micromachining technique would not be suitable to fabricate such gratings, because of the FIB induced damage. The FIB micromachined gratings will mainly be used to verify the computer simulation.

4.2.1.1 Gratings machined by 0.25μm ion beam

A better way to verify the Gaussian depth profile is to machine shallow gratings, rather than single line scans, for the gratings will reflect the properties of Gaussians. In other words, the depth profile of the gratings will be varied when the line spacing of the gratings and the beam spot size are changed. Therefore, by choosing the line spacings greater than two beam diameters in one scan direction (see chapter 3), and scanning the ion beam along straight lines in the other scan direction, gratings can be micromachined.

An SEM micrograph of a cross-section of a shallow grating with a $0.65\mu m = 5.2\sigma$ line spacing, micromachined by an ion beam with $0.25\mu m$

spot size on a GaAs substrate in the FIBM workstation I. is shown in Fig. 4.2(a). The ion beam current (I) was $3.1 \times 10^{-10} A$. The dwell time was 0.1 ms, and the total exposure time (T) was 1 min. 57 seconds. Therefore, the total number of Ga^+ would be $\frac{IT}{q} = 2.27 \times 10^{11}$ ions. Also the source code of the beam scan strategy will be given in Appendix B. In order to digitize the cross-section of the actual grating, a magnified (2.5×) half-tone photo copy of the SEM micrograph was traced out along the upper boundary of the high light area of the grating, using semi-transparent graph paper, so that the one micron bar in the SEM micrograph extended to about 50mm long in the graph paper. Therefore, the error (ϵ_d) of the digitization process, for digitizing each sampling point, would be around one millimeter, i.e. $\epsilon_d = \frac{1}{50} = 0.02 \mu m$. The digitized cross-section and a series of simulated cross-sections are shown in Fig. 4.2(b). The etch rate K multipled by dwell time Δt was equal to $0.0034 \mu m$/scan for the GaAs substrate. Since the dwell time $\Delta t = 0.1 ms$, K was equal to $34 \mu m$/second/scan for GaAs substrate. The simulated gratings, (starting second from the top and going to the bottom), were made by using a beam with varying diameter from $0.24 \mu m$ to $0.28 \mu m$, in $0.01 \mu m$ intervals, while scanning the Gaussian beam with the same scan strategy as in the actual FIB micromachining.

To estimate the difference between the actual grating and the simulated one, an average absolute difference (ERR) of their depths (y) over N sampling points (x_i) has been calculated as follows:

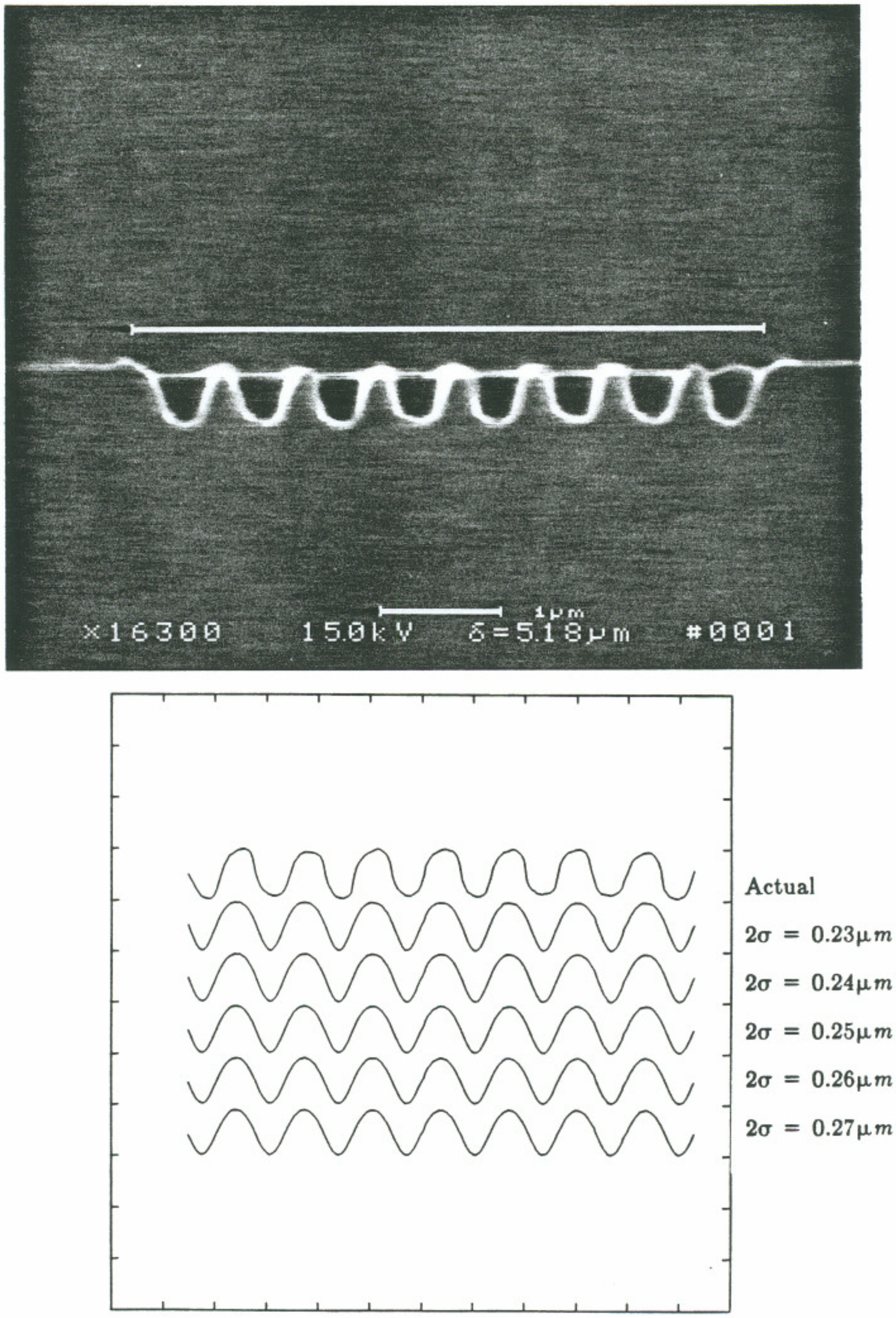

Figure 4.2 (a) Upper: SEM micrograph of a cross-section of a FIB micromachined shallow grating on GaAs substrate by straight line scans. (b) Lower: first curve (from the top) is a digitized cross-section of the actual machined grating, and cross-sections from second curve to sixth one, beginning from the top, are simulated using a Gaussian beam with a beam diameter varied from $0.23\mu m$ to $0.27\mu m$ in $0.01\mu m$ intervals.

$$ERR = \frac{1}{N}\sum_{i=1}^{N} |y_a(x_i) - y_s(x_i)|,$$

where N is the total number of the sampling points (x_i), $y_a(x_i)$ is the depth of actual digitized grating profile, and $y_s(x_i)$ is the depth of simulated one. Because errors (ϵ_d), introduced during the digitization process, would propagate through the entire digitization process over N sampling points, the uncertainties of the ERR (ΔERR) could be calculated as the following, using equations described in section 3.7 of the book: "Experimentation: An Introduction to Measurement Theory and Experiment Design". $\Delta ERR = \frac{\epsilon_d}{\sqrt{N}}$. Thus, $ERR = ERR \pm \Delta ERR$. The correlation coefficient CRL between the actual digitized grating profile and the simulated one was calculated as follows:

$$CRL = \frac{E(\mathbf{y_a y_s}) - E(\mathbf{y_a})E(\mathbf{y_s})}{\sqrt{E(\mathbf{y_a}^2) - E^2(\mathbf{y_a})}\sqrt{E(\mathbf{y_s}^2) - E^2(\mathbf{y_s})}},$$

where $E(\mathbf{x})$ is the expected value or mean of an array $\mathbf{x}$. $-1.0 \leq CRL \leq 1.0$. For zero mean functions, if $CRL = 1$, the two functions display the same functional dependence within a positive scaling factor; if $CRL = -1$, the two functions display the same functional dependence within a negative scaling factor; if $CRL = 0$, the two functions will be uncorrelated.

The computer simulation has only two intrinsic parameters, i.e. the etch rate K and the beam radius σ. The parameter K is determined by physical conditions such as the type of substrates, the beam energy, and the type of incoming ions. The beam radius σ is determined by the ion optics. To prove the consistency of this simulation, the ERR should approach to its minimum point at the calibrated 2σ value ($0.25\mu m$), and CRL should approach its maximum. Because the one micron bar extended to 40mm long, $\Delta ERR = \frac{1.0}{40.0\sqrt{197}} = 0.0018\mu m$, with $N = 197$. The ERRs for various beam diameters 2σ (BD) are given in the following table.

SIMULATION	1	2	3	4	5
ERR ($10^{-2}\mu m$)	4.0	3.8	4.0	4.3	4.7
CRL	0.95	0.96	0.96	0.96	0.96
BD (μm)	0.23	0.24	0.25	0.26	0.27

A graph of ERR with error bars vs. BD is shown in Fig. 4.3. Note that, within the given uncertainty (ΔERR), the ERRs could not be distinguished at the BD = 0.23, 0.24 and $0.25\mu m$. In other words, the actual beam diameter could be in the range of 0.23 to $0.25\mu m$, based upon the simulation. Moreover, the CRL keeps constant of 0.96 as BD increases, which indicates that the computer simulation fails to simulate the actual grating structure.

Also the actual grating has a rather sharper top and more round bottom than the simulated one. The sharper top may be caused by the large non-Gaussian tail of the actual beam current distribution, because the larger beam

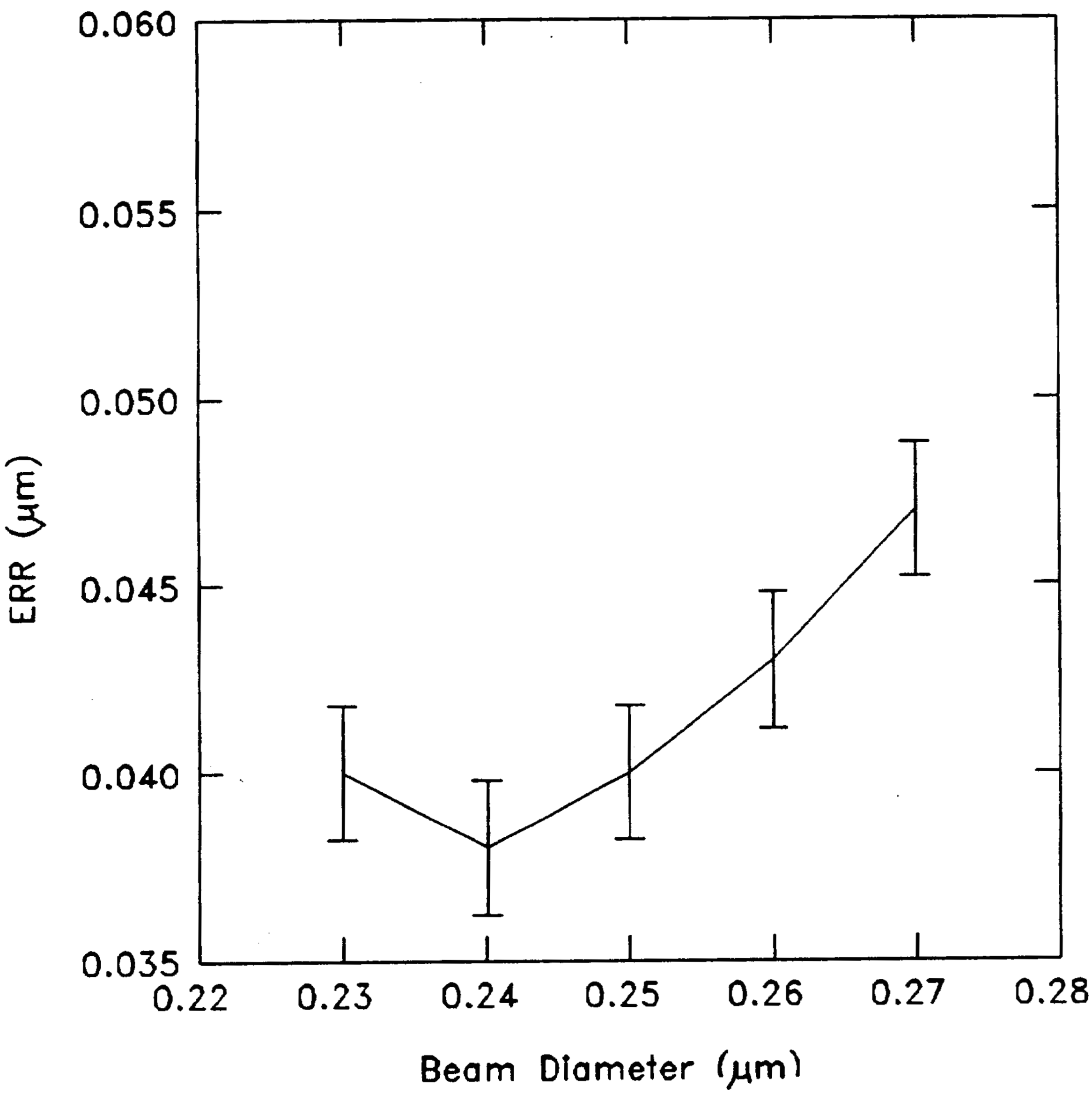

Figure 4.3 A graph of *ERR* with error bars vs. *BD*, where $\Delta ERR = 0.0018 \mu m$ in GaAs substrate.

tail would "machine" more materials around the top of the grating pitch than a Gaussian beam. The more round bottom may be caused by droplets covering the underlying materials. Systematic studies of such Ga-rich droplet production in GaAs and GaAs based materials have been done by Puretz[87] in terms of ion current effects, droplet size, droplet motion, beam heating effects, and a simple model of droplet formation onset. In general, the droplet size varies from sub-micron to several microns. Puretz[87] found that the threshold dose for droplet formation, with a Ga^+ ion beam of 25 keV energy and at room temperature, was about $2.5\times10^{16}/\mathrm{cm}^2$. However, due to periodic (non-uniform) distribution of ion dosage, the average ion dose could not be obtained by the definition described in page 113 of Puretz's dissertation: "The dose, $D = \frac{Jt}{q}$, with J the average current density, q the ion charge and t the exposure time". Nevertheless, the threshold was greatly exceeded along the grating grooves and, as can be seen in the SEM micrograph of Fig. 4.4(a), droplets have formed on the grating grooves where the cross-section was produced as shown in the SEM micrograph of Fig. 4.4(b). Droplets were not recognizable on the cross-section, but are visible in a top view. The total ion dose per grating groove of this grating is the same as in the previous grating (Fig. 4.2). Note the distance (DST) between the wafer surface to the top of grating is approximately zero. For these simulated gratings, the DST increases as the spot size increases.

The SEM micrograph of a cross-section of a micromachined grating fabricated with the same ion dose as in the previous case but with a different scan strategy (i.e. with line spacing of $0.57\mu m = 4.56\sigma$) is shown in Fig.

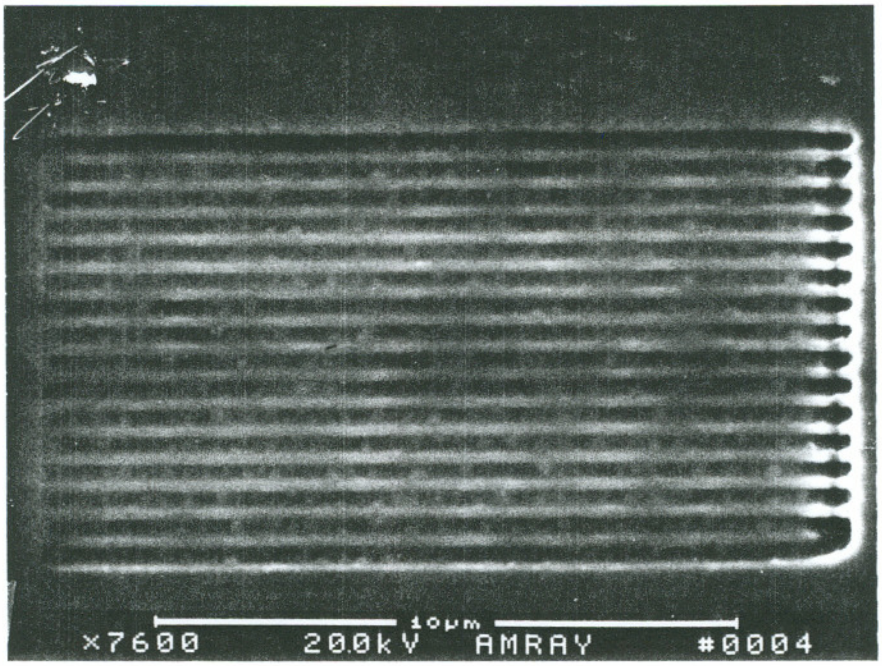

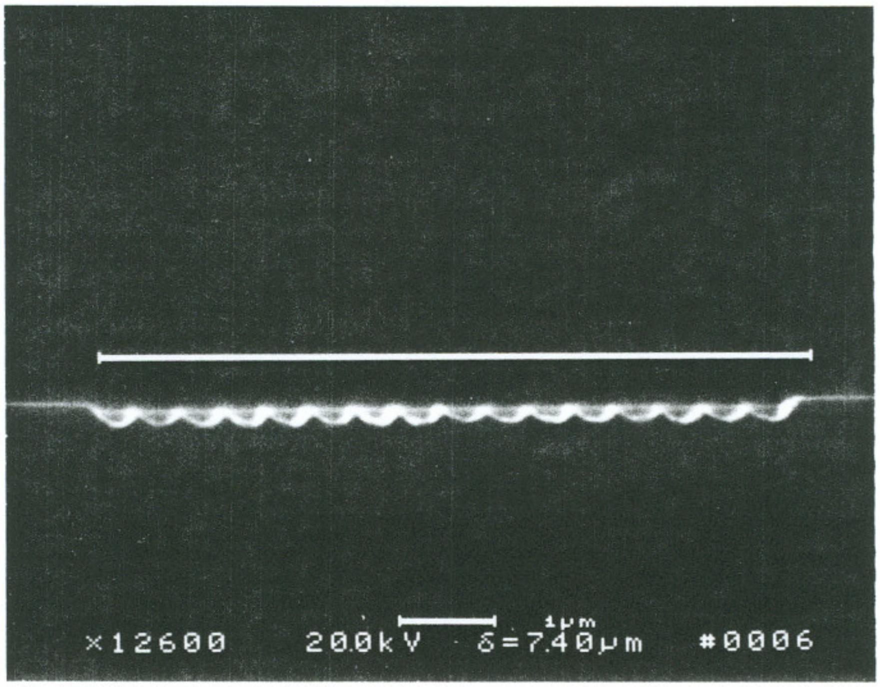

Figure 4.4 (a) Upper: SEM micrograph of a top view of a micromachined grating on GaAs substrate. Droplets have formed on the grating grooves. (b) Lower: SEM micrograph of a cross-section of the grating.

4.5(a). The average DST's of the micromachined grating is $0.22\mu m$. In Fig. 4.5(b), cross-sections of a digitized actual grating (top curve) and a series of simulated gratings are plotted. The simulated beam diameters are varied from $0.23\mu m$ to $0.27\mu m$ in $0.01\mu m$ intervals, beginning at the top. The DST's, differences of DST between micromachined and simulated gratings ($DIFF$), and beam diameters (BD) are given in the following table.

SIMULATION	1	2	3	4	5
DST (μm)	0.15	0.18	0.21	0.24	0.27
DIFF. (μm)	0.07	0.04	0.01	-0.02	-0.05
BD (μm)	0.23	0.24	0.25	0.26	0.27

The minimum DIFF occurs at the beam diameter of $0.25\mu m$.

Using a digitized grating profile, we have also calculated ERR and CRL of this grating as shown in the following table, while $\Delta ERR = \dfrac{1.0}{51.0\sqrt{181}} = 0.0015\mu m$, because the one micron bar extended to 40mm long, with $N = 181$.

SIMULATION	1	2	3	4	5
ERR ($10^{-2}\mu m$)	5.4	4.5	3.9	3.7	4.2
CRL	0.96	0.96	0.96	0.96	0.96
BD (μm)	0.23	0.24	0.25	0.26	0.27

A graph of ERR with error bars vs. BD is shown in Fig. 4.6. Note that,

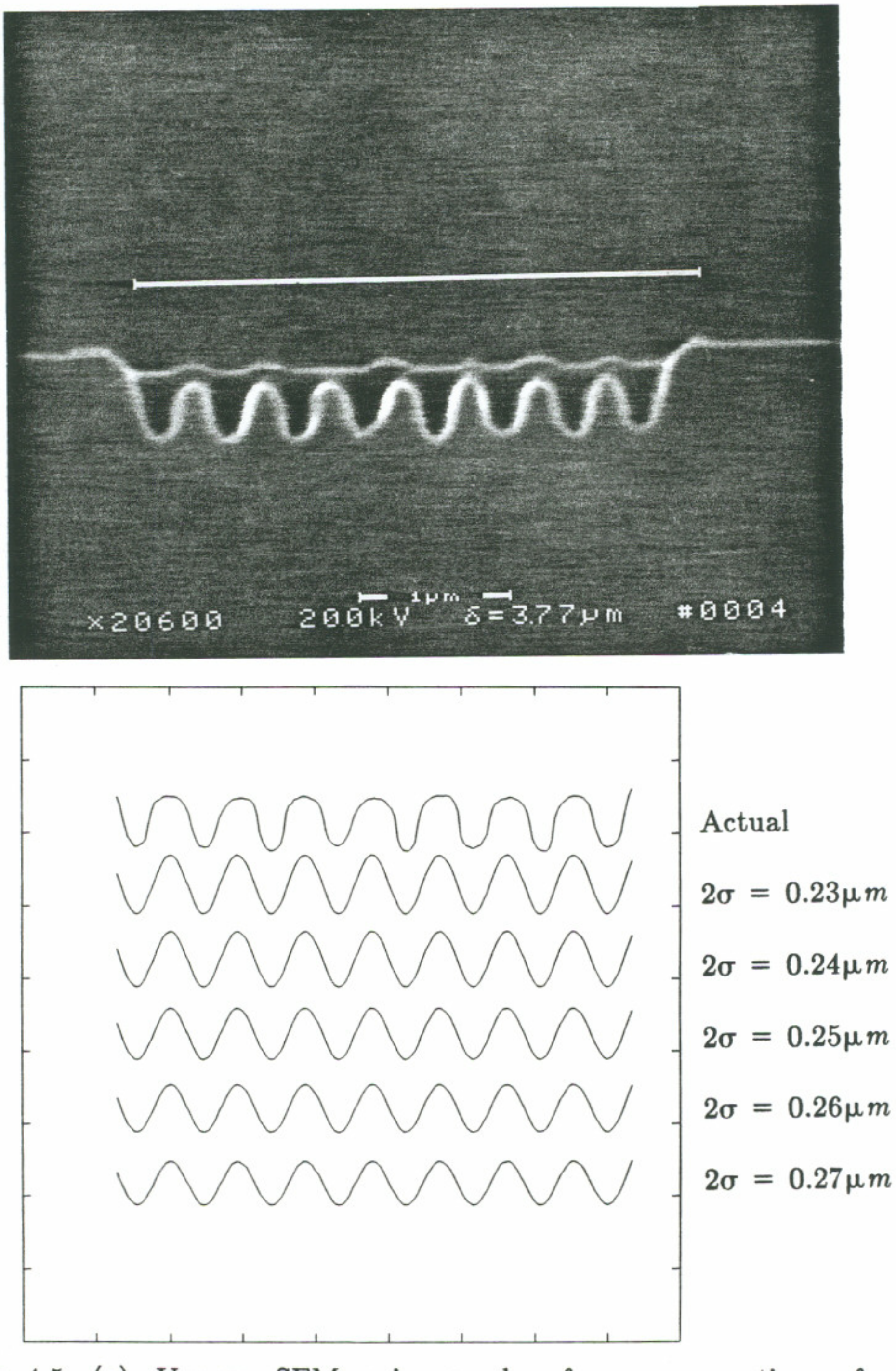

Figure 4.5 (a) Upper: SEM micrograph of a cross-section of a FIB micromachined shallow grating on GaAs substrate by straight line scans. (b) Lower: first curve (from the top) is a digitized cross-section of the actual machined grating, and cross-sections from second curve to sixth one, beginning at the top, are simulated using a Gaussian beam with a beam diameter varied from $0.23\mu m$ to $0.27\mu m$ in $0.01\mu m$ intervals.

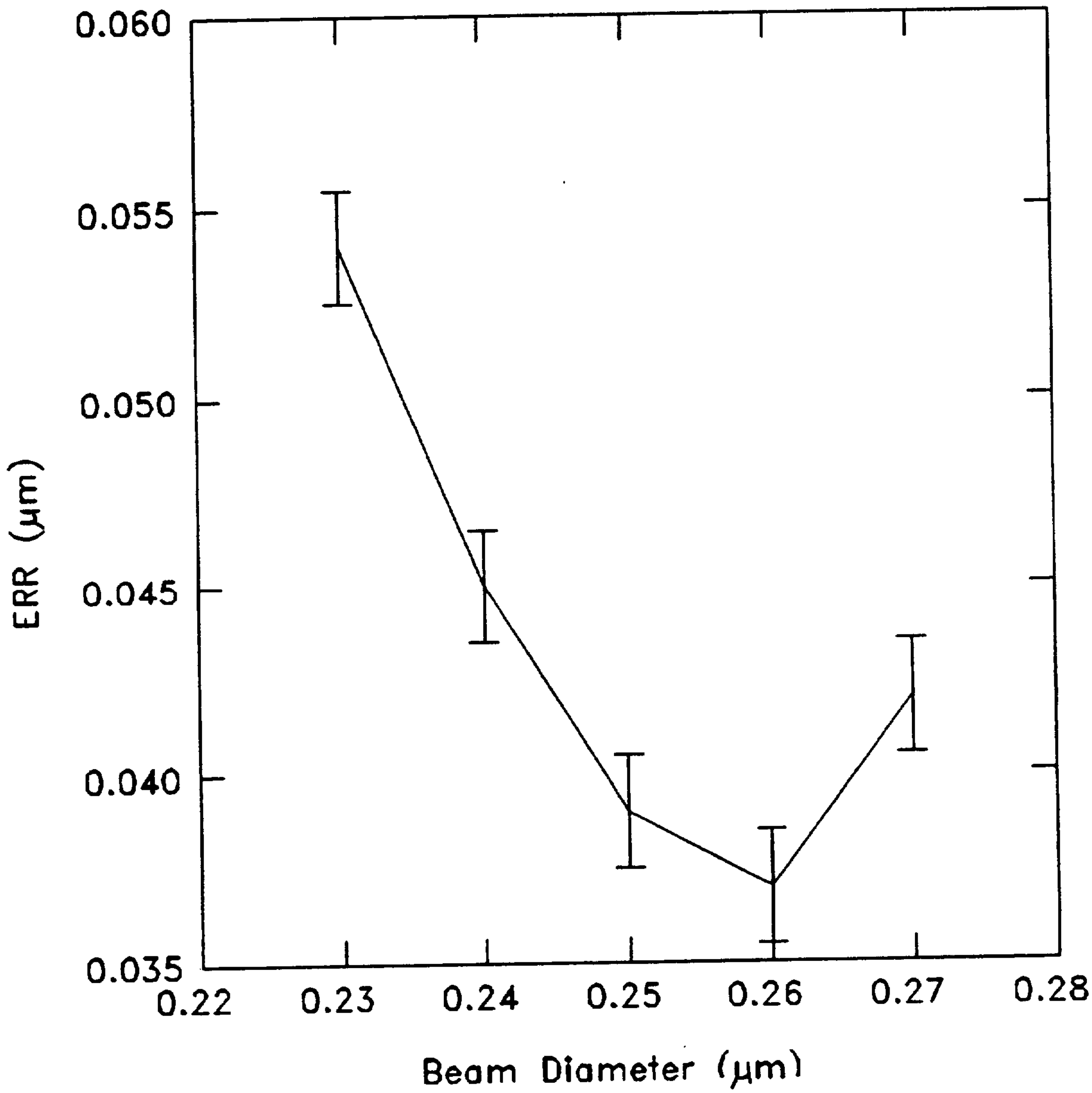

Figure 4.6 A graph of ERR with error bars vs. BD, where $\Delta ERR = 0.0015 \mu m$ in GaAs substrate.

within the given uncertainty (ΔERR), the ERRs could be marginally distinguished at the BD = 0.25 and 0.26μm. For the above-mentioned grating, the minimum points of the ERR have been reached at $2\sigma = 0.25$ and 0.26μm. Therefore, the simulation and the formation of Ga droplet has to be further investigated in order to improve the accuracy of the computer simulation. Also the CRL keeps constant of 0.96 as the BD increases.

By calculating the ERR or CRL as a function of σ, a quantitative measure of the computer simulation is given to show how sensitive the only adjustable parameter σ is. If the actual beam diameter was used in the simulation, the simulated structures would be very close to the real ones. Note that the only difference between the two gratings (used for simulation) was the scan strategy. The minimum point of the ERR, in both cases, occurs around $2\sigma = 0.25\mu m$, which argues for the consistency of the simulation, although the CRL did not show this consistency, which could be due to the formation of Ga droplets on GaAs substrates. Therefore, different substrate (Si) will be used in the fabrication of shallow gratings, due to the fact that Ga droplets would form at a larger threshold ion dose[88] of 7×10^{16}ions/cm^2, in Si substrate using a 10-keV Ga^+ focused ion beam, than in GaAs substrate. However, the beam energy, used in our experiment, was 25-keV, a lower threshold ion dose (in Si) would be expected[87].

In conclusion, the computer was calibrated by using the FIB micromachined shallow grooves, as shown in Fig. 4.1. First, the etch rate K was determined by matching the depth of the machined grooves and the simulated ones. Second, the beam diameter (2σ) of the Gaussian beam was obtained by finding the closest match between the simulated grooves and the actual ones, among various grooves simulated with different beam diameters and constant etch rate K. More complicated structures such as gratings have then been simulated by applying the same scan strategy as that used to micromachine the real structures, but keeping the intrinsic parameters such as σ and K constant. However, due to the secondary effects, most likely the formation of Ga droplets, the simulated structures are not exactly the same as the actual ones. The accuracy of the computer is measured by the *ERR*, i.e. the average absolute difference between the actual grating and the simulated one. There are cases, to be shown in section 4.2.2, where the simulation fails to predict micromachined structures due to secondary effects.

The question may arise whether non-Gaussian functions could also be used to simulate the FIBM structures. Two bell-shaped functions have been introduced in order to investigate the sensitivity of the basic function for the simulation. One is the Cauchy function $\frac{1}{1 + x^2/a^2}$, where $2a$ is the full width at half maximum, the other is the half sine function $\sin(\pi \frac{x}{b})$. The simulated cross-sections of the micromachined grating (shown in Fig. 4.2(a)) have been shown in Fig. 4.7. The Cauchy function is used in Fig. 4.7(a), with a varied from 0.1 to 0.14μm in 0.01μm intervals, where a is in a similar region as σ of Gaussian. The a was chosen, so that *ERR* would pass through its minimal point. The *ERR* and *CRL* were calculated as given in the following table.

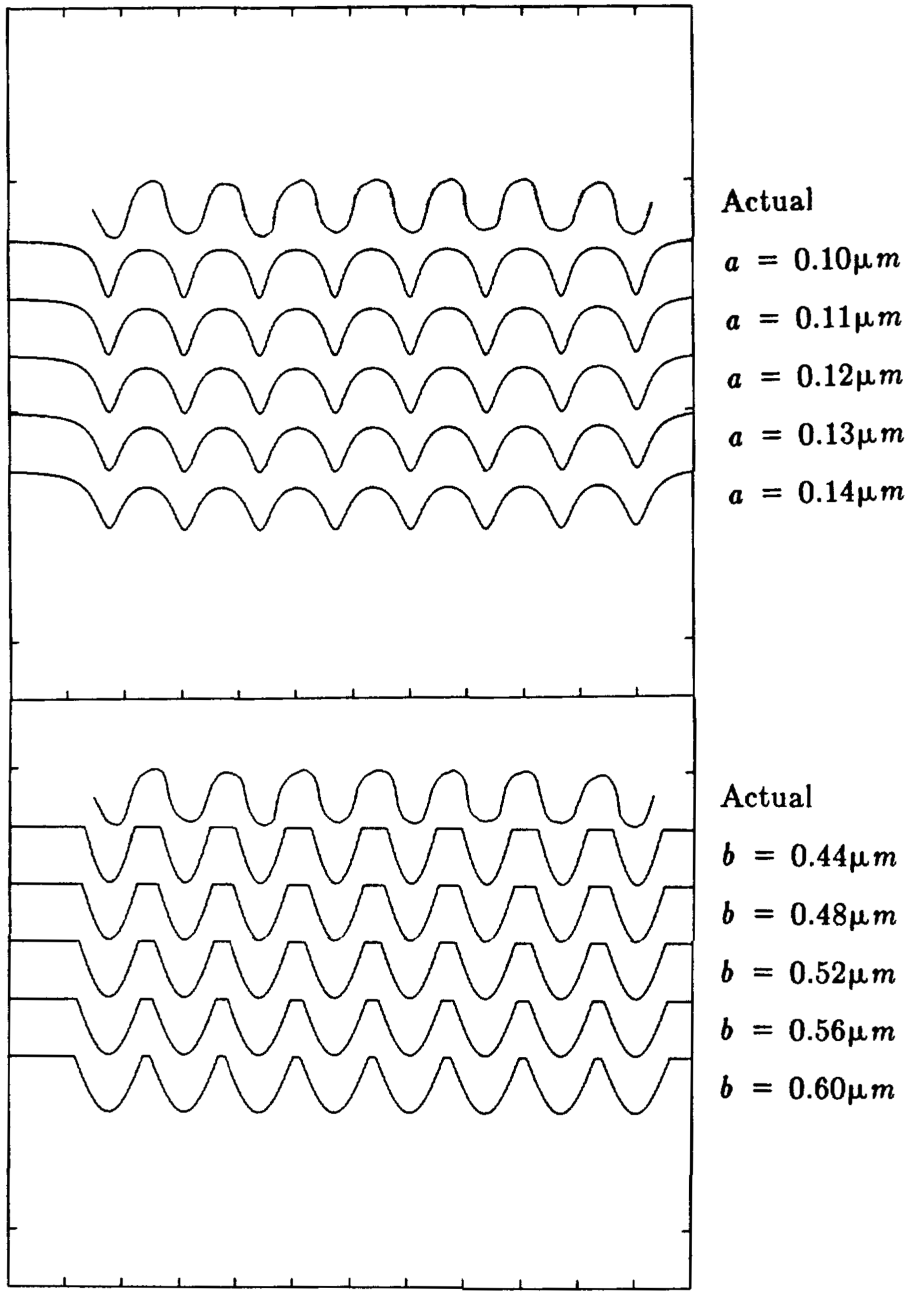

Figure 4.7 (a) Upper: first curve (from the top) is a digitized cross-section of the actual machined grating, and cross-sections from second curve to sixth one, beginning at the top, are simulated using a Cauchy beam $(1/(1 + x^2/a^2))$ with a varied from $0.1\mu m$ to $0.14\mu m$ in $0.01\mu m$ intervals. (b) Lower: first curve (from the top) is the digitized cross-section, and cross-sections from second curve to sixth one, are simulated using a half sine beam $(\sin(\pi\, x/b))$ with b varied from $0.44\mu m$ to $0.60\mu m$ in $0.04\mu m$ intervals.

SIMULATION	1	2	3	4	5
ERR ($10^{-2}\mu m$)	7.4	7.3	7.6	8.2	9.3
CRL	0.88	0.89	0.90	0.92	0.92
a (μm)	0.10	0.11	0.12	0.13	0.14

The half sin function is used in Fig. 4.7(b), with b varied from 0.44 to 0.60μm in 0.04μm intervals. The *ERR* and *CRL* were also calculated.

SIMULATION	1	2	3	4	5
ERR ($10^{-2}\mu m$)	4.0	3.9	4.2	5.0	6.1
CRL	0.96	0.96	0.96	0.95	0.94
b (μm)	0.44	0.48	0.52	0.56	0.60

The minimal *ERR* is 0.038, 0.073 and 0.039μm using Gaussian, Cauchy and half sine, respectively, while the maximal *CRL* is 0.96, 0.92 and 0.96. However, for the Cauchy function, the *ERR* and *CRL* did not show any consistency. For the half sine function, although, the value of *ERR* or *CRL* was close to that of Gaussian, the simulated curves are unrealistically flat at the top of the grating grooves. As comparison, the digitized cross-section is plotted in both figures. The simulated cross-sections do not look similar, while this does not prove that the beam has a Gaussian current distribution, it could be concluded that the Gaussian current distribution was the best approach among these three basic functions.

It may be of interest to generate a basic function which will yield better simulation results than Gaussian.

4.2.1.2 Gratings machined by $0.05\mu m$ ion beam

If we used a focused ion beam with 500Å spot size, the minimal achievable line spacing of FIB micromachined gratings would be expected to be $0.1\mu m$. Although, the FEI prototype FIBM workstation is capable of producing an ion beam with a 500Å spot size, considerable experience is required to achieve the optimum focusing condition of the system. In fact smallest achievable grating in this study has a line spacing of $0.18\mu m$, as shown in a top view in an SEM micrograph of Fig. 4.8. The line spacing of $0.18\mu m$ was determined by measuring the distance of 20 grating pitches divided by 19. A grating with line spacing of $0.23\mu m$ was also produced, as shown in the SEM micrograph of Fig. 4.9. In Fig. 4.9(a), small droplets[84,87] appear on the grating surface. When the grating is rinsed in a dilute solution of HCl, the Ga droplets vanish, as shown in Fig. 4.9(b).

A cross-section of a cleaved FIB micromachined grating, with line spacing of $0.4\mu m$, is shown in the SEM micrograph of Fig. 4.10(a). As a comparison, three simulated grating cross-sections are shown in Fig. 4.10(b). From the bottom to the top, three cross-sections were simulated using a Gaussian beam with beam diameters of 0.1, 0.15 and $0.2\mu m$, respectively. Apparently, the bottom one is much too sharp, and the top one is too round. Thus, the actual beam diameter was between 0.1 to $0.2\mu m$, rather than the $0.05\mu m$ achievable beam diameter. This implies the value σ should not be

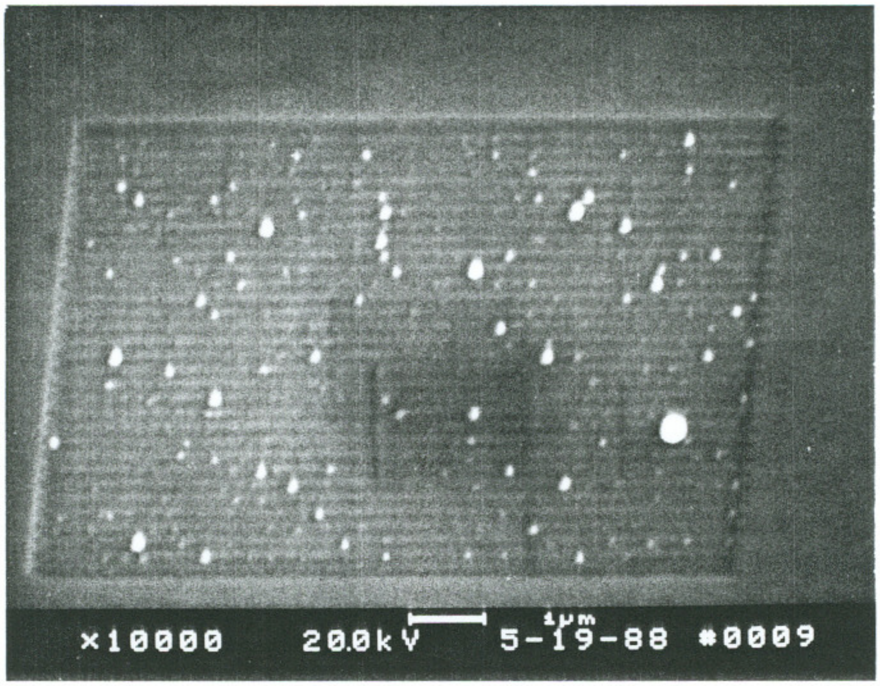

Figure 4.8 SEM micrograph of a grating FIB micromachined on GaAs substrate, using an FEI two-lens ion gun with minimum achievable 500Å spot size, has a line spacing of $0.18 \mu m$.

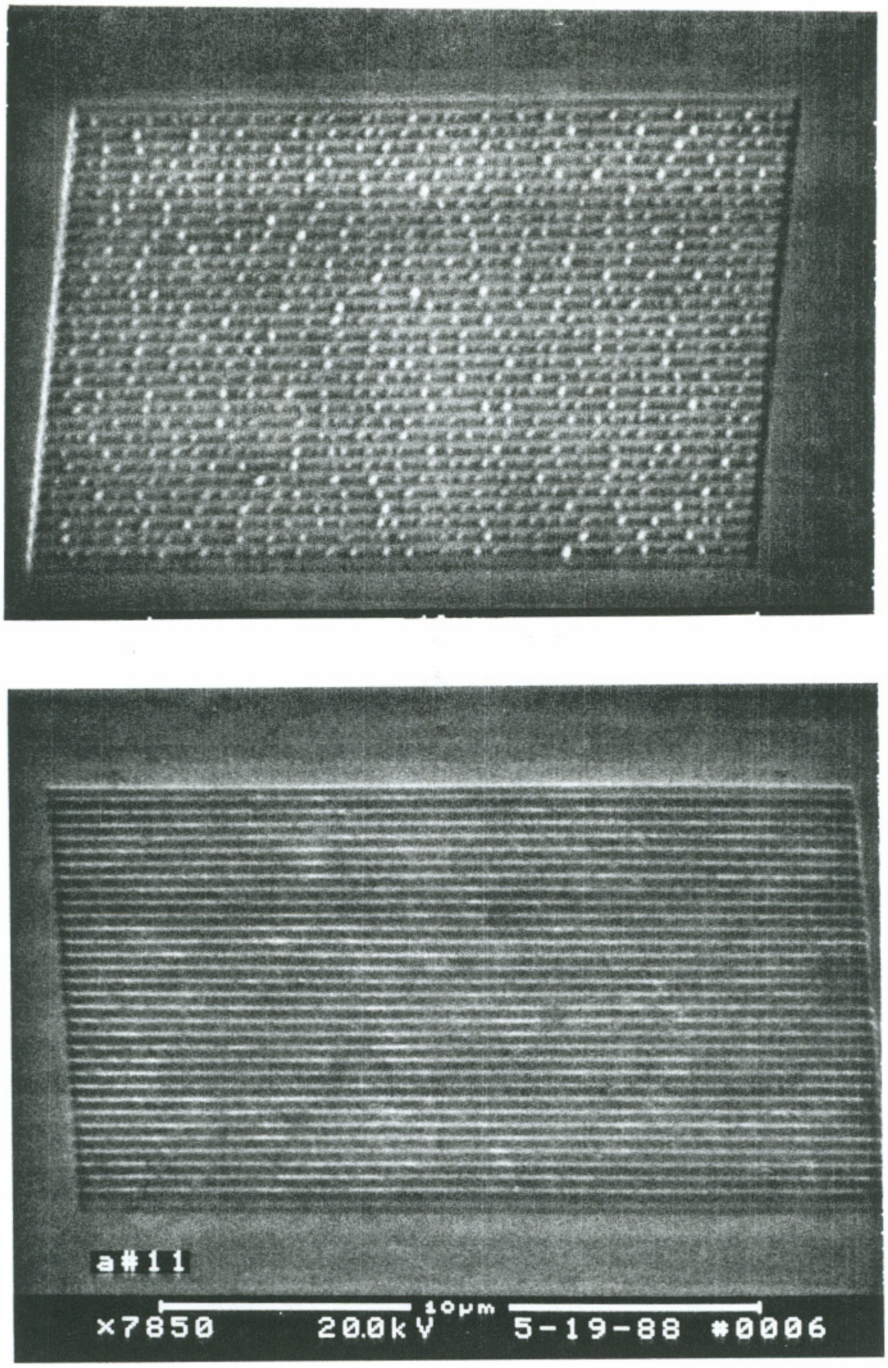

Figure 4.9 (a) Upper: SEM micrograph of a FIB micromachined grating with line spacing of $0.23\mu m$ on GaAs substrate, where many small droplets appear on the grating surface. (b) Lower: SEM micrograph of the same grating as in (a), being rinsed in a dilute solution of HCl, where the Ga droplets vanished.

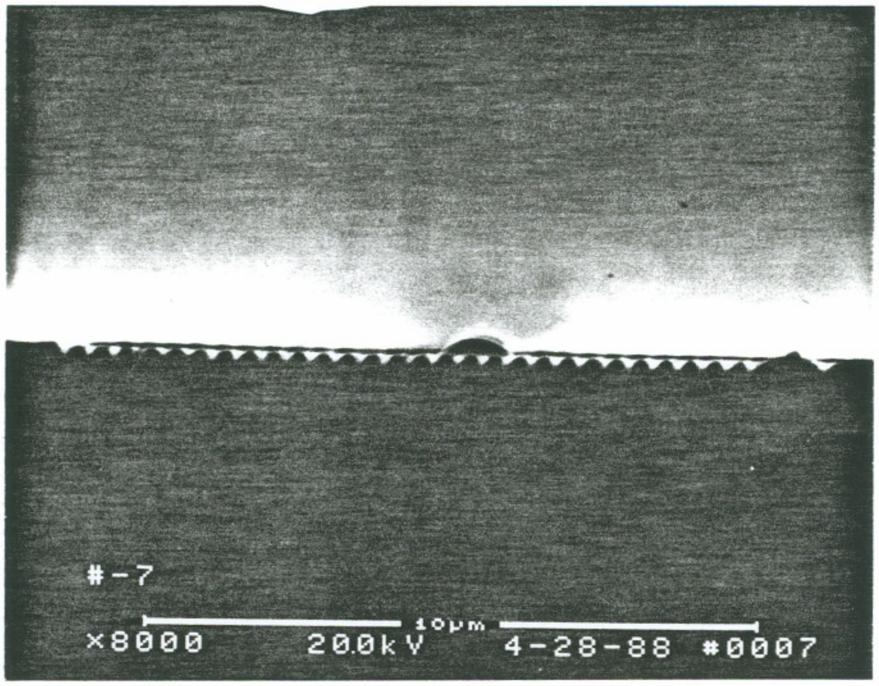

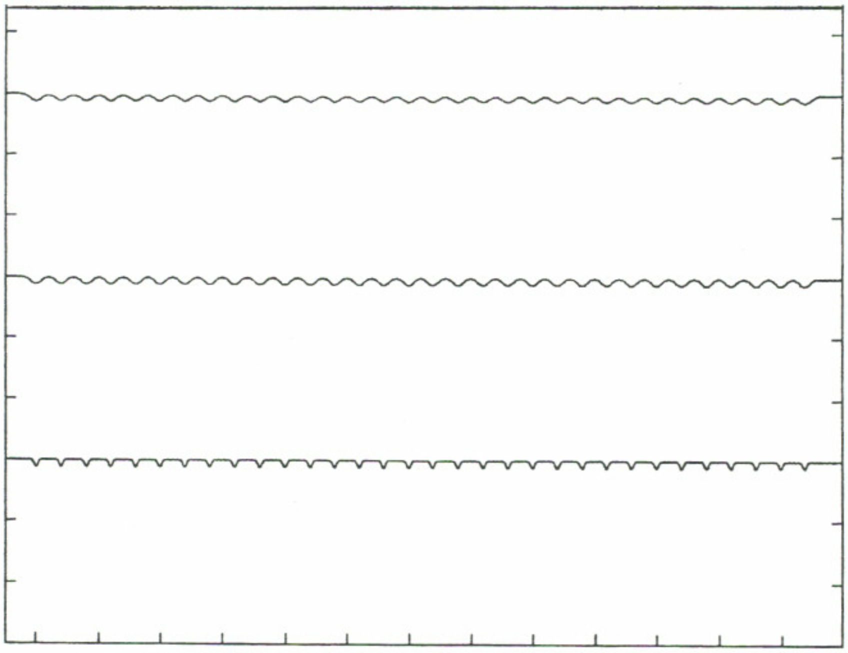

Figure 4.10 (a) Upper: SEM micrograph of a cross-section of a cleaved FIB micromachined grating with line spacing of $0.23\mu m$ on GaAs substrate. (b) Lower: a graph of three simulated cross-sections (from the bottom to the top) using a Gaussian beam with a beam diameter of 0.1, 0.15 and $0.2\mu m$, respectively.

the manufacturer's suggested value of $0.05\mu m$, because considerable experience is required to achieve the optimum focusing condition ($0.05\mu m$ spot size) of the FIBM system.

4.2.1.3 Gratings FIB micromachined on Si substrate

As is known, droplets form randomly on the surface of a GaAs substrate bombarded with a Ga ion beam and will prevent the underlying material from sputtering off the surface. Because the present computer simulation doesn't take into account secondary effects such as redeposition or droplet formation, a Si substrate was used as an experimental verification of the simulation, due to the fact that the formation of droplets would be reduced on Si substrate. This experiment has been conducted in the FIBM workstation III. No droplet formation could be recognized in the SEM micrograph of Fig. 4.11(a), which is a top view of a micromachined grating used for simulation, to be described later. In a SEM micrograph of Fig. 4.11(b), no droplets were visible even in grating grooves micromachined with a total ion dose 1.5 times higher than the grating in Fig. 4.11(a).

A cross-section of the grating FIB micromachined on a Si wafer is shown in the SEM micrograph of Fig. 4.12(a). A digitized cross-section and a series of simulated cross-sections are shown in Fig. 4.12(b). The etch rate K multipled by the dwell time Δt was equal to $0.0021\mu m$/second/scan. Since the dwell time $\Delta t = 0.1ms$, K was equal to $21\mu m$/second/scan for Si substrate. The beam diameters used for the simulated curves (from the top to the

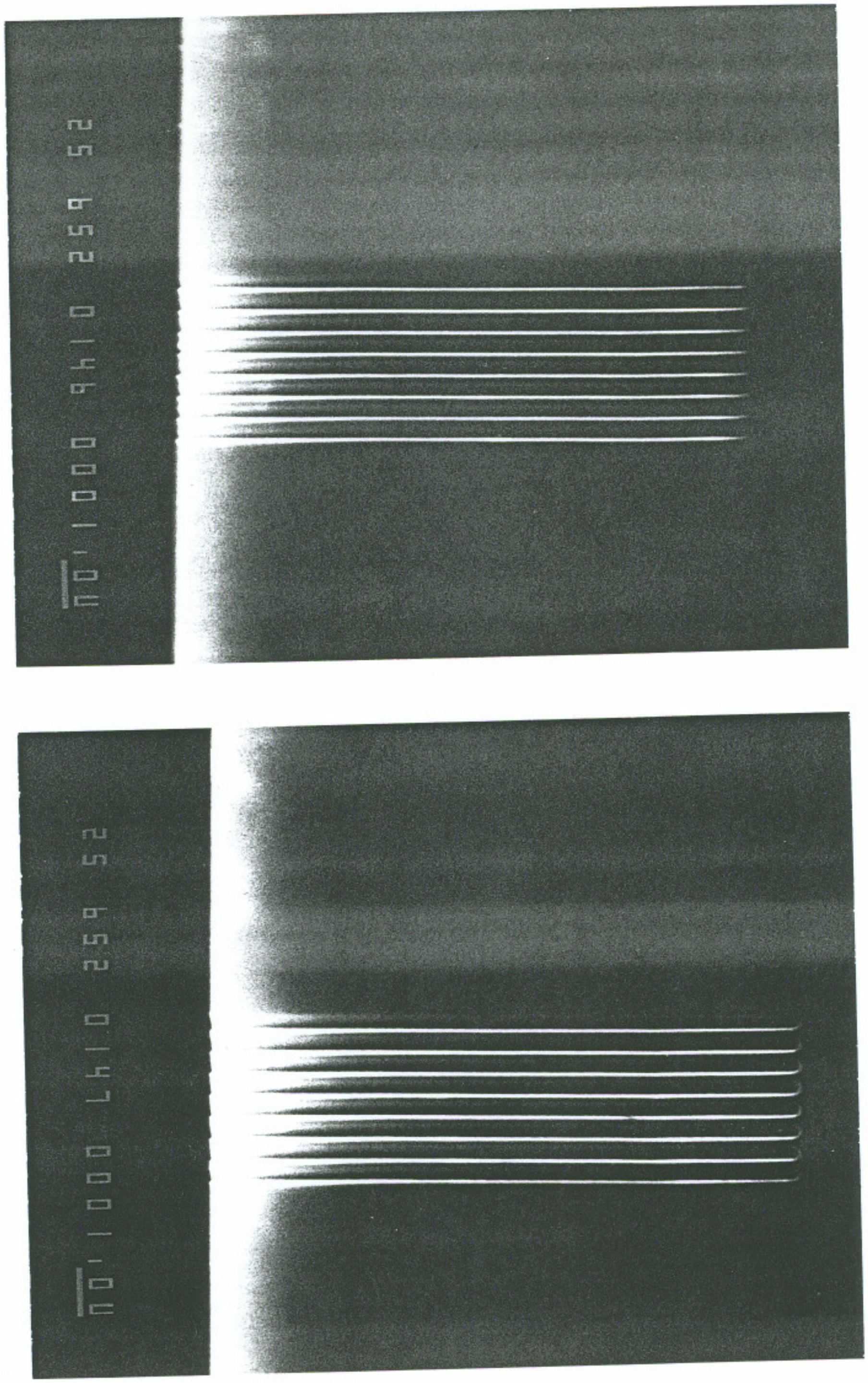

4.11 (a) Upper: SEM micrograph of a top view of a micromachined grating on Si substrate. (b) Lower: SEM micrograph of a top view of another micromachined grating on Si substrate, with a total ion dose 1.5 times higher than the previous one. No droplet formation could be recognized.

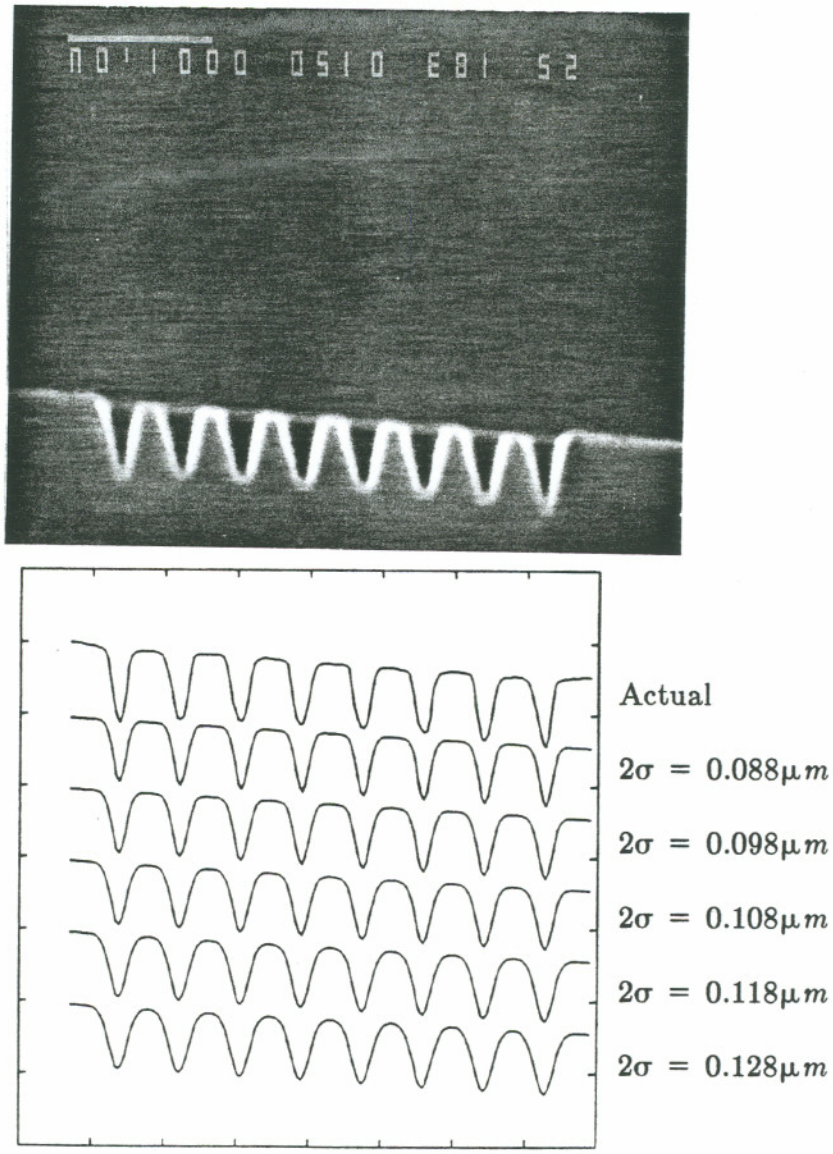

Figure 4.12 (a) Upper: SEM micrograph of a cross-section of a cleaved FIB micromachined grating on Si substrate. (b) Lower: first curve (from the top) is a digitized cross-section of the actual machined grating, and cross-sections from second curve to sixth one, beginning at the top, are simulated using a Gaussian beam with a beam diameter varied from $0.088\mu m$ to $0.128\mu m$ in $0.01\mu m$ intervals.

bottom) are varied from $0.098\mu m$ to $0.138\mu m$ in $0.01\mu m$ intervals. The ERR and CRL have also been calculated for comparison of gratings machined on GaAs substrates, as described in section 4.2.1.1. $\Delta ERR = \frac{1.0}{47.5\sqrt{172}} = 0.0016\mu m$, because the one micron bar extended to 47.5mm long, with $N = 172$.

SIMULATION	1	2	3	4	5
ERR ($10^{-2}\mu m$)	3.6	3.0	2.9	3.2	3.7
CRL	0.98	0.98	0.98	0.97	0.97
BD (μm)	0.088	0.098	0.108	0.118	0.128

A graph of ERR with error bars vs. BD is shown in Fig. 4.13. Note that, within the given uncertainty (ΔERR), the ERRs could not be distinguished at the $BD = 0.098$ and $0.108\mu m$. In other words, the minimum points of the ERR have been reached at $2\sigma = 0.098$ and $0.108\mu m$. Clearly, a better way of digitizing the actual micromachined structure is important for quantifying the accuracy of the computer simulation. Nevertheless, the minimal ERR ($2.9 \times 10^{-2}\mu m$) of this grating is smaller than that of the gratings machined on GaAs substrates. The maximal CRL (0.98) is larger, as well. It thus seems that the formation of droplets is the primary difficulty for simulating shallow gratings on GaAs substrates, while other secondary effect would be minimal in the case of low depth aspect ratio.

Note that the grating has been machined on a 3° tilted Si wafer, due to misalignment of the Si wafer. Thus, modification has been made in Eqn. 2.3,

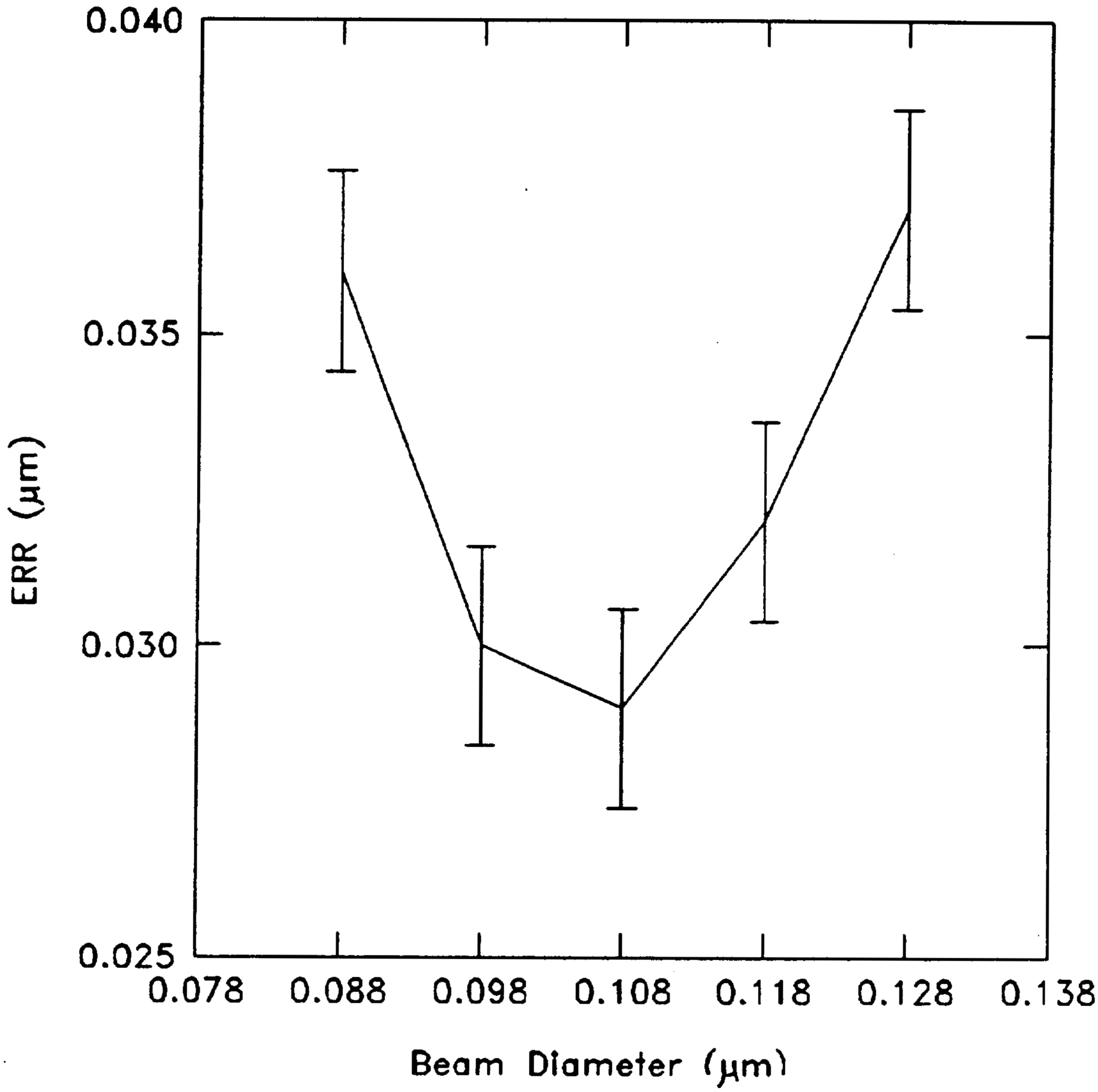

Figure 4.13 A graph of *ERR* with error bars vs. *BD*, where $\Delta ERR = 0.0016 \mu m$ in Si substrate.

which is used for the single scan approach.

$$Z_{n+1}(x,y) = Z_0(x,y) + Z_n(x,y) + \tag{4.1}$$

$$\sum_{x_p,y_p} \frac{K}{2\pi} \exp\left(-\frac{(x-x_p)^2+(y-y_p)^2}{2\sigma^2}\right) \omega(x_p,y_p)\, dt,$$

where $Z_0(x,y)$ is the initial surface contour, and the incident ion beam is still along z axis. In the case of performing FIB micromachining on a tilted substrate, $Z_0(x,y)$ would be a slanted plane, rather than a flat plane of $Z_0(x,y) = 0$. Without taking into account sputtering yield angular dependency, the simulation result is still better than the one on GaAs substrates.

4.2.2 Cases badly predicted by the computer simulation

A structure with a 45° slanted bottom, cutting into a diode laser waveguide, may be useful in surface-emitting diode laser applications, (see the paper entitled "300 mW operation of a surface-emitting phase-locked array of diode lasers" by Puretz *et. al.*)[38]. The fabrication of such structures has also been investigated by Crow *et. al.*[41] The possibility of simulating such structures by using this computer simulation has been studied. However, because secondary effects were neglected, the simulation results were not very satisfactory.

As shown in the SEM micrograph of Fig. 4.14(a), a cross-section of a structure with a slanted surface on a GaAs substrate was micromachined by a

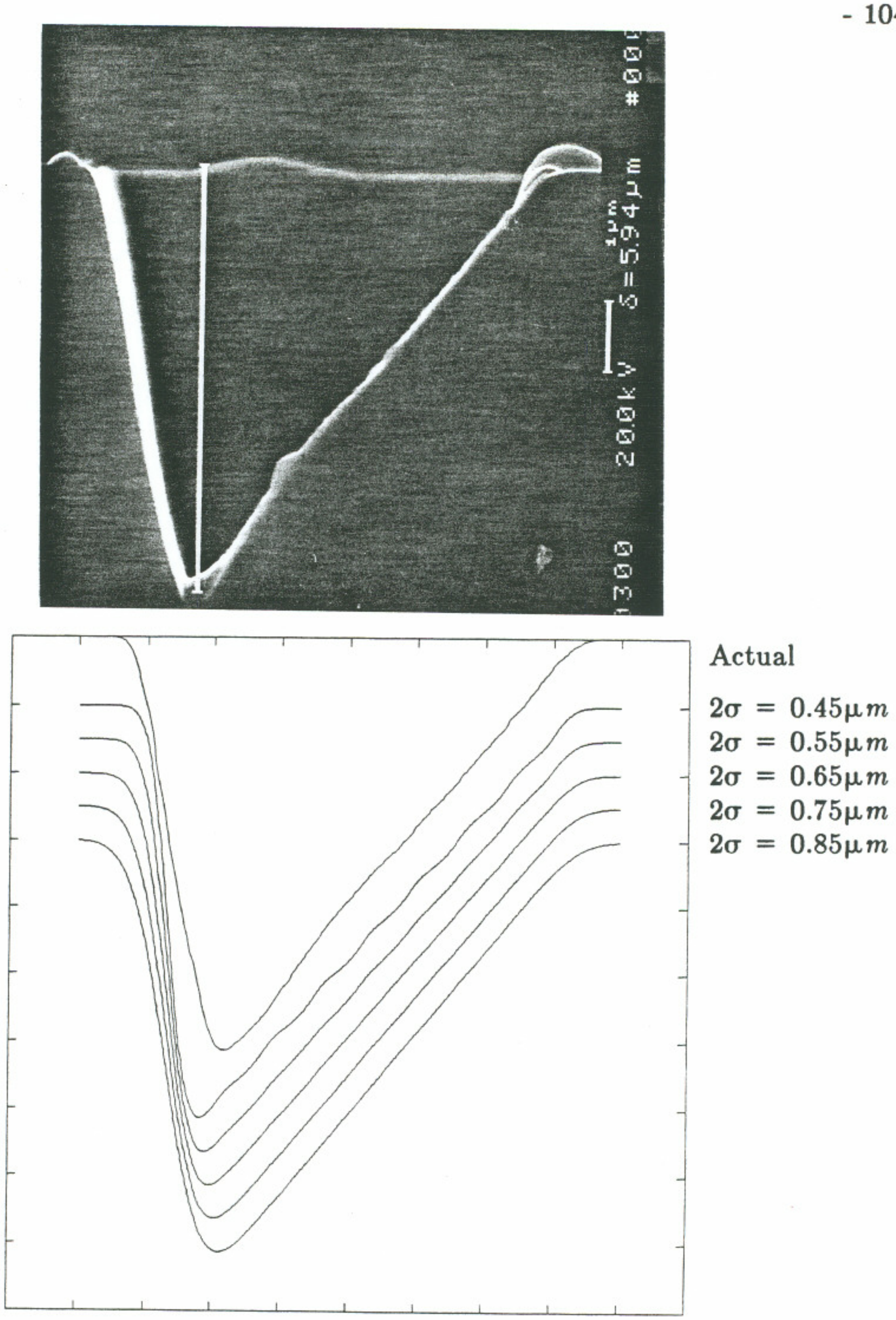

Figure 4.14 (a) Upper: SEM micrograph of a cross-section of a FIB micromachined structure with a slanted surface by straight line scans on GaAs substrate. (b) Lower: first curve (from the top) is a digitized cross-section of the actual machined structure, and cross-sections from second curve to sixth one, beginning at the top, are simulated using a Gaussian beam with a beam diameter varied from $0.45\mu m$ to $0.85\mu m$ in $0.1\mu m$ intervals.

15 kV Ga^+ ion beam focused to a spot ~$0.5\mu m$ in diameter, in the FIBM workstation I. Note that a big droplet was formed at the upper right corner of the structure. In Fig. 4.14(b), a digitized cross-sectional profile (first curve) and several simulated profiles are shown, where 2σ varies from $0.45\mu m$ to $0.85\mu m$ in intervals of $0.1\mu m$ (from the top to the bottom in the associated profile). The *ERR*s and *BD*s are given in the following table.

SIMULATION	1	2	3	4	5
ERR (μm)	0.23	0.15	0.12	0.13	0.17
BD (μm)	0.45	0.55	0.65	0.75	0.85

The minimum point of the *ERR* is at $2\sigma = 0.65\mu m$. Note that the bottoms of the simulated profiles move from the left side of the bottom of the actual structure to the right side, but they do not simulate the actual structure as closely as in the shallow grating cases. These differences may be caused by secondary effects, mainly the ion beam reflection effect, due to the fact that the bottom of the actual structure was farther right than that of the simulated one, because the ion beam was probably reflected to the right, when it reached the left side wall. Also when the beam diameter increases, the near-vertical slope (left side of the crater) increases. The slope angle of the actual slanted surface is 50.11°. The slope angles of the simulated structures, the difference of angles between machined and simulated surfaces, and the beam diameters are given in the following table.

SIMULATION	1	2	3	4	5
ANGLE (°)	47.0	49.0	50.0	50.0	51.0
DIFF. (°)	2.8	0.8	-0.1	-0.3	-0.9
BD (μm)	0.45	0.55	0.65	0.75	0.85

The minimum difference in the slope angles occurs at a beam diameter of $0.65\mu m$.

4.3 Turning mirrors micromachined by 3-D digital scan

Recently, there has been great interest in surface emitting semiconductor diode lasers for various applications such as coherent monolithic 2-D arrays and optical interconnects for integrated optics. Unlike conventional (edge-emitting) cleaved semiconductor diode lasers, surface-emitting lasers offer advantages in wafer processing and testing. There are several approaches to achieve surface-emitting laser arrays, such as incorporation of 45° deflecting mirrors[38], parabolic deflecting mirrors[35], vertical cavities[89], and second-order distributed-Bragg-reflection (DBR) gratings[90]. Among these surface-emitting laser devices, those with DBR gratings are promising for coherent 2-D arrays with narrow beam divergences. The DBR-GSE lasers made at David Sarnoff Research Center (DSRC) have achieved large scale 2-D coherent arrays, with demonstrated beam divergences to the order of 0.01° in one direction[90].

For a DSRC DBR-GSE laser array, lateral coherence is achieved by evanescent or Y-coupling of ten or more laser stripes in the lateral direction. The array is injection coupled through DBR waveguides in the longitudinal direction by the zeroth diffracted order and undiffracted light. For convenience, this array is named as a quasi-two-dimensional (Q2D) array. Fabrication of all turning mirrors has been accomplished in the FIBM workstation II.

4.3.1 45° Turning Mirrors

To achieve laterally coherent 2-D laser arrays, a scheme to couple individual Q2D array column is needed. One such scheme is to form 45° total internal reflection (TIR) turning mirrors with which the light from one column may be reflected laterally to the next column to achieve lateral coherence[39,40] (see Fig. 4.15).

The micromachining of 45° turning mirrors was accomplished by using a 25 keV Ga^+ ion beam of $2.9 \times 10^{-10} A$ current focused into a $0.25 \mu m$ diameter spot. The incident beam was aligned normal to the wafer surface and the micromachining was carried out by scanning the beam along a line inclined at 45° to each of the laser column axes at one end of the columns. The scan strategy was to keep constant $\frac{ds}{dt}$, while the scan speeds in the x and y directions were $\frac{dx}{dt} = \frac{dy}{dt} = \frac{ds/dt}{\sqrt{2}}$. The mirrors consisted of $3.6 \mu m$ deep, $80 \mu m$ long grooves cut into the wafer, as shown in the SEM micrograph of Fig. 4.16(a), where gratings with a line spacing of $0.25 \mu m$ and Si_3N_4 passivation layer are demonstrated.

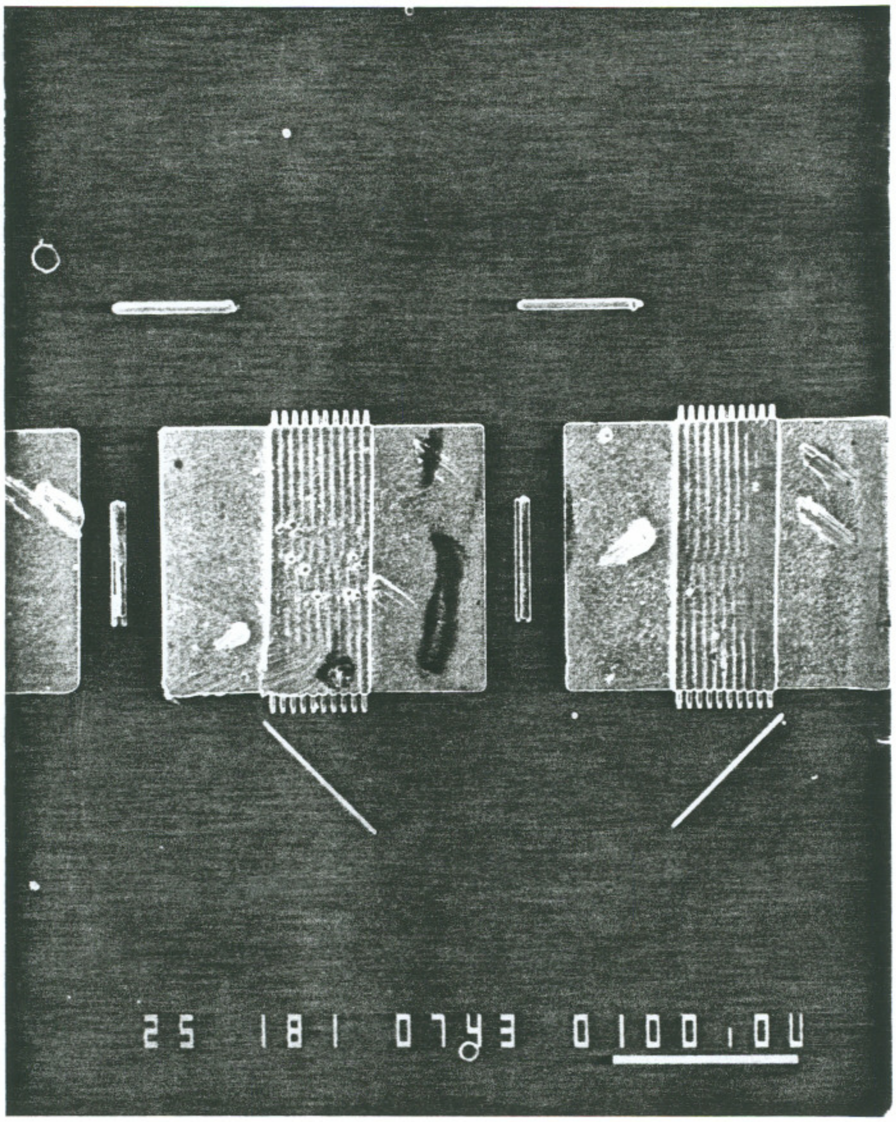

Figure 4.15 SEM micrograph of one 45° turning mirror and one ten-stripe laser array from each of the two array columns of a DBR-GSE diode laser device.

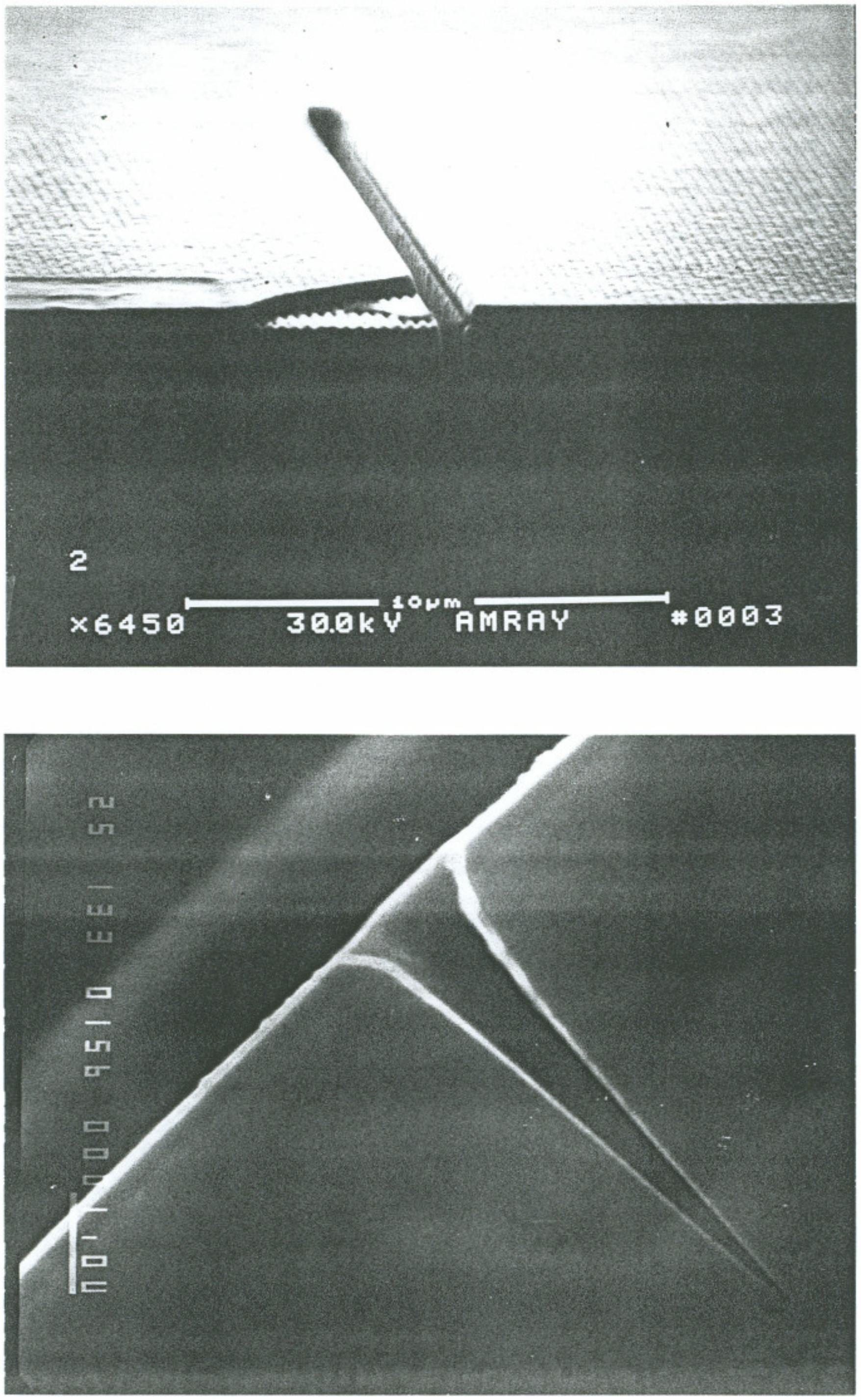

Figure 4.16 (a) Upper: SEM micrograph of a cleaved FIB micromachined groove, where gratings of a DBR-GSE diode laser device with a line spacing of $0.25\mu m$ and a Si_3N_4 passivation layer are recognizable. (b) Lower: SEM micrograph of a typical cross-section of a turning mirror.

A typical cross-section of such TIR turning mirrors is shown in the SEM micrograph of Fig. 4.16(b). There is a 3000Å-thick Si_3N_4 layer deposited by DSRC on the top of grating sections, where FIBM is to be performed. Note that due to the low sputtering yield of Si_3N_4, there is a slope discontinuity on the cross-section of the sidewalls (see Fig. 4.16(b)) at the interfacial plane of Si_3N_4 and AlGaAs. Also the gap and gap angle, at the interfacial plane of Si_3N_4 and AlGaAs, are $1.11\mu m$ and 7.04°.

Using the sputtering yield of Si_3N_4, which is $5.0 \times 10^{-6}cm^3mA^{-1}min^{-1}$ (determined by Zheng *et. al.*)[73] about four times lower than that of GaAs, a series of simulated cross-sectional profiles have been calculated by the split scan strategy (described in section 2.3.5) and shown in Fig. 4.17. As comparison, a series of simulated cross-sectional profiles on the top of the existing profiles have been calculated by a Gaussian beam without the Si_3N_4 layer. Also digitized cross-sections of the actual groove have also been shown in Fig. 4.17. However, the bottom of the actual groove was not very well defined in the magnified (2.5 ×) SEM micrograph. An open-end cross-section was thus produced. Note that the slope discontinuity occurred at different depth between the digitized cross-section and the simulated one, which could be due to the limitation of the simulation. The simulated profiles (from right to left) were "machined" using beam diameters from $0.3\mu m$ to $0.6\mu m$ in intervals of $0.1\mu m$. For the grooves with the Si_3N_4 layer, the gaps, gap angles and beam diameters, are given in the following table.

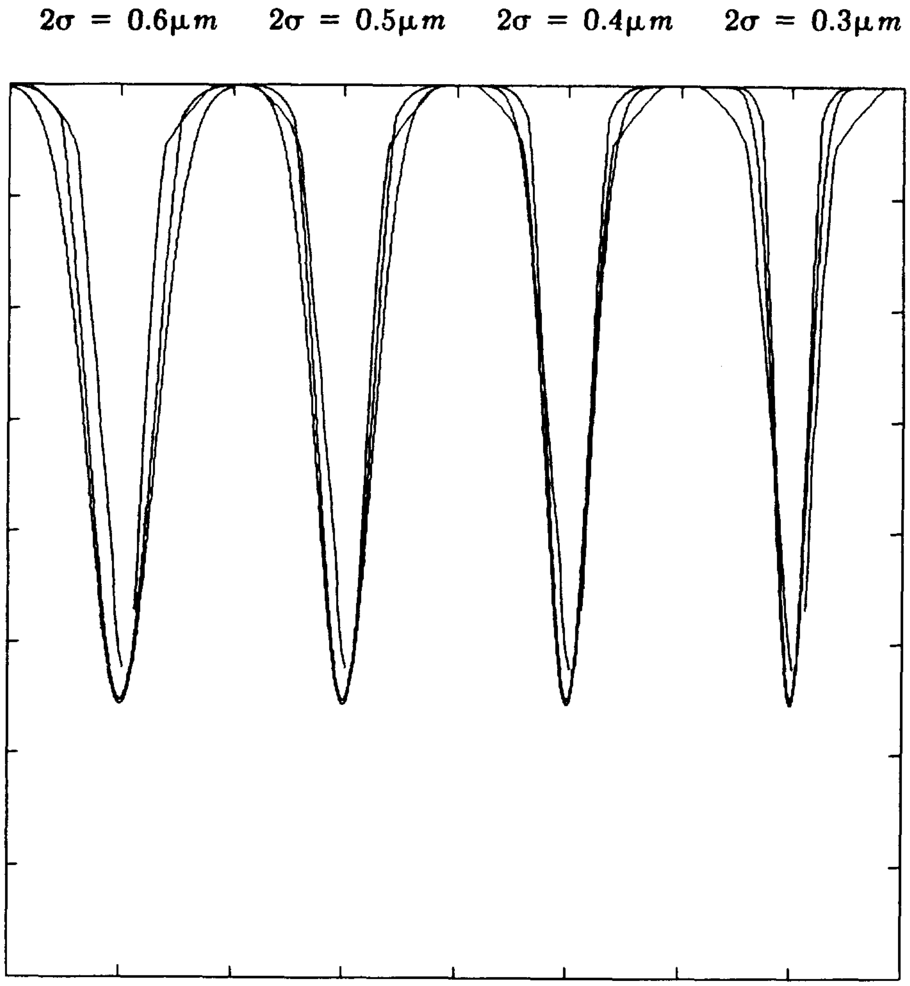

Figure 4.17 A series of cross-sectional profiles (from left to right) of the turning mirrors have been simulated using a Gaussian beam with a beam diameter of $0.3\mu m$ to $0.6\mu m$ in $0.1\mu m$ intervals. There are two cross-sections for each groove simulated by a Gaussian beam only (outer) and split scan approach (inner). As comparison, a digitized (irregular) cross-section of the actual groove was laid on the top of the simulated ones.

SIMULATION	1	2	3	4
GAP (μm)	0.52	0.70	0.89	1.07
ANGLE (°)	4.73	6.22	7.61	9.12
BD (μm)	0.3	0.4	0.5	0.6

The simulation results are not very satisfactory, because secondary effects are dominant in FIB micromachined structures with high depth aspect ratio. Since the actual and simulated cross-sections are grossly different, ERRs will not be calculated. The non-vertical side walls could be the primary difficulty for being a perfect total-internal-reflection turning mirror, because the laser light would be reflected off from the plane of the laser active region by the slanted side wall. The verticality of the slanted side walls may be improved by using an ion beam with a smaller spot size and a more uniform current distribution than the Gaussian distribution.

Note that, using the split scan strategy, all simulated profiles with the Si_3N_4 layer have some discontinuities in the slopes of their side walls at the interfacial plane of Si_3N_4 and AlGaAs, while no such discontinuities are observed in the side walls of the grooves without the Si_3N_4 layer. For the simulated grooves with the Si_3N_4 layer, the profile with a 0.4μm beam diameter simulates the slope of the lower part of side walls at the AlGaAs layer best, while the profile with a 0.6μm beam diameter simulates the slope of the upper part of curved side walls at the Si_3N_4 layer better. In other words, the lower part of the machined groove seems to be machined by a ion beam with small beam diameter, while the upper part seems to be machined by a ion beam with larger beam diameter. This could be explained that the upper portion of the groove received a larger ion dose as result of an actual current distribution, i.e. a longer non-Gaussian tail, while the lower portion of the groove suffered from redeposition and ion beam reflection effects. In detail, redeposition effects would make the sputtered material re-deposit to the side walls and the reflected ions would sputter more material from the central portion of sharp "V" grooves.

Furthermore, because of the low sputtering yield of Si_3N_4, the micromachined grooves are always narrower than those fabricated without a Si_3N_4 layer, because the Si_3N_4 layer can minimize the sputtering etch by Ga^+ ions from the tail of the Gaussian beam. Only ions from the center portion of the ion beam will penetrate through the Si_3N_4 layer. Once the ions meet the bulk of the AlGaAs, the sputtering yield will be increased by a factor of up to three[73,79], and the gap width of the micromachined grooves is decreased, because only a limited amount of Ga^+ ions from the center of the current distribution contributes most of the sputtering.

When a pair of FIB micromachined 45° turning mirrors is machined at the end of two columns of DBR-GSE laser Q2D arrays, as shown in Fig. 4.15, occasionally the emission spectra of the two columns is injection locked and the spectrum of one of the columns can be shifted by varying the drive current to each gain section in the other column[39]. Furthermore, single longitudinal mode operation has been demonstrated by placing an additional pair of 45° such mirrors at the other end of the columns in order to form a ring laser[40], as shown in the SEM micrograph of Fig. 4.18. Such a novel way for routing the laser light from one optical waveguide to another, monolithically

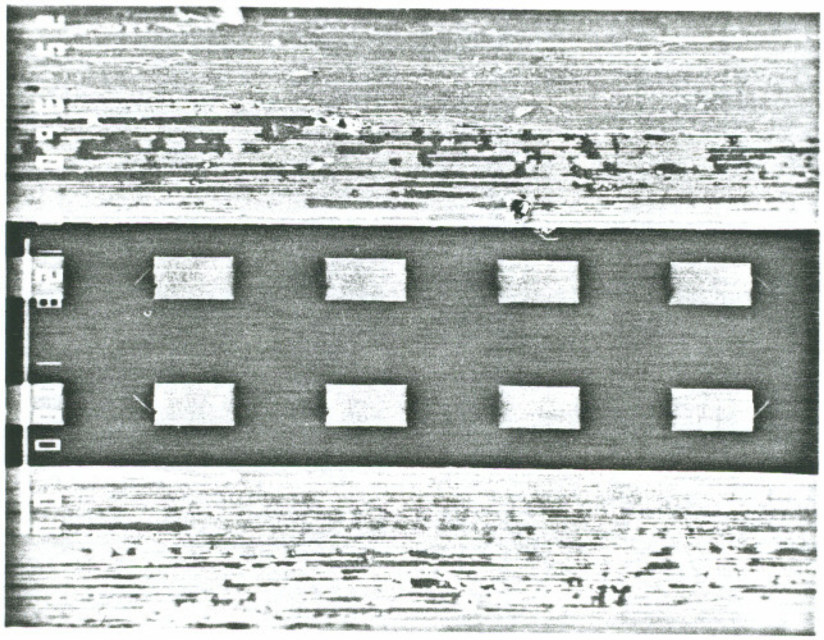

Figure 4.18 SEM micrograph of a top view of a GSE ring laser with one 45° turning mirrors at each end of the two array columns.

in the plane of the wafer, is a significant development in FIB applications for fabricating various novel and new integrated laser structures.

To this point, we have not fully taken advantage of the 3-D digital scan strategy. One could rotate the ion beam electrically or rotate the sample stage mechanically by 45° (relative to the optical waveguide axis), and make straight lines again. But it is easier to align the optical axis horizontally and to scan the ion beam along 45° scan lines. For different applications shown later, however, the traditional scan strategy of FIB micromachined features, (namely lines and rectangles), cannot meet the requirements of specific applications. Also, for the consistency of this turning mirror method, we still assume plane 45° turning mirrors as structures machined by the variable-scan-speed strategy. The method for developing more complicated turning mirrors, such as retroreflectors ("V" and micro-"V" turning mirrors) and parabolic turning mirrors will be discussed later.

4.3.2 "V" and Micro-"V" Turning Mirrors

It was hoped that we could enhance the lateral coupling of a DBR-GSE Q2D ten-stripe laser array by micromachining "V" or micro-"V" TIR turning mirrors at each end of one column of the laser array, but no enhancement has been found so far. As one of applications of the 3-D scan strategy, the formation of the "V" or micro-"V" mirrors by scanning the ion beam continuously along a "V" shaped path or a saw-toothed path respectively has been demonstrated. Fig. 4.19(a) is a SEM micrograph of a "V" mirror and a ten-stripe laser array where the "V" mirror will act as a retroreflector to reflect the light

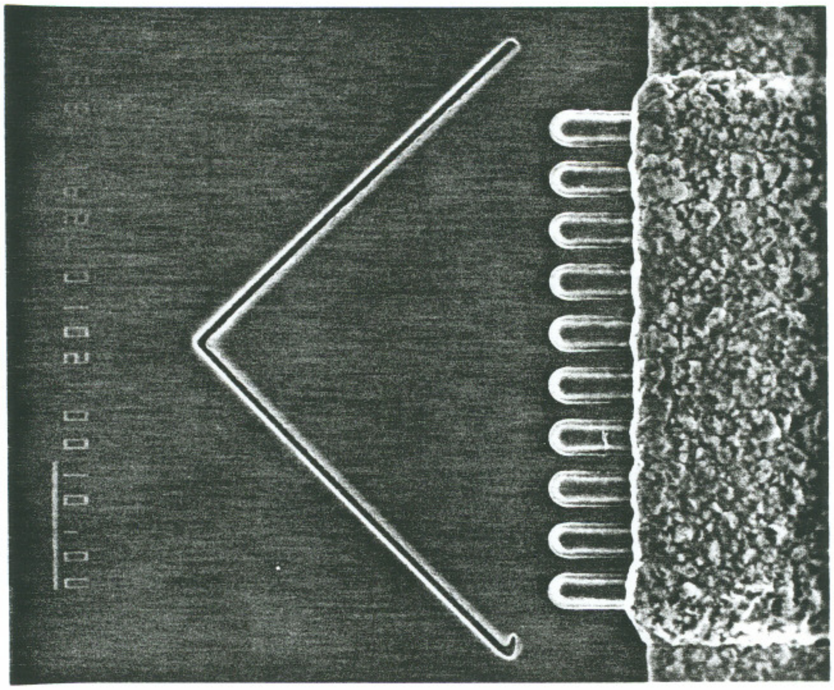

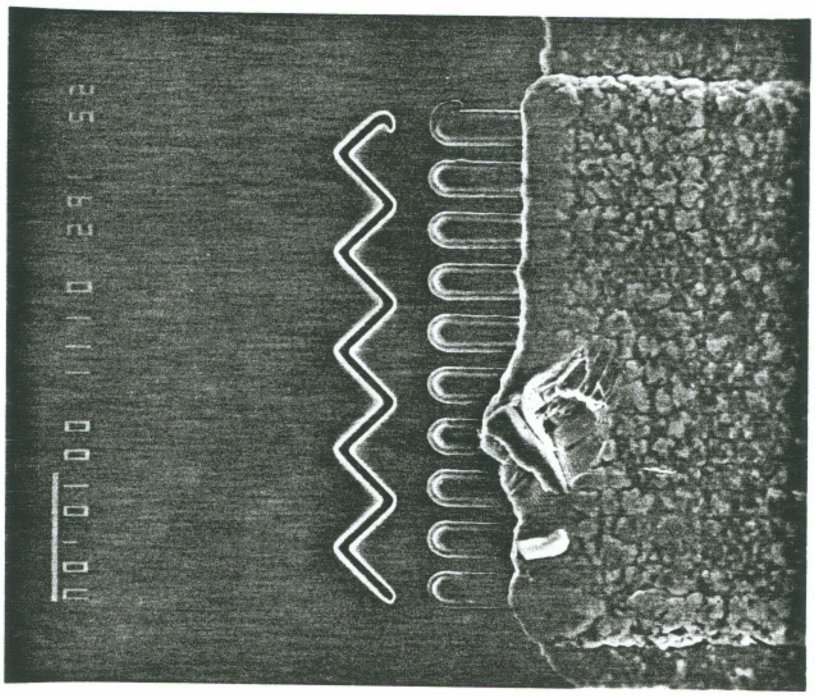

Figure 4.19 (a) Upper: SEM micrograph of one "V" retroreflector and one ten-stripe laser array. (b) Lower: SEM micrograph of one micro-"V"s retroreflector and one ten-stripe laser array.

output from the top five stripes to the bottom five ones. Similarly, in Fig. 4.19(b), the saw-toothed 5-micro-"V" retroreflector will reflect the light output from one stripe to another. At the other end of the array column, a 4-micro-"V" retroreflector was placed with one stripe shift. However, the open angle between two branches of the "V" or micro-"V" is really 89°, not 90°, probably due to uncertainty of the 12-bit DAC's employed in the FIB workstation, which would result in the misalignment of the open angles of the "V" mirrors.

As to the scan strategy for the ion beam, these "V" mirrors could not be machined by connecting different segments of rotated 45° straight lines, because at the junction of two line segments redeposited materials would fill up the previously machined groove. Thus the continuous scan is preferred. Prior to the actual FIB micromachining, a host computer first calculates a look-up table of bit-address of DAC's for a saw-toothed path taking into consideration constant of $\frac{ds}{dt}$. Then the ion beam will be scanned according to the determined look-up table.

A 3-D simulation of the FIBM process could be performed to examine the 3-D structures, as shown in Fig. 4.20, where top and inverted views of a "V" structure can be seen. Also, at the corner of the "V" crater, the depth is greater than the rest of the crater because three scan points (one from the top of the "V" and two from each branch of the "V") intersect there. In other words, the overlap of the Gaussian beam at the intersection of the above-mentioned three scan points is greater than the rest of the crater(see Fig. 4.21).

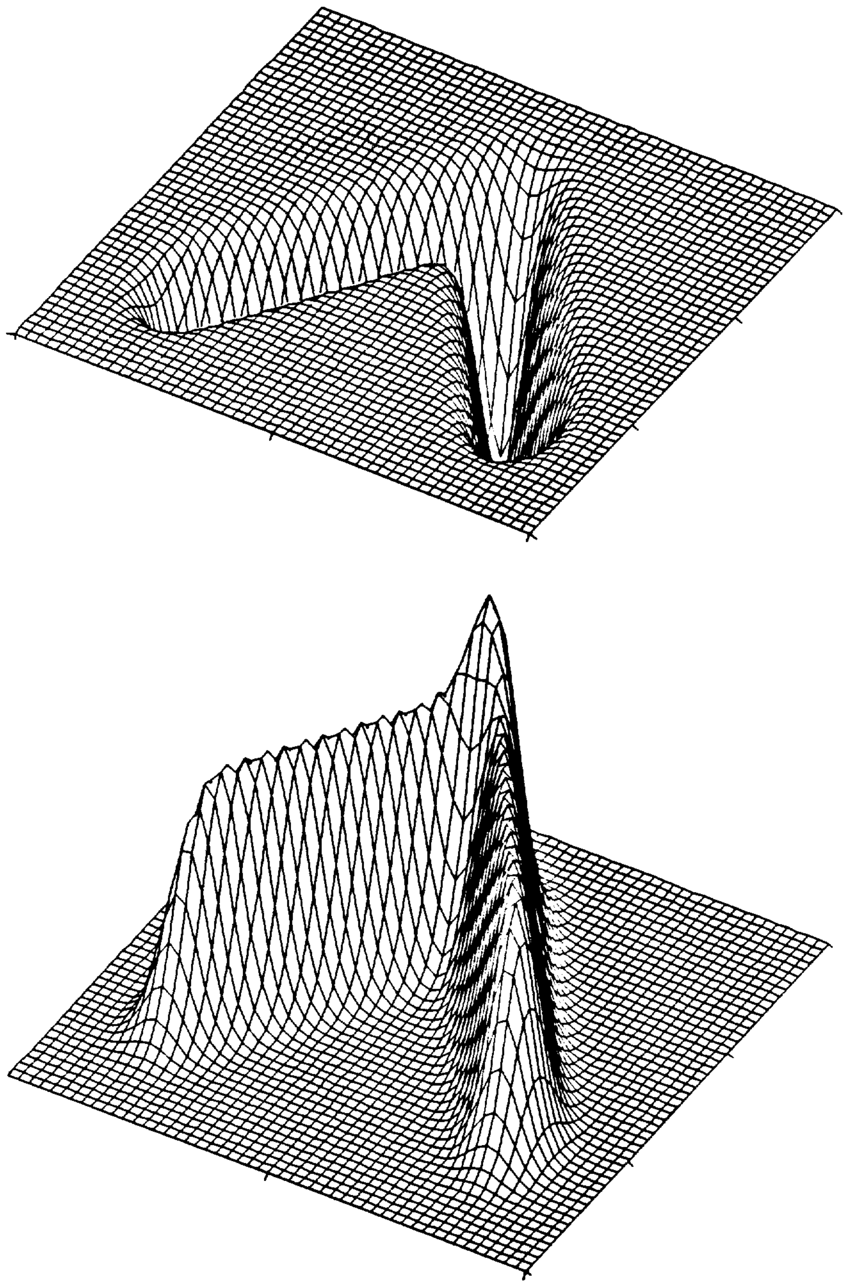

Figure 4.20 3-D top and inverted views of a simulated "V" turning mirror. Note that, at the corner of the "V" crater, the depth is greater than the rest of the crater.

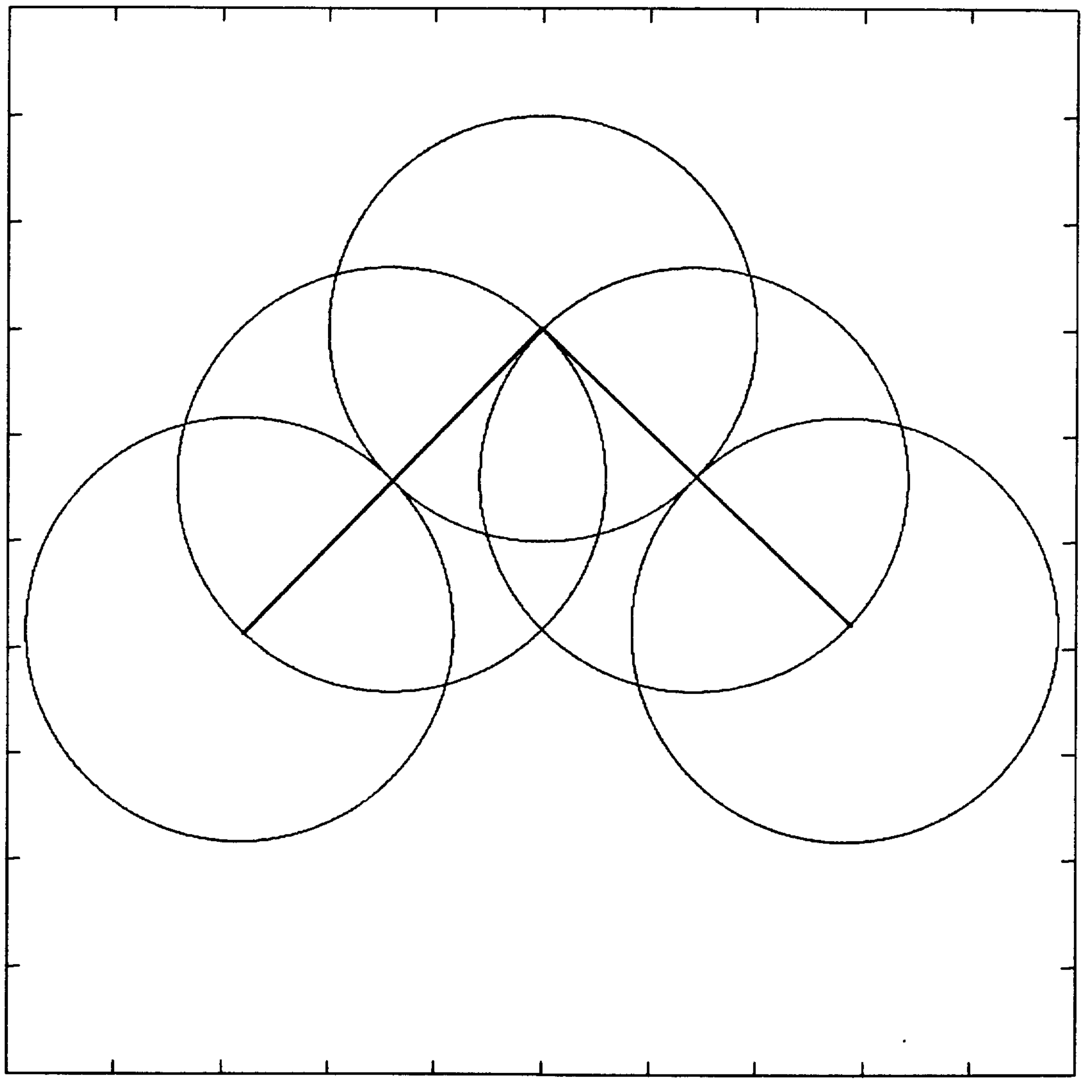

Figure 4.21 Five intersected circles represent the scan points of the Gaussian beam at the corner of the "V" crater.

4.3.3 Parabolic Turning Mirrors

As another application of the 3-D scan strategy, fabrication of a pair of confocal, right angle, off-axis parabolic turning mirrors has been accomplished by FIB micromachining. One of the parabolic mirrors has been placed at one end of a broad area DBR-GSE array column, as shown in the SEM micrograph of Fig. 4.22(a). With this structure one could perhaps make unstable resonator ring lasers. The straight line in the figure is a reference line used to determine the curvature of the parabolic line. In contrast to the plane 45° turning mirrors, the parabolic mirror was designed to focus the collimated light output from a broad-area laser column and then another such mirror placed in the front of an adjacent laser column would collimate and inject the light into that column. To complete the unstable resonator ring laser, a pair of plane 45° turning mirrors is needed at the other end of the columns, as shown in the SEM micrograph of Fig. 4.22(b). However, these unstable resonator ring lasers have not yet shown any difference in the lasing characteristics relative to the ring lasers with plane 45° turning mirrors.

The computer is used to first calculate the bit addresses, based upon the desired scan strategy and desired parabolic path functions, and then used to control the 12-bit DAC's to fabricate parabolic turning mirrors with uniform depth profile. However, such parabolic curves are indeed machined by scanning the ion beam along a straight line between two adjacent scan points, over a set of many discrete scan points. Therefore the ability to approach a mathematically smooth path function is limited by the resolution of the DAC's.

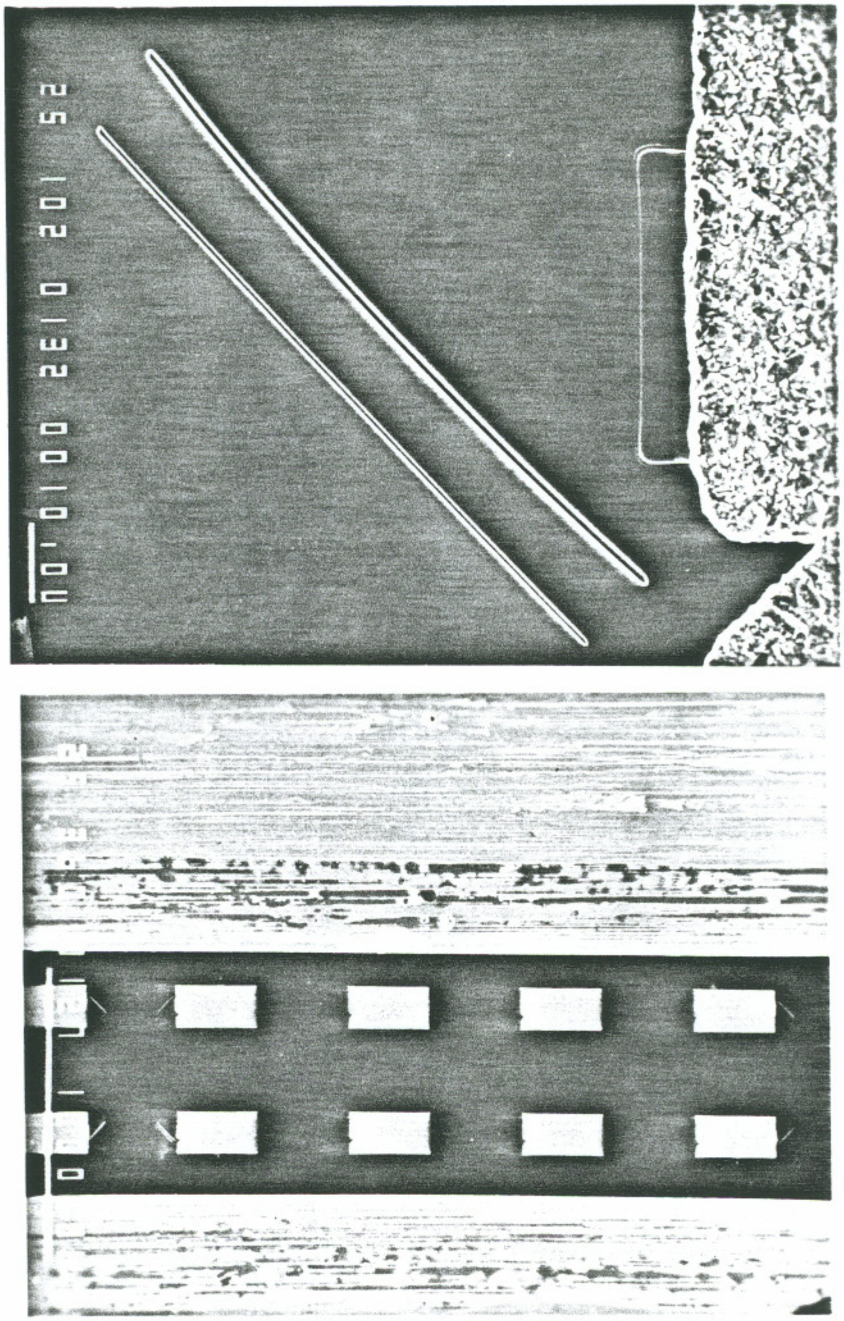

Figure 4.22 (a) Upper: SEM micrograph of one parabolic turning mirror and one board-area laser array, where the straight line in the figure is a reference line. (b) Lower: SEM micrograph of a GSE unstable resonator ring laser, where two plane 45° turning mirrors have been placed at one end of two laser columns, and two parabolic turning mirrors placed at the other end.

4.4 Discussions and prospects

Due to the flexibility of our 3-D digital scan strategy, any 3-D structures with arbitrary path functions and desired depth profiles can, in principal, be fabricated by the ion beam. However, there could be a "refill" problem at the intersection of two scan lines, if the depth difference between the already machined groove and the groove presently being milled was pronounced, because of redeposition effects. This suggests that removal of material should be minimal at each scan of the ion beam.

As one of many prospects for this 3-D digital scan strategy, the Ga^+ ion beam has been scanned in a series of concentric circles to make circular gratings with line spacing of $0.53\mu m$, which could be useful to form "bull's eye" lasers, as shown in the SEM micrograph of Fig. 4.23. However, due to the ion beam induced damage, the FIB micromachined circular gratings may not be practically useful. By fabricating curved optical coupling etalons in coupled-cavity diode laser devices, unstable coupled-cavity diode lasers could be formed, as well.

As mentioned in the introduction, the preliminary attempt at a better understanding of the FIBM technique, by developing a 3-D simulation and a 3-D ion beam scan strategy, would provide software support for computer controlled FIB micromachining, which could be further developed to provide some computer-aided-design (CAD) abilities for the existing FIB micromachining workstations.

Remember that simulation is not a curve-fitting procedure. The curve

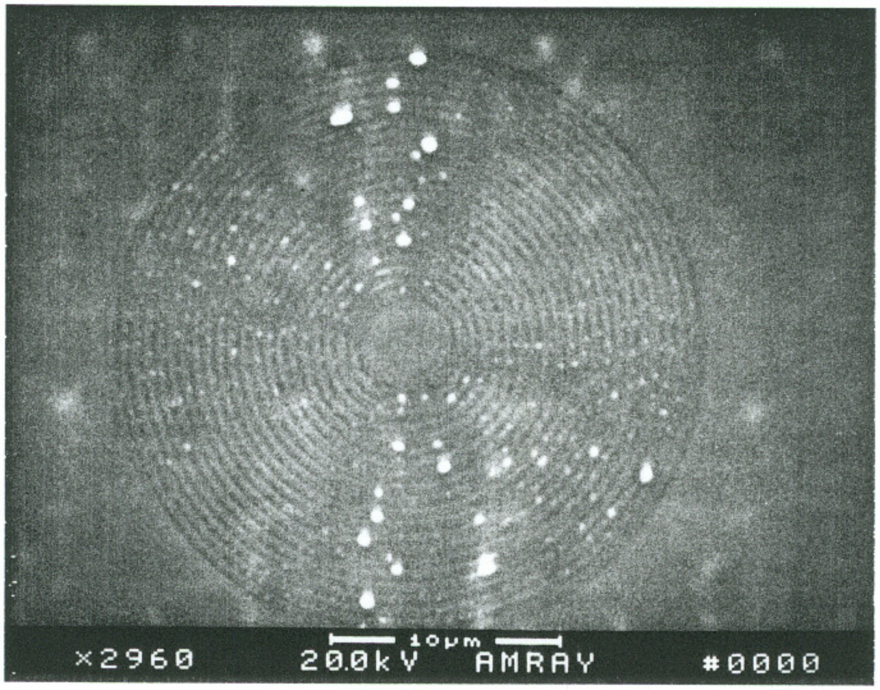

Figure 4.23 SEM micrograph of a series of concentric circles with a line spacing of $0.53\mu m$, micromachined by constant scan speeds along the arc.

fitting is to select the best fitting to an existing curve among all possible curves, by changing a number of parameters. Then, if another curve needs to be fitted, another set of parameters may be obtained by selecting the best fit to this curve. However, these two sets of parameters may have correlation in some extent. On the other hand, the simulation is used to predict certain physical processes. Once input parameters of the simulation are calibrated, they will not be adjusted during the entire process. For example, the 3-D computer simulation of FIBM has two input parameters: K and σ. After K was determined for given substrates, and σ was calibrated for the ion beam in a particular experimental setup, the physical process would change the line spacing to fabricate different gratings (see Fig. 4.2 and 4.5), and could be simulated by the simulation with constant K and σ. Therefore, consistency of a simulation is a key to clarify whether the simulation is legitimate.

5. CONCLUSION AND FUTURE RESEARCH

After theoretical and experimental studies of FIBM, a computer simulation program in three-dimensional space and a fully-digitized, non-linear, three-dimensional, variable-scan-speed ion beam scan strategy have been developed which can fabricate and simulate arbitrarily curved 3-D features with desired depth profiles, such as "V", micro-"V" and parabolic mirrors. However, the simulation mainly works for shallow features. In-wafer monolithic fabrication of various kinds of optical elements such as turning mirrors, retroreflectors and focusing mirrors in semiconductor diode laser materials has been produced by this scan strategy.

The simulation results have not fully agreed with experimental results, except in the cases where the depth aspect ratio is less than 2:1. The cross-sections of turning mirrors are sharp "V" shapes, as shown in Fig. 4.16(b), due to secondary effects, (i.e. mainly sputtering yield angular dependency, ion reflection, and redeposition). Therefore a more sophisticated 3-D simulation, taking into account secondary effects such as sputtering yield angular dependency, redeposition, and ion reflection, must be developed.

High energy ions have the ability to remove atoms from substrates and also have the ability to induce damage to the crystal structure of the substrates. When modifications on semiconductor diode laser devices by FIB micromachining, such damage has to be investigated thoroughly in order to be able to modify the devices properly, rather than to destroy them. However, the mechanism of such FIB induced damage cannot be revealed by the simple detection experiments on DBR-GSE diode laser devices, as described in Appendix A. More systematic and sophisticated damage detection experiments need to be carried out.

References

1. Ian G. Brown, *The Physics And Technology of Ion Sources,* JOHN WILEY & SONS, New York, 1989.

2. R. Gomer, "On the Mechanism of Liquid Metal Electron and Ion Sources," *Applied Physics*, vol. 19, pp. 365-375, 1979.

3. D. R. Kingham and L. W. Swanson, "Mechanism of Ion Formation In Liquid Metal Ion Source," *J. De. Physique*, vol. C9, pp. 133-138, 1984.

4. D. R. Kingham and L. W. Swanson, "Theoretical Investigation of Liquid Metal Ion Sources: Field and Temperature Dependence of Ion Emission," *Applied Physics A*, vol. 41, pp. 157-169, 1986.

5. G. Benassayag, P. Sudraud, and B. Jouffrey, "In Situ High Voltage TEM Observation of an Electro-hydrodynamic (EHD) Ion Source," *Ultramicroscopy*, vol. 16, pp. 1-8, 1985.

6. D. R. Kingham and L. W. Swanson, "Shape of Liquid Metal Ion Source: A Dynamic Model Including Fluid Flow and Space Charge Effects," *Applied Physics A*, vol. 34, pp. 123-132, 1984.

7. A. Wagner, "The Hydrodynamics of Liquid Metal Ion Sources," *Applied Physics Letters*, vol. 40(5), pp. 440-442, 1982.

8. G. L. R. Mair, "Space-charge Effects in Liquid Metal Ion Sources," *J. Physics D: Applied Physics*, vol. 15, pp. 2523-2530, 1982.

9. G. L. R Mair, "Theoretical Determination of Current-Voltage Curves for Liquid Metal Ion Sources," *J. Phys. D: Appl. Phys.*, vol. 17, pp. 2323-2330, 1984.

Liquid Metal Ion Sources," *J. Phys. D: Appl. Phys.*, vol. 17, pp. 2323-2330, 1984.

10. G. L. R. Mair, "An Analytical Expression for the Current-Voltage Characteristics of Capillary Type Liquid Metal Ion Sources," *J. De Physique*, vol. C9, pp. 173-177, 1984.

11. J. Orloff and L. W. Swanson, "An Asymmetric Electrostatic Lens for Field-Emission Microprobe Applications," *J. Appl. Phys.*, vol. 50(4), pp. 2494-2501, April 1979.

12. J. Orloff, "The Effect of Extraction Voltage and Beam Voltage of a Liquid Metal Ion Source Focused Beam System on the Current Density in a Focused Spot," *Scanning Electron Microscopy*, vol. IV, pp. 1541-1546, 1984.

13. Peter Sigmund, "Theory of Sputtering. I. Sputtering Yield of Amorphous and Polycrystalline Targets," *Physical Review*, vol. 184(2), pp. 383-416, 10 August 1969.

14. H. Oechsner, "Sputtering -- a Review of Some Recent Experimental and Theoretical Aspects," *Appl. Phys.*, vol. 8, pp. 185-198, 1975.

15. C. R. Fritzsche and W. Rothemund, "Sputtering during Ion Implantation into Gallium Arsenide," *Appl. Phys.*, vol. 7, pp. 39-44, 1975.

16. P. Sigmund, "Sputtering Processes: Collision Cascades and Spikes," *Inelastic Ion-Surface Collisions" edited by N. H. Tolk, J. C. Tully, W. Heiland, and C. W. White.*, pp. 121-152, Academic Press, Inc., New York, 1977.

17. S. A. Schwarz and C. R. Helms, "A Statistical Model of Sputtering," *J. Appl. Phys.*, vol. 50(8), pp. 5492-5499, August 1979.

18. R. Behrisch, G. Maderlechner, b. M. U. Scherzer, and M. T. Robinson, "The Sputtering Mechanism for Low-Energy Light Ions," *Appl. Phys.*, vol. 18, pp. 391-398, 1979.

19. M. Hou and M. T. Robinson, "Computer Simulation of Low-Energy Sputtering in the Binary Collision Approximation," *Appl. Phys.*, vol. 18, pp. 381-389, 1979.

20. R. Behrisch, "Sputtering by Particle Bombardment I," *Topics in Applied Physics*, vol. 47, Springer-Verlag, Berlin Heidelberg New York, 1981.

21. Y. Yamamura, "Theory of Sputtering and Comparison to Experimental Data," *Nuclear Instruments and Methods*, vol. 194, pp. 515-522, 1982.

22. M. Szymonski and A. Poradzisz, "A Model of Sputtering from Spikes," *Appl. Phys. A*, vol. 28, pp. 175-178, 1982.

23. P. Sigmund and M. Szymonski, "Temperature-Dependent Sputtering of Metals and Insulators," *Appl. Phys. A*, vol. 33, pp. 141-152, 1984.

24. G. Falcone and A. Oliva, "Sputtering of Multicomponent Materials," *Appl. Phys. A*, vol. 33, pp. 175-178, 1984.

25. W. Husinsky, G. Betz, I. Girgis, F. Viehbock, and H. L. Bay, "Velocity Distributions and Sputtering Yields of Chromium Atoms under Argon, Oxygen and Carbon Ion Bombardment," *Journal of Nuclear Materials*, vol. 128 & 129, pp. 577-582, 1984.

26. Yoshikazu Homma and Yoshikazu Ishii, "Surface Sputtering Rate

Reduction and its Effect on SIMS Depth Profiling in Cesium-Ion-Bombarded GaAs," *J. Vac. Sci. Technol.*, vol. A 3(2), pp. 351-355, Mar/Apr 1985.

27. G. Carter, M. J. Nobes, and J. L. Whitton, "Sputtering Induced Topography Development on f.c.c. Metals," *Appl. Phys. A*, vol. 38, pp. 77-95, 1985.

28. Ch. Steinbruchel, "A Simple Formula for Low-Energy Sputtering Yields," *Appl. Phys. A*, vol. 36, pp. 37-42, 1985.

29. M. Hou, "A Comparison of Deposited Energy in Statistical and Individual Cascades Generated in Amorphous and Polycrystalline Materials," *Nuclear Instruments and Methods in Physics Research*, vol. B13, pp. 331-337, Elsevier Science Publishers B.V., North-Holland, Amsterdam, 1986.

30. Y.-T. Cheng, M.-A. Nicolet, and W. L. Johnson, "From Cascade to Spike -- a Fractal-Geometry Approach," *Physical Review Letters*, vol. 58(20), pp. 2083-2086, 18 May 1987.

31. G. P. Chen, J. von Seggern, H. Gnaser, and W. O. Hofer, "Sputtering Yields of Nickel and Chromium," *Appl. Phys. A*, vol. 49, pp. 711-717, 1989.

32. J. P. Biersack and W. Eckstein, "Sputtering Studies with the Monte Carlo Program TRIM.SP," *Appl. Phys. A*, vol. 34, pp. 73-94, 1984.

33. W. Eckstein and J. P. Biersack, "Computer Simulation of Two-Component Target Sputtering," *Appl. Phys. A*, vol. 37, pp. 95-108, 1985.

34. M. Hou and W. Eckstein, "Computer Simulation of Low Energy Static Single Crystal Sputtering," *Nuclear Instruments and Methods in Physics Research,* vol. B13, pp. 324-330, Elsevier Science Publishers B.V., North-Holland, Amsterdam, 1986.

35. R. K. DeFreez, J. Puretz, R. A. Elliott, G. A. Crow, H. Ximen, D. J. Bossert, G. A. Wilson, and J. Orloff, "Focused-Ion-Beam Micromachined Diode Laser Mirrors," *Proceedings of the Society of Photo-Optical Engineers*, vol. 1043, pp. 25-35, 1989.

36. R. K. DeFreez, J. Puretz, J. Orloff, R. A. Elliott, H. Namba, E. Omura, and H. Namizaki, "Operating Characteristics and Elevated Temperature Lifetests of Focussed Ion Beam Micromachined Transverse Junction Stripe Lasers," *Appl. Phys. Lett.*, vol. 53, pp. 1153-1155, 26 September 1988.

37. R. K. DeFreez, J. Puretz, R. A. Elliott, J. Orloff, and L. W. Swanson, "CW Operation of Widely and Continuously Tunable Micromachined-Coupled-Cavity Diode Lasers," *Electron. Lett.*, vol. 22, pp. 919-921, 14 August 1986.

38. J. Puretz, R. K. DeFreez, R. A. Elliott, J. Orloff, and T. L. Paoli, "300 mW Operation of a Surface-Emitting Phase-Locked Array of Diode Lasers," *Electron. Lett.*, vol. 23, pp. 130-131, 29 January, 1987.

39. R. K. DeFreez, H. Ximen, D. J. Bossert, J. M. Hunt, G. A. Wilson, R. A. Elliott, J. Orloff, G. A. Evans, N. W. Carlson, M. Lurie, J. M. Hammer, D. P. Bour, S. L. Palfrey, and R. Amantea, "Spectral Locking in an Extended Area Two-Dimensional Coherent Grating-Surface-Emitting

Laser Array Fabricated Using Focused Ion Beam Micromachining," *IEEE Photonics Technol. Lett.*, vol. 2(1), pp. 6-8, January 1990.

40. D. J. Bossert, R. K. DeFreez, H. Ximen, R. A. Elliott, J. M. Hunt, G. A. Evans, N. W. Carlson, M. Lurie, J. M. Hammer, D. P. Bour, S. L. Palfrey, and R. Amantea, "Grating Surface Emitting Lasers in a Ring Configuration," *Appl. Phys. Lett.*, vol. 56(21), pp. 2068-2070, 21 May 1990.

41. G. Crow, J. Puretz, J. Orloff, R. K. DeFreez, and R. A. Elliott, "The Use of Vector Scanning for Producing Arbitrary Surface Contours with a Focused Ion Beam," *J. Vac. Sci. Technol. B,* vol. 6, pp. 1605-1607, September/October 1988.

42. K. P. Mueller, U. Weigmann, and H. Burghause, "Simulation of Focused Ion Beam Milling," *Microelectronic Engineering,* vol. 5, pp. 481-489, 1986.

43. A. R. Neureuther et.al., *SAMPLE,* EE/CS, University of California, Berkeley, CA 94720.

44. R. Smith and J. M. Walls, "The Development of a General Three-Dimensional Surface under Ion Bombardment," *Phil. Mag. A*, vol. 42(2), pp. 235-248, 1980.

45. R. Smith, T. P. Valkering, and J. M. Walls, "The Erosion of Amorphous and Crystalline Surfaces by Ion Bombardment," *Philosophical Magazine A*, vol. 44, No. 4, pp. 879-893, 1981.

46. R. Smith, M. A. Tagg, G. Carter, and M. J. Nobes, "Erosion of Corners and Edges on an Ion-Bombarded Silicon Surface," *J. Mat. Sci. Lett.*, vol.

5, pp. 115-120, 1986.

47. R. Smith, S. S. Makh, and J. M. Walls, "Surface Morphology During Ion Etching - The Influence of Redeposition," *Phil. Mag. A*, vol. 47(4), pp. 453-481, 1983.

48. R. Smith, M. A. Tagg, and J. M. Walls, "Deterministic Models of Ion Erosion, Reflection and Redeposition," *Vacuum*, vol. 34, No. 1-2, pp. 175-180, 1984.

49. R. Smith and M. A. Tagg, "An Algorithm to Calculate Secondary Sputtering by the Reflection of Ions in Two Dimensions," *Vacuum*, vol. 36, No. 5, pp. 285-288, 1986.

50. M. A. Tagg, R. Smith, and J. M. Walls, "Sample Rocking and Rotation in Ion Beam Etching," *J. Mat. Sci.*, vol. 21, pp. 123-130, 1986.

51. D. W. Youngner and C. M. Haynes, "Modeling Ion Beam Milling," *J. Vac. Sci. Technol.*, vol. 21(2), pp. 677-680, July/Aug. 1982.

52. H. Tsuge, S. Esho, and H. Gokan, "Simulation of Ion-Beam Etching Pattern Profiles," *J. Vac. Sci. Technol.*, vol. 19(2), pp. 221-224, Jul./Aug. 1981.

53. J. A. Valles-Abarca and A. Gras-Marti, "Comments on: "Simulation of Ion-Beam-Etched Pattern Profiles"," *J. Vac. Sci. Technol.*, vol. 21(3), pp. 891-892, Sept./Oct. 1982.

54. John L. Reynolds, Andrew R. Neureuther, and William G. Oldham, "Simulation of Dry Etching Line Edge Profiles," *J. Vac. Sci. Technol.*, vol. 16(6), pp. 1772-1775, Nov./Dec. 1979.

55. J. C. Moreno-Marin, J. A. Valles-Abarca, and A. Gras-Marti, "Secondary Effects in Ion Milling," *J. Vac. Sci. Technol.*, vol. B 4(1), pp. 322-325, Jan/Feb 1986.

56. Noriyoshi Yamauchi, Toshiaki Yachi, and Tsutomu Wada, "A Pattern Edge Profile Simulation for Oblique Ion Milling," *J. Vac. Sci. Technol.*, vol. A 2(4), pp. 1552-1557, Oct.-Dec. 1984.

57. M. Hou and M. T. Robinson, "The Conditions for Total Reflection of Low-Energy Atoms from Crystal Surfaces," *Appl. Phys.*, vol. 17, pp. 371-375, 1978.

58. R. E. Chapman, "Redeposition: a Factor in Ion-Beam Etching Topography," *J. Mat. Sci.*, vol. 12, pp. 1125-1133, 1977.

59. H. W. Lehmann, L. Krausbauer, and R. Widmer, "Redeposition-A Serious Problem in rf Sputter Etching of Structures with Micronmeter Dimensions," *J. Vac. Sci. Technol.*, vol. 14, No. 1, pp. 281-284, Jan./Feb. 1977.

60. A. R. Neureuther, C. Y. Liu, and C. H. Ting, "Modeling Ion Milling," *J. Vac. Sci. Technol.*, vol. 16(6), pp. 1767-1771, Nov./Dec. 1979.

61. I. W. Rangelow, P. Thoren, and R. Kassing, "Computer Simulation of Pattern Profiles Through Physical Etching with Shadow, Trenching, and Redeposition," *Microelectronic Engineering*, vol. 3, pp. 631-638, 1985.

62. Jurgen Lorenz, Joachim Pelka, Heiner Ryssel, Albert Sachs, Albert Seidl, and Milos Svoboda, "COMPOSITE-A Complete Modeling Program of Silicon Technology," *IEEE Transactions on Computer-Aided Design*, vol. CAD-4, No. 4, pp. 421-430, Oct. 1985.

63. K. P. Mueller and J. Pelka, "Redeposition in Ion Milling," *Microelectronic Engineering*, vol. 7, pp. 91-101, 1987.

64. L. R. Harriott, "Beam-Size Measurements in Focused Ion Beam Systems," *J. Vac. Sci. Technol.*, vol. A 8(2), pp. 899-901, Mar/Apr 1990.

65. J. W. Ward, M. W. Utlaut, and R. L. Kubena, "Computer Simulation of Current Density Profiles in Focused Ion Beams," *J. Vac. Sci. Technology*, vol. B 5(1), pp. 169-174, Jan/Feb 1987.

66. J. W. Ward, R. L. Kubena, and M. W. Utlaut, "Transverse Thermal Velocity Broadening of Focused Beams From Liquid Metal Ion Source," *J. Vac. Sci. Technology*, vol. B 6(6), pp. 2090-2094, Nov/Dec 1988.

67. K. D. Cummings, L. R. Harriott, G. C. Chi, and F. W. Ostermayer Jr., "Micron Features in III-V Materials by Photoelectrochemical Etching of Focused Ion Beam Induced Damage Patterns," *Proceedings of the SPIE*, vol. 632, pp. 93-96, 1986.

68. John Melngailis, "Critical Review: Focused Ion Beam Technology and Applications," *J. Vac. Sci. Technol.*, vol. B 5(2), pp. 469-495, Mar/Apr 1987.

69. Masanori Komuro, "Radii Broadening due to Molecular Collision in Focused Ion Beams," *Appl. Phys. Lett*, vol. 52 (1), pp. 75-77, 4 January 1988.

70. Tetsuo Morita, Eizo Miyauchi, Hiroshi Arimoto, Akira Takamori, Yasuo Bamba, and Hisao Hashimoto, "Geometrical Design of an Alignment Mark for Focused Ion Beam Implantation in GaAs Using Monte Carlo Simulation of Ion Trajectories," *J. Vac. Sci. Technol.*, vol. B 5(1), pp.

236-240, Jan/Feb 1987.

71. Tetsuo Morita, Hiroshi Arimoto, Eizo Miyauchi, and Hisao Hashimoto, "Novel Methods for Measuring Diameter of Focused Ion Beam," *Jap. J. Appl. Phys.*, vol. 26, No. 2, pp. 289-292, February 1987.

72. M. Taneya, Y. Sugimoto, and K. Akita, "Characterization of Subsurface Damage in GaAs Processed by Ga^+ Focused Ion-Beam-Assisted Cl_2 Etching Using Photoluminescence," *J. Appl. Phys.*, vol. 66(3), pp. 1375-1381, 1 August 1989.

73. Zheng Xu, Kenji Gamo, and Susumu Namba, "Ion Beam Assisted Etching of SiO_2 and Si_3N_4," *J. Vac. Sci. Technol. B*, vol. 6(3), pp. 1039-04, May/Jun 1988.

74. S. Matsui, Y. Ochiai, Y. Kojima, H. Tsuge, N. Takado, K. Asakawa, H. Matsutera, J. Fujita, T. Yoshitake, and Y. Kubo, "Focused Ion Beam Processes for High-T_c Superconductors," *J. Vac. Sci. Technol.*, vol. B 6(3), pp. 900-905, May/Jun 1988.

75. Yukinori Ochiai, Kenji Gamo, Susumu Namba, Kazuhiko Shihoyama, Akio Masuyama, Takao Shiokawa, and Koichi Toyoda, "Temperature Dependence of Maskless Ion Beam Assisted Etching of InP and Si Using Focused Ion Beam," *J. Vac. Sci. Technol.*, vol. B 5(1), pp. 423-426, Jan/Feb 1987.

76. Yukinori Ochiai, Kazuhiko Shihoyama, Takao Shiokawa, Koichi Toyoda, Akio Masuyama, Kenji Gamo, and Susumu Namba, "Characteristics of Maskless Ion Beam Assisted Etching of Silicon Using Focused Ion Beams," *J. Vac. Sci. Technol.*, vol. B 4(1), pp. 333-336, Jan/Feb 1986.

77. Yukinori Ochiai, Kenji Gamo, and Susumu Namba, "Pressure and Irradiation Angle Dependence of Maskless Ion Beam Assisted Etching of GaAs and Si," *J. Vac. Sci. Technol.*, vol. B 3(1), pp. 67-70, Jan/Feb 1985.

78. R. A. Barker, T. M. Mayer, and W. C. Pearson, "Surface Studies of and a Mass Balance Model for Ar^+ Ion-Assisted Cl_2 Etching of Si," *J. Vac. Sci. Technol.*, vol. B 1(1), pp. 37-42, Jan.-Mar. 1983.

79. Yukinori Ochiai, Kenji Gamo, and Susumu Namba, "Characteristics of Ion Beam Assisted Etching of GaAs Using Focused Ion Beam: Dependence on Gas Pressure," *Jap. J. of Appl. Phys.*, vol. 23, No. 6, pp. L400-L402, June, 1984.

80. L. R. Harriott, R. E. Scotti, K. D. Cummings, and A. F. Ambrose, "Micromachining of Optical Structures with Focused Ion Beams," *J. Vac. Sci. Technology*, vol. B 5, pp. 207-210, January/February 1987.

81. L. R. Harriott, R. E. Scotti, K. D. Cummings, and A. F. Ambrose, "Micromachining of Integrated Optical Structures," *Appl. Phys. Lett.*, vol. 48, pp. 1704-1706, 23 June 1986.

82. L. R. Harriott, "A Second Generation Focused Ion Beam Micromachining System," *Electron-Beam X-Ray and Ion-Beam Lithographies VI*, vol. SPIE 773, pp. 190-194, 1987.

83. H. Yamaguchi, A. Shimase, S. Haraichi, and T. Miyauchi, "Characteristics of Silicon Removal by Fine Focused Gallium Ion Beam," *J. Vac. Sci. Technol.*, vol. B 3(1), pp. 71-74, Jan/Feb 1985.

84. H. Yamaguchi, "Line Dose Dependence of Silicon and Gallium Arsenide Removal by a Focused Gallium Ion Beam," *Journal De Physique*, vol. C6, No. 11, pp. 165-170, Novembre 1987.

85. Hiroshi Yamaguchi, "Sputter Etching by Focused Ion Beams," *Advances in Solid State Technology*, D. Reidel Publishing Company, Holland.

86. J. Puretz, R. K. DeFreez, R. A. Elliott, and J. Orloff, "Focused-Ion-Beam Micromachined AlGaAs Semiconductor Laser Mirrors," *Electron. Lett.*, vol. 22, pp. 700-702, 19 June 1986.

87. Joseph Puretz, "A Theoretical and Experimental Study of Liquid Metal Ion Sources and their Application to Focused Ion Beam Technology," *Dissertation*, AP/EE Oregon Graduate Institute, OR 97006-1999, Dec. 1988.

88. T. Ishitani, A. Shimase, and H. Tamura, "Condensation of Bombarding Gallium Ions on a Silicon Surface," *Appl. Phys. Lett.*, vol. 39(8), pp. 627-628, 15 October 1981.

89. Fumio Koyama, Susumu Kinoshita, and Kenichi Iga, "Room-Temperature Continuous Wave Lasing Characteristics of a GaAs Vertical Cavity Surface-Emitting Laser," *Appl. Phys. Lett.*, vol. 55(3), pp. 221-222, 17 July 1989.

90. G. A. Evans, N. W. Carlson, J. M. Hammer, M. Lurie, J. K. Butler, S. L. Palfrey, R. Amantea, L. A. Carr, F. Z. Hawrylo, E. A. James, C. J. Kaiser, J. B. Kirk, and W. F. Reichert, "Two Dimensional Coherent Laser Arrays Using Grating Surface Emission," *IEEE J. Quantum Electron.*, vol. 25, pp. 1525-1538, June 1989.

91. Hideto Miyake, Toshihiko Yuba, Kenji Gamo, Susumu Namba, and Takao Shiokawa, "Defects Induced by Focused Ion Beam Implantation in GaAs," *J. Vac. Sci. Technol. B*, vol. 6(3), pp. 1001-05, May/Jun 1988.

92. K. Kanaya and H. Kawakatsu, "Secondary Electron Emission due to Primary and Backscattered Electrons," *J. Phys. D: Appl. Phys.*, vol. 5, pp. 1727-1742, 1972.

93. G. Carter and J. S. Colligon, *Ion Bombardment of Solids,* AMERICAN ELSEVIER PUBLISHING COMPANY, INC., 1968.

94. D. G. Lishan, H. F. Wong, D. L. Green, E. L. Hu, J. L. Merz, and D. Kirillov, "Dry Etch Induced Damage in GaAs Investigated Using Raman Scattering Spectroscopy," *J. Vac. Sci. Technol.*, vol. B 7(3), pp. 556-560, May/Jun 1989.

95. Fusao Shimokawa, Hidenao Tanaka, Yuji Uenishi, and Renshi Sawada, "Reactive-Fast-Atom Beam Etching of GaAs Using Cl_2 Gas," *J. Appl. Phys.*, vol. 66(6), pp. 2613-2618, 15 September 1989.

96. A. Scherer, H. G. Craighead, M. L. Roukes, and J. P. Harbison, "Electrical Damage Induced by Ion Beam Etching of GaAs," *J. Vac. Sci. Technol.*, vol. B 6(1), pp. 277-279, Jan/Feb 1988.

97. H. F. Wong, D. L. Green, T. Y. Liu, D. G. Lishan, M. Bellis, E. L. Hu, P. M. Petroff, P. O. Holtz, and J. L. Merz, "Investigation of Reactive Ion Etching Induced Damage in GaAs-AlGaAs Quantum Well Structures," *J. Vac. Sci. Technol.*, vol. B 6(6), pp. 1906-1910, Nov/Dec 1988.

98. A. Henry, O. O. Awadelkarim, J. L. Lindstrom, and G. S. Oehrlein, "Electrical Studies on Plasma and Reactive-Ion-Etched Silicon," *J. Appl.*

Phys., vol. 66(11), pp. 5388-5393, 1 December 1989.

99. S. J. Pearton, U. K. Chakrabarti, and W. S. Hobson, "Reactive ion Etching Induced Damage in GaAs and AlGaAs Using $C_2H_6/H_2/Ar$ or CCl_2F_2/O_2 Gas Mixtures," *J. Appl. Phys.*, vol. 66(5), pp. 2061-2064, 1 September 1989.

100. S. W. Pang, G. A. Lincoln, R. W. McClelland, P. D. DeGraff, M. W. Geis, and W. J. Piacentini, "Effects of Dry Etching on GaAs," *J. Vac. Sci. Technol.*, vol. B 1(4), pp. 1334-1337, Oct.-Dec. 1983.

101. Yoshihiko Yuba, Tomohiro Ishida, Kenji Gamo, and Susumu Namba, "Characterization of Ion Beam Etching Induced Defects in GaAs," *J. Vac. Sci. Technol.*, vol. B 6(1), pp. 253-256, Jan/Feb 1988.

102. C. M. Knoedler, L. Osterling, and H. Shtrikman, "Reactive Ion Etching Damage to GaAs Layers with Etch Stops," *J. Vac. Sci. Technol.*, vol. B 6(5), pp. 1573-1576, Sep/Oct 1988.

103. S. W. Pang, "Surface Damage on GaAs Induced by Reactive Ion Etching and Sputter Etching," *J. Electrochem. Soc.: Solid-State Science and Technology*, vol. 133. No. 4, pp. 784-787, April 1986.

104. M. Tamura, S. Shukuri, and Y. Madokoro, "Two-Dimensional Distributions of Secondary Defects in Focused Ion Beam Implantation into Si," *J. Vac. Sci. Technol. B*, vol. 6(3), pp. 996-05, May/Jun 1988.

105. Qiang Guo, Ximao Bao, Jianming Hong, Yong Yan, and Duan Feng, "Implantation Damage and Anomalous Diffusion of Implanted Boron in Silicon," *Appl. Phys. Lett.*, vol. 54(15), pp. 1433-1435, 10 April 1989.

106. Tohru Hara, Shuya Takahashi, Hiroyuki Hagiwara, Jun Hiyoshi, W. Lee Smith, C. Welles, S. K. Hahn, L. Larson, and C. C. D. Wong, "Damage Formed by Ion Implantation in Silicon Evaluated by Displaced Atom Density and Thermal Wave Signal," *Appl. Phys. Lett.*, vol. 55(13), pp. 1315-1317, 25 September 1989.

107. C. Uzan-Saguy, D. Comedi, V. Richter, R. Kalish, and R. Triboulet, "Buildup of Ion Implantation Damage in $Hg_{1-x}Cd_xTe$ for Various x Values," *J. Vac. Sci. Technol.*, vol. A 7(4), pp. 2575-2579, Jul/Aug 1989.

108. A. Reisman, C. J. Merz, J. R. Maldonado, and W. W. Molzen, Jr., "Low Energy X-Ray and Electron Damage to IGFET Gate Insulators," *J. Electrochem. Soc.*, vol. 131(6), pp. 1404-1409, June 1984.

109. Masakazu Shimaya, Osaake Nakajima, Chisato Hashimoto, and Yutaka Sakakibara, "Reduction of Electron-Beam-Damage in MOS Devices Using Three-Layer Resist with Heavy Metal Interlayer," *J. Electrochem. Soc.*, vol. 131(6), pp. 1391-1395, June 1984.

110. J. R. Maldonado, A. Reisman, H. Lezec, C. K. Williams, and S. S. Iyer, "X-Ray damage Considerations in MOSFET Devices," *J. Electrochem. Soc.*, vol. 133(3), pp. 628-631, March 1986.

111. J. R. Maldonado, A. Reisman, H. Lezec, B. Bumble, C. K. Williams, and S. S. Iyer, "Thin Film Structure to Reduce Radiation Damage in X-Ray Lithography," *J. Vac. Sci. Technol. B*, vol. 5(1), pp. 248-05, Jan/Feb 1987.

112. G. A. Evans, N. W. Carlson, J. M. Hammer, M. Lurie, J. K. Butler, S. L. Palfrey, L. A. Carr, F. Z. Hawrylo, E. A. James, C. J. Kaiser, J. B. Kirk,

and W. F. Reichert, "Efficient 30 mW Grating Surface-Emitting Lasers," *Appl. Phys. Lett.*, vol. 51, pp. 1478-1480, 9 November 1987.

113. G. A. Evans, N. W. Carlson, J. M. Hammer, M. Lurie, J. K. Butler, S. L. Palfrey, R. Amantea, L. A. Carr, F. Z. Hawrylo, E. A. James, C. J. Kaiser, J. B. Kirk, W. F. Reichert, S. R. Chinn, J. R. Shealy, and P. S. Zory, "Coherent, Monolithic Two-Dimensional (10X10) Laser Arrays Using Grating Surface Emission," *Appl. Phys. Lett.*, vol. 53, pp. 2123-2125, 28 November 1988.

114. R. Fastow, R. Brener, R. Kalish, and M. Eizenberg, "Ion Beam Mixing of GaAs with Films of Al, Si, and their Nitrides," *J. Appl. Phys.*, vol. 63(8), pp. 2586-2590, 15 April 1988.

APPENDIX A:
EXPERIMENTAL OBSERVATION OF FIB INDUCED DAMAGE AND DAMAGE PROTECTION BY MEANS OF A Si_3N_4 DAMAGE "STOP" LAYER

A.1 Introduction

Target atoms bombarded with an incident Ga^+ ion of tens of kV acceleration potential can be displaced from their lattice sites. With different incident beam energies, the displacements can result in different collision effects, such as physical sputtering which predominates at the low energy range (< 30 keV) and ion implantation at higher energy ranges (> 60 keV). Whatever the effects are, however, ion beam induced damage will take place below the surface of the target. When modifications are made on semiconductor diode laser devices by FIB micromachining at submicron scale, such damage has to be investigated in order to be able to learn how to modify the devices properly, rather than destroy them.

Energetic ions can create damage in a DBR grating section of a semiconductor laser, because the primary ions cause collisions with lattice atoms along the penetration path. Miyake *et. al.*[91] had investigated defects induced by focused ion beam implantation in GaAs by means of deep-level transient spectroscopy (DLTS), C-V carrier profiling, and resistance measurements. It was observed that the DLTS spectra of Si and Ga FIB implanted samples annealed at temperatures up to 500 $°C$ were apparently identical to one another, while the energy of the focused ion beam was at 100 keV. Also the resistance increased by more than five orders of magnitude by Si and Ga FIB implantation due to the induced defects. However, it was restored to initial values after annealing at 600 $°C$, except for a sample of Ga implantation with a dose higher than $10^{14}/\mathrm{cm}^2$. It was concluded that for annealing of induced defects, there were no intrinsic problems for FIB implantation with a dose lower than $10^{13}/\mathrm{cm}^2$. Thus a measure for preventing such damage is needed, particularly in FIB micromachining.

When the aforementioned 3-D features (see chapter 4) were micromachined on the grating sections of DBR-GSE lasers, the lasing characteristics changed dramatically in terms of the increase of threshold currents and the decrease of output power. A series of experiments were then conducted by micromachining rectangles on the grating sections with different ion doses. At a very low ion dose ($< 7.3 \times 10^{14}\mathrm{ion}/\mathrm{cm}^2$), the degradation of laser devices was observed, which, indicates that FIBM is too destructive to serve as a milling tool for modifying the DBR-GSE laser diode arrays. A method for reducing the damage by means of a "stop" film deposited on top of the areas to be micromachined was found and will be described in section A.3.

A.2 Background

Before a high energy incident ion arrives at a final resting position within the substrate lattice, the ion will make multiple collisions (elastic or inelastic) with the lattice atoms and its energy will gradually decrease. This energy loss is transferred to the lattice atoms in the form of electronic excitation when there are inelastic contributions to the loss mechanism or in the form of kinetic energy of motion of the lattice atoms when the collisions are elastic. In the former case there will mainly be secondary electron emission[92,93], while in the latter one the struck atoms will be displaced from their equilibrium positions in the lattice. If the struck atoms received sufficient energy in the collision, the atom displacement will be big enough to carry it away from the influence of the immediately surrounding atoms; it could fly off the lattice into the vacuum chamber as in a sputtering process, or become a "foreign" atom elsewhere in the lattice, and cause atomic dislocation.

Since ion beam induced damage could be caused by atomic dislocation in the normal undisturbed lattice, it must be anticipated that the damage will result in observable changes in the macroscopic properties of the bombarded substrate. Therefore, one may expect to observe changes in thermal and electrical conductivity and changes in optical and mechanical properties of irradiated materials.

A.2.1 Evaluation of radiation damage

There are several methods to detect ion beam induced damage which can be found in the literature. In applications in the low energy range (<3 keV) such as ion-beam etching (IBE) and reactive-ion etching (RIE), many methods can be used including Raman scattering spectroscopy[94], photoluminescence (PL) spectroscopy[95], Auger electron spectroscopy (AES), cross-sectional transmission electron microscopy (TEM) analysis[96], and cathodoluminescence (CL) spectroscopy by using multiple quantum wells as *in situ* probes[97]. Two of the most common methods are current-voltage (I-V) and capacitance-voltage measurements on Schottky diodes, and deep-level transient spectroscopy (DLTS)[98-103]. In ion beam implantation in the high energy range (>60 keV), there are some other methods besides the above mentioned Schottky diodes, DLTS and TEM[91,104], such as secondary-ion mass spectroscopy (SIMS)[105] and channeling Rutherford backscattering spectrometry (RBS)[106,107]. However, there is not much research in the medium energy range (10 keV to 30 keV range, mainly FIB), except for life-tests of FIB micromachined output mirrors on transverse junction stripe lasers, and[36] characterization of subsurface damage using PL spectroscopy[72].

A.2.2 Damage protection layer

Radiation damage studies have been done in connection with e-beam and x-ray lithography[108-111] for more than a decade. Recently there have been increasing concerns about ion beam induced radiation damage in a wide spectrum of energies, from several hundred volts to more than one hundred thousand volts. It is possible to reduce or avoid damage by using a "stop" layer, which was discovered in the present study. As far as we know, in the FIBM technique, a damage "stop" layer has not been reported in literature yet. It appears that any material with very low sputtering yield will be suitable for making a radiation damage "stop" layer. There are some other requirements for the purposes of FIB micromachining diode laser devices, including laser light transparency and electrical insulation or dielectric properties to avoid short circuits between laser diode electrodes. Si_3N_4 was found to be suitable as a damage "stop" layer.

A.3 Experimental Observation of FIB induced damage on DBR-GSE diode lasers

It is important to investigate the FIB induced damage in order to apply FIB techniques more efficiently. A novel method to detect this type of damage has been developed using DBR-GSE diode laser arrays (see section A.3.2). While performing the FIB micromachining of various structures on DBR-GSE laser devices, lasing characteristics of some devices was degraded dramatically, but some of them were not. It was discovered that, on those devices which were not degraded there was a layer of Si_3N_4, which had been accidently not removed at the by David Sarnoff Research Center. Therefore, a protection layer of Si_3N_4 should be deposited on the top of substrates in order to prevent damage during alignment and observation of the wafer.

A.3.1 Experimental Setup

In order to investigate damage detection techniques, a damage-sensitive device is needed. DBR-GSE diode lasers have many useful properties for detecting FIB induced damage. The grating period is chosen so that the second diffraction order acts as a Bragg reflector in the wafer plane (which provides the optical feedback for laser oscillation), while the first order diffraction provides surface emission. The characteristics of such laser devices are very sensitive to the grating structure. Any damage to the grating section and the active region will change the laser characteristics or even destroy the laser itself.

A.3.1.1 DBR-GSE diode lasers

DBR-GSE diode laser arrays, manufactured by David Sarnoff Research Center[112,113], were chosen for this experiment. The structure of the DBR-GSE arrays used in our experiments is that of index-guided ridge lasers. At each end of the laser section there are second-order DBR grating sections with length of $300\mu m$ and period of 0.25 μm. The transverse structure in the gain and grating regions is a graded index separate confinement heterostructure single quantum well (GRINSCH SQW) geometry grown by metalorganic chemical vapor deposition in a single step.

The GRINSCH SQW structure[112], shown in Fig. A.1, consists of an n-GaAs substrate, an n-GaAs buffer layer ($0.01\mu m$), an n $-Al_{0.25}Ga_{0.75}As$ buffer layer ($0.01\mu m$), an n $-Al_{0.75}Ga_{0.25}As$ cladding layer ($1.2\mu m$), a graded region from n $-Al_{0.75}Ga_{0.25}As$ to n $-Al_{0.35}Ga_{0.65}As$ ($0.2\mu m$); a GaAs quantum well (50 Å), a second graded region from n $-Al_{0.35}Ga_{0.65}As$ to n $-Al_{0.75}Ga_{0.25}As$ ($0.2\mu m$), a p $-Al_{0.75}Ga_{0.25}As$ cladding layer ($1.2\mu m$), and a p-GaAs cap layer ($0.4\mu m$).

A.3.1.2 Output power measurement

In using a 25 keV Ga^+ ion beam, damage was only induced on one of the grating sections. A schematic diagram of the top view of a DBR-GSE diode laser device with five gain sections is shown in the Fig. A.2, where the FIB induced damage area is illustrated. Pulsed constant-current sources with a rise time of less than 20 ns were used to drive the laser gain sections. Pulse duration and duty cycle are 200 ns and 0.1 percent, respectively.

The focused ion beam was scanned in a raster fashion over the grating sections of the arrays, with various ion doses, in order to identify the threshold ion dose of the damage. The laser output power with respect to driving currents (L-I curves) of a laser array was measured before exposing it to the ion beam. The array was placed in the FIB system, as described previously,

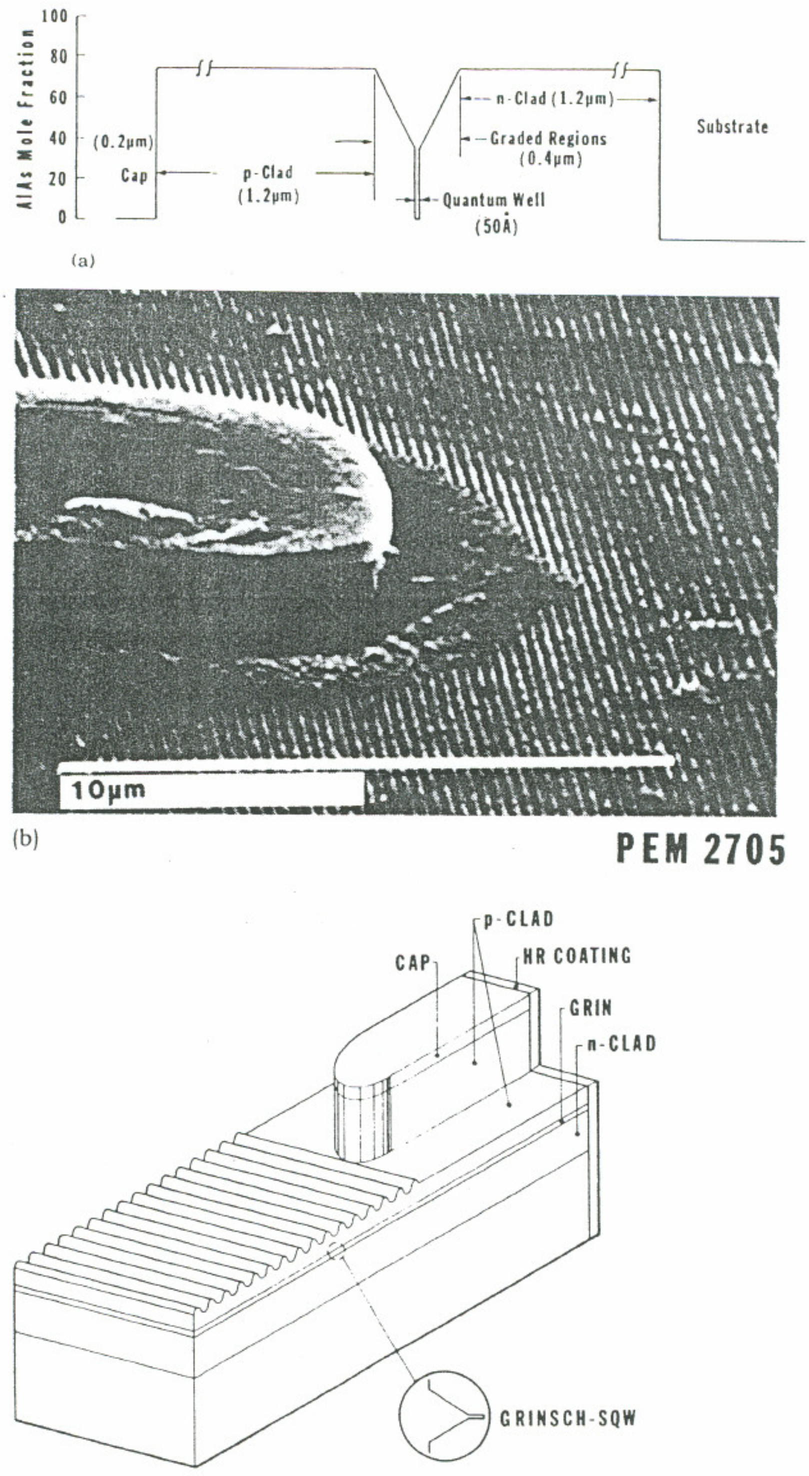

Figure A.1 (a) Upper: GRINSCH SQW structure. (b) Middle: scanning electron micrograph of the transition between the laser and passive waveguide sections. (c) Lower: schematic of the GRINSCH SQW surface-emitting laser. cf. Evans *et. al. Appl. Phys. Lett.*, vol. 51, pp. 1478-1480, 9 November 1987.

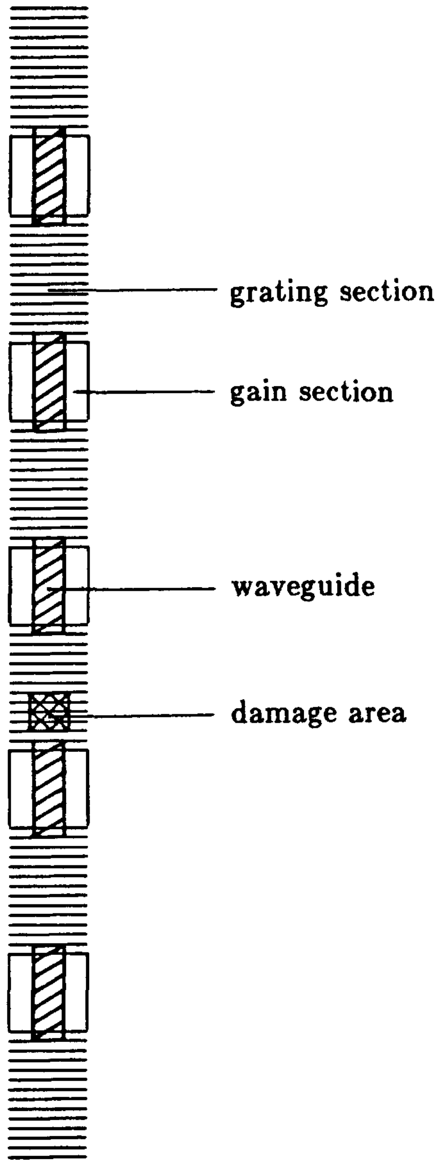

Figure A.2 Schematic diagram of the top view of a DBR-GSE diode laser device used to investigate the FIB induced damage, where grating section, gain section, waveguide and damage area are illustrated.

and dosed with a small amount of ions; then they were taken out of the vacuum chamber so that the power measurement could be performed to obtain the L-I curves. This array was then placed back into the FIB system, where it was exposed to an additional dose of ions so that the total ion dose is equal to the sum of these two exposures. The L-I curves were measured again and this procedure will be repeated many times, if necessary, until the L-I curves shows significant changes.

A.3.2 Experimental results of damage effects

A DBR-GSE diode laser array with five gain sections and six grating sections was used. From the L-I curve, the threshold current of this device was about 160mA. A low dose experiment with FIB micromachining was done with a 25 keV Ga^+ with 215pA probe current (measured in the blanking plates of the ion column) over a $116 \times 110\ \mu m$ area of gratings for 5 seconds. The equivalent ion dose was very small and equal to $D = \frac{Jt}{q} = 5.3 \times 10^{13}/\text{cm}^2$, with J the average current density, q the ion charge and t the exposure time (see section 5.3 in Puretz's dissertation). Under the above conditions, it often took two minutes to align a device for micromachining. No change in the device L-I curves was noted as shown in Fig. A.3. and no damage was detected.

Since the ion dosage was only on a small area of gratings, it is necessary to normalize the ion dose against entire gratings. The total number of ions

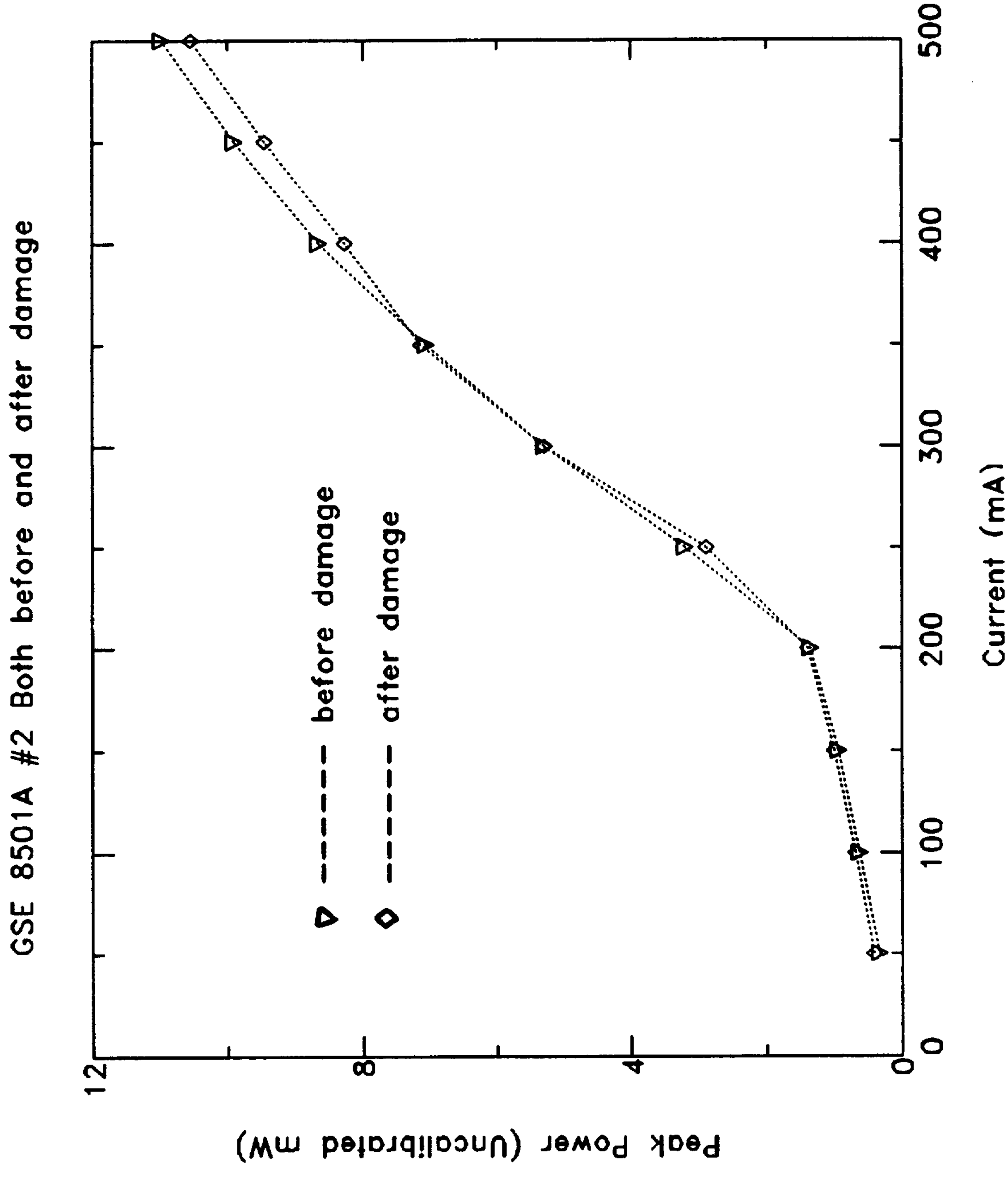

Figure A.3 L-I curve of a GSE laser array irradiated by low ion dose.

exposured to gratings was 6.7×10^9. But the waveguide is only $40\mu m$ wide, thus the actual damage area is $116 \times 40\mu m$. Therefore, the total number of ions, which could actually induce damage to the laser device, was $6.7\times10^9\times40\div110 = 2.44 \times 10^9$. Because there were six grating sections, the number of ions per grating section was 4.1×10^8/grating.

Another array with four gain sections and five grating sections was used for a high ion dose experiment. By measuring the output power and plotting the L-I curve, we found that the threshold current was about 370mA. After one of the grating sections was exposed with the same ion beam over the same exposure area as in the previous experiment, for 20 seconds (a factor of four greater of ion dose than was used in the previous experiment), a shift of the L-I curve to higher driving current was observed. At the same driving current, the threshold current jumped to 520mA and output power varied by $4mW$, as shown in Fig. A.4. However, the differential quantum efficiency of this device remained unchanged. The total number of ions was 2.7×10^{10}, the number of actual damage ions 9.8×10^9, and the number of actual damage ions per grating section 2.0×10^9/grating.

The array was returned to the FIB system, and the ion beam was scanned for another 10 seconds over the same area, so the total machine time on this device was 30 seconds. The total number of ions was 4.1×10^{10}, the number of actual damage ions 1.5×10^{10}, and the number of actual damage ions per grating section 3.0×10^9/grating. A small shift of the L-I curve was seen. As a result, the threshold current was changed by a small amount to 550mA, but the differential quantum efficiency was still the same, as shown in

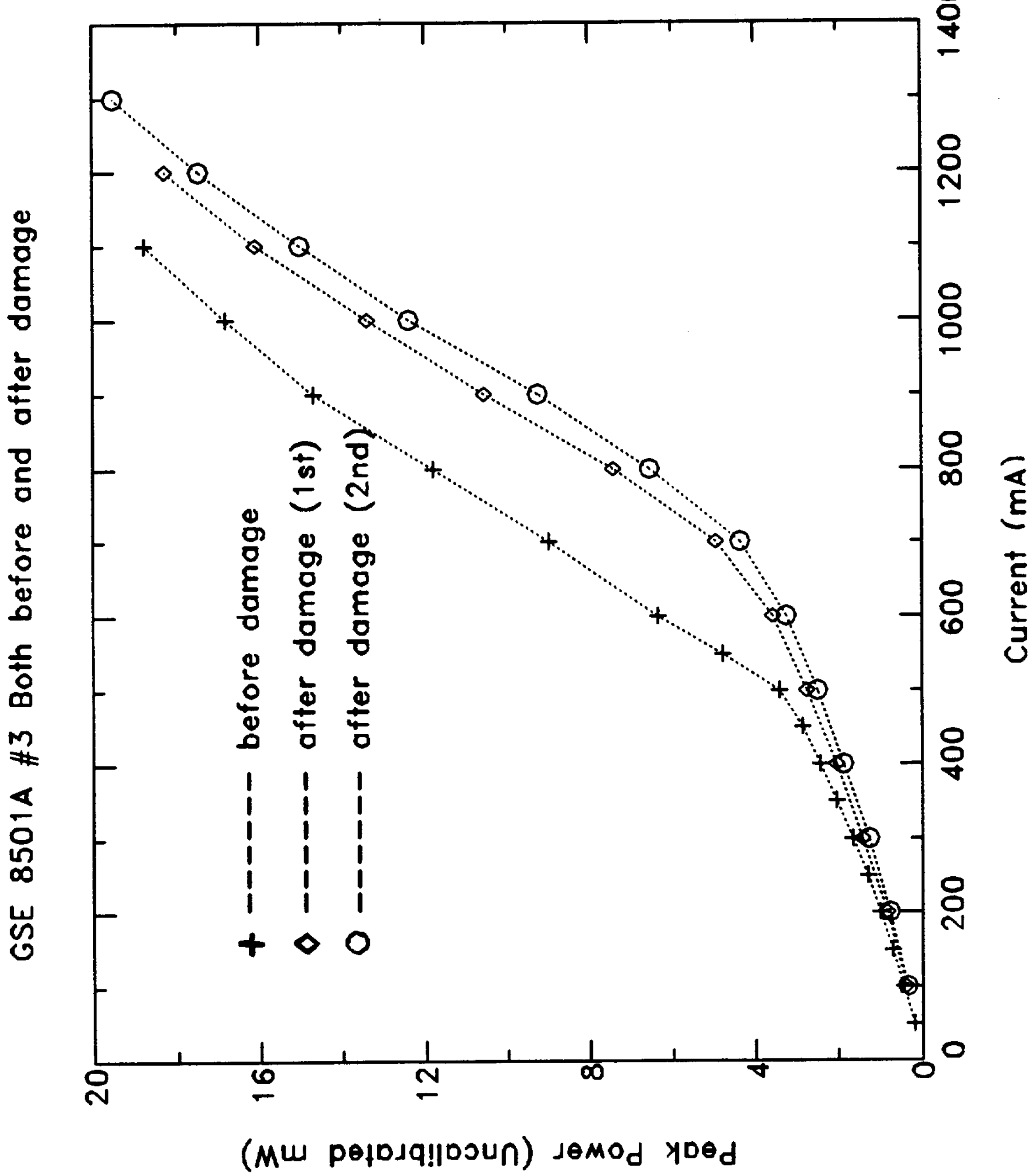

Figure A.4 L-I curve of a GSE laser array irradiated by high ion dose.

Fig. A.4.

The effects of FIB induced damage on the grating sections have been investigated with regard to threshold currents, output power levels, and differential quantum efficiency. After the ion dose reached a certain point, the FIB induced damage could be detected by observing the degradation of the laser performance. Shifts of L-I curves to higher driving currents have been observed. Note that the L-I curves do not change much after the ion dose exceeds the threshold. Because the damaged area in the grating section is very small ($100\mu m \times 40\mu m$) in comparison with total area of the grating sections, the change of the surface emitted laser light power from the damaged gratings would not affect the L-I curve of the entire laser array. In conclusion, the threshold number of ions per grating of such laser device is between 4.1×10^8/grating to 2.0×10^9/grating.

A.3.3 Experimental results of damage protection effects by Si_3N_4

As an analogy to the electron-beam "stop" layer in electron-beam lithography, we utilize a layer of Si_3N_4 as a focused ion beam induced damage "stop" layer for fabrication of various kinds of semiconductor diode lasers using FIB techniques.

To investigate the protective ability of a Si_3N_4 layer, a five gain section (six grating section) DBR-GSE diode laser array with a layer of Si_3N_4 deposited on the top of the grating sections was irradiated by a focused 25 keV Ga^+ ion beam scanning over an area ($55 \times 54\mu m$) in one of the grating sections. The beam current at the target was 220pA, and the machining time was 6 minutes and 24 seconds, so that the ion dose was $1.78 \times 10^{16}/cm^2$. The total number of ions was 5.28×10^{11}, the number of actual damage ions 4.0×10^{11}, and the number of actual damage ions per grating 6.7×10^{10}/grating. A lasing characteristics calibration test of this array was carried out before the FIB damage experiment, in which a threshold current of 260mA is observed.

After the first ion dose, there was no significant change in L-I curves, as shown in Fig. A.5. This grating section was then exposed for 60, 30 and then 60 seconds. After each exposure, an L-I curve measurement was made, while the total ion dose was $2.4 \times 10^{16}/cm^2$. The total number of ions was 7.34×10^{11}, the number of actual damage ions 5.44×10^{11}, and the number of actual damage ions per grating 9.1×10^{10}/grating. The basic characteristics of this array were not altered significantly, as shown in L-I curves of Fig. A.5, which indicated that there had been no damage induced by FIB occurred in the presence of the Si_3N_4 protection layer.

A.4 Conclusions

From FIB induced damage experiments with a 25 keV Ga^+ ion beam, at the threshold number of ions per grating between 4.1×10^8/grating to 2.0×10^9/grating, a threshold ion dose for FIB induced damage on the DBR-GSE diode laser arrays could be found. The resolution of our damage detec-

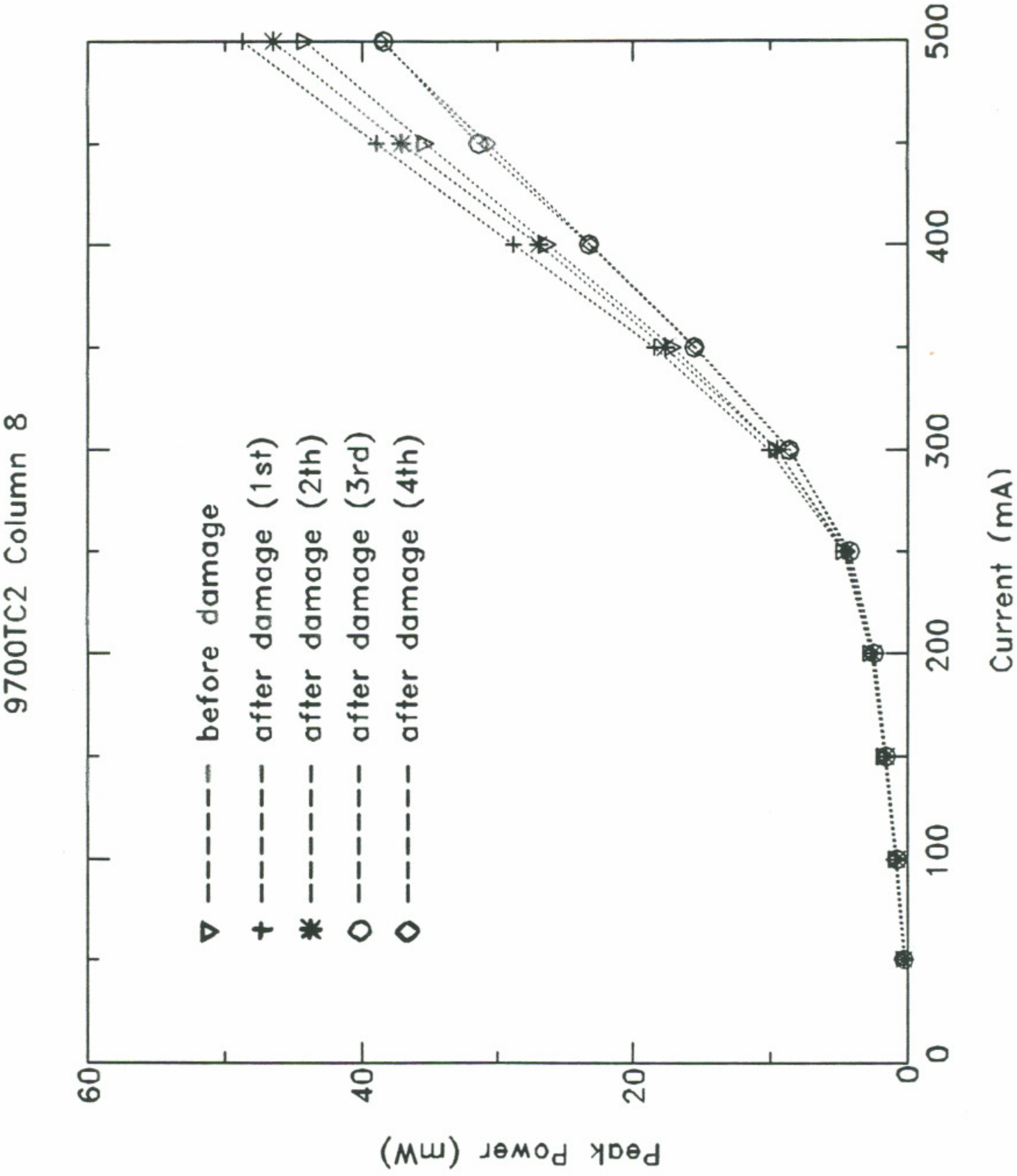

Figure A.5 L-I curve of a GSE laser array, with a layer of Si_3N_4 deposited by DSRC on the top of the grating sections, irradiated by very high ion dose.

tion technique is limited by this threshold ion dose.

When a Si_3N_4 "stop" layer was used, the number of up to 9.1×10^{10}/grating ions did not induce any damage which could be detected by DBR-GSE diode lasers technique. Therefore, according to this result, the Si_3N_4 "stop" layer could protect the laser array from damage for at least $91.0/2.0 = 45$ times more ion dose than that without using a "stop" layer.

A.5 Speculations

Low sputtering yield of Si_3N_4 could probably be used to explained the mechanism for protecting against FIB induced damage, especially for GaAs/AlGaAs semiconductor laser materials. The subsurface damage induced by FIB has been investigated by Taneya *et al*[72], with Ga^+ focused ion-beam-assisted Cl_2 etching. The photoluminescence intensity of a damaged sample[72] decreased to $1/30-1/40$ of that of an undamaged sample, with an ion dose of $8 \times 10^{15}/cm^2$. Taneya *et al* discovered that the damaged layer thickness is $0.7\mu m$ at least, which is much larger than the ion range (about $0.01\mu m$ for 10 keV Ga^+ beam). For a Si_3N_4 "stop" layer, a dose of up to $2.4 \times 10^{16}/cm^2$ ion did not induce any damage which could be detected by the DBR-GSE diode lasers technique. Therefore, Si_3N_4 presumably has some special properties other than low sputtering yield.

The properties of Si_3N_4 material has been studied in detail, especially ion beam mixing[114]. The ion beam interfacial mixing has been studied by

Fastow *et. al.*[114] by implanting silicon ions in thin films of Al, AlN, Si, and Si_3N_4 deposited on GaAs substrates, while the ion dose was as high as $1.6 \times 10^{17} Si^+/cm^2$ at energies between 200 and 250 keV. Fastow *et. al.* concluded that small or negligible mixing, measured by Rutherford backscattering spectrometry and Auger depth profiling, would occur in the AlN/GaAs and the Si_3N_4/GaAs systems, presumably because of strong nitrogen bonding in these layers. This suggested that any effect induced by incident silicon ions, at the interface of the thin films and GaAs substrates could be reduced because of the presence of Si_3N_4.

APPENDIX B

Source code of programs used to fabricate shallow gratings, "V", micro-"V" and parabolic turning mirror will be given in Appendix B. The basic structure of these programs is as follows: the bit addresses of the 12-bit DAC's were calculated according to certain beam scab strategies, then two instructions would be issued by the computer to the 12-bit DAC's, which could send appropriate voltage signals to the x and y channels of the ion beam deflector. The instructions used to control the DAC's are the only machine dependent commands in the above-mentioned programs.

Positions of the ion beam are controlled by a Heathkit (H-207) computer with a 12-bit 4-channel D-A converter (AOM-12). The deflecting voltages in both x and y channels can be changed between -5.0 V and +5.0 V by the 12-bit DAC's with input data between 0 to 4096, respectively.

```
/*------------------------------
| circle.c
| mill a circle grating
------------------------------*/

#include <stdio1.h>

main()
{

    extern int scanf();
    extern double sin(), cos();

    double r, angle, inc;
    int x, y;
    int xh, xl, yh, yl;
    int i, n, itime, ttime;

    outportb(85,192);       /*toggle relays to DACS*/

    printf("Input scan time=");
    scanf("%d",&ttime);
    printf("Scan time=%d\n",ttime);

    printf("Begin milling process!\n");
    outportb(12,0);         /* unblank beam */

    for(itime = 0; itime < ttime; itime++)
    {
        for(r = 256.; r < 1792.; r = r + 64.)
        {
            inc = 8. / r;
            for(angle = 0.; angle < 6.2831853; angle = angle + inc)
```

```
                {
                 x = r * cos(angle) + 2048;
                 y = r * sin(angle) + 2048;
                 xh = x / 256;
                 xl = x - xh * 256;
                 yh = y / 256;
                 yl = y - yh * 256;
                 outportb(0x9,xl);  /* x scan */
                 outportb(0x8,xh);
                 outportb(0xB,yl);  /* y scan */
                 outportb(0xA,yh);
              }
          }
     }
     outportb(12,12);        /* blank beam */
}
```

```
/*-------------------------------------
| grating.c
| a grating with eight grooves
| used to machine grooves in
| Fig. 4.2, 4.5, and 4.12
-------------------------------------*/

#include "stdio1.h"

main()
{
    unsigned int rtime, xhi, xlo, yhi, ylo;

    outportb(85,192);/* toggle relays to DACs */
    outportb(12,0);     /* unblank the ion beam */

    for(rtime = 1; rtime < 600; ++rtime)  /* scan time */
    {
        for(xhi = 4; xhi < 12; ++xhi)
        {
            xlo = 0;
            outportb(0x9,xlo);  /* x scan */
            outportb(0x8,xhi);
            for(yhi = 0;yhi < 16; ++yhi)
            {
                for(ylo = 0;ylo < 256;ylo=ylo+4)
                {
                    outportb(0xB,ylo);  /* y scan */
                    outportb(0xA,yhi);
                }
            }
        }
    }
    outportb(12,12);  /* blank the ion beam */
}
```

```
/*----------------------------------------
| line45.c
| used to fabricate 45 TIR
| turning mirrors
| single line scans
----------------------------------------*/

#include "stdio1.h"

main()    /* draw a line in one scan */
{
    unsigned int xlo, xhi;
    unsigned int rtime, ttime;

    printf("Input scan time=");
    scanf("%d",&ttime);
    printf("Scan time = %d\n",ttime);

    outportb(85,192);       /*toggle relays to DACS*/
    outportb(12,0);         /* unblank beam */

    for(rtime = 0; rtime < ttime; rtime++) /* scan time */
    {
        for(xhi = 1; xhi < 15; ++xhi)
            for(xlo = 0; xlo < 256; xlo = xlo + 2)
            {
            outportb(0x8,xlo);   /* x scan */
            outportb(0x9,xhi);
            outportb(0xB,xlo);   /* y scan */
            outportb(0xA,xhi);
            }
     }
     outportb(12,12);       /* blank beam */
}
```

```
/*------------------------------------------------------
| para1r.c
| used to fabricate parabolic mirror
| this is second part of the program
| it will read the pre-calculated
| look-up table
| first part of data generator
| is called para1w.c
| xwnm.out means xh starts form n to m
| for para1.dat dimension is 1214
--------------------------------------------------------*/

#include <stdio1.h>

main()
{
    extern int scanf(), fscanf();
    FILE *inf;

    int xh[1214], xl[1214], yh[1214], yl[1214];
    int i, itime, ttime;
    char *name, string[80];

    printf("Input scan time=");
    scanf("%d",&ttime);
    printf("Scan time=%d",ttime);

    outportb(85,192);        /*toggle relays to DACS*/
    inf = fopen("para1.dat","r");  /* open a data file */

    printf("\nBegin read data!\n");
    for(i = 0; i < 1214; i++)
        fscanf(inf,"%d %d %d %d\n",&xh[i],&xl[i],&yh[i],&yl[i]);

    printf("Begin milling process!\n");
```

```
        outportb(12,0);        /* unblank beam */

    for(itime = 0; itime < ttime; itime++)
    {
        /* scan ion beam along arc */
         for(i = 0; i < 1214; i++)
        {
            outportb(0x9,xl[i]);  /* x scan */
            outportb(0x8,xh[i]);
            outportb(0xB,yl[i]);  /* y scan */
            outportb(0xA,yh[i]);
        }
        /* scan ion beam along arc in a reserve way*/
         for(i =1213; i >= 0; i--)
        {
            outportb(0x9,xl[i]);  /* x scan */
            outportb(0x8,xh[i]);
            outportb(0xB,yl[i]);  /* y scan */
            outportb(0xA,yh[i]);
        }
    }
    outportb(12,12);      /* blank beam */
}
```

```
/*------------------------------
| para1w.c
| with constant scan
| along arc machining
| a parabola
| write a look-up table
| in heath machine
| second part of this
| program is para1r.c
--------------------------------*/

#include <stdio1.h>

main()
{

    extern double sqrt();

    FILE *outf;

    double ratio, f, a, a4, a2, arc;
    double xend, xst, yst, xm, ym, x, y, aconst;
    int xh, xl, yh, yl;

    outf = fopen("para1.dat","w");

    ratio = 4095./60.;
    f = 107.;
    a = 1./(4.*f);
    a4 = 1./f;
    a2 = 1./(2.*f);
    arc = 0.07;

    /* x must be increasing. */
    xst = 184.;
```

```
        xend = 244.;

    /* generate look-up table for paralr.c */
    do
    {
        yst = a*xst*xst;
        x = (xst - 184.)*ratio;
        y = (yst - 79.1)*ratio;
        tr(x,&xh,&xl);
        tr(y,&yh,&yl);
        fprintf(outf,"%d %d %d %d\n",xh,xl,yh,yl);

        aconst = arc/sqrt(1. + a4*yst);
        xm = xst + aconst;
        ym = yst + a2*xst*aconst;
        xst = xm;
        yst = ym;
    }
    while(xm < xend);

}

tr(x,h,l)

double x;
int *h, *l;

{
    *h = x/256.;      /* high bit of DACs */
    *l = x - *h * 256; /* low bit of DACs */
}
```

```
/*----------------------------------------------
| twos45.c
| fabricate a 45 slant deflecting mirror
| with better vertical wall and
| smoother surface using
| FEI two-lens ion gun which has 500 A
| resolution
----------------------------------------------*/

#include "stdio1.h"

main()    /* draw a rectangular in one scan */
{
    unsigned int limit, width, xhi, xlo, yhi, ylo;
    unsigned int rtime, ttime;

    printf("Input scan time =");
    scanf("%d",&ttime);
    printf("Scan time = %d\n",ttime);

    outportb(85,192);        /*toggle relays to DACS*/
    outportb(12,0);          /* unblank beam */

    for(rtime = 0; rtime < ttime; rtime++)
    {
        limit = 13;
        for(width =  0; width < 8; width++)
        {
            limit--;
            for(xhi = 4; xhi < limit; xhi++)
                for(xlo = 0; xlo < 256; xlo = xlo + 16)
                {
                    outportb(0x9,xlo);
                    outportb(0x8,xhi);
                    for(yhi = 0; yhi < 16; yhi++)
```

```
                        for(ylo = 0; ylo < 256; ylo = ylo + 16)
                      {
                         outportb(0xB,ylo);
                         outportb(0xA,yhi);
                      }
                 }
            }
        }
        outportb(12,12);       /* blank beam */
}
```

```
/*------------------------------
| vline.c
| fabricate "V" mirror
------------------------------*/

#include "stdio1.h"

main()    /* draw a line in one scan */
{
    unsigned int value4, value5, value2, value3;
    unsigned int rtime, ttime;

    printf("Input scan time=");
    scanf("%d",&ttime);
    printf("Scan time = %d\n",ttime);

    outportb(85,192);       /*toggle relays to DACS*/
    outportb(12,0);         /* unblank beam */
    for(rtime = 0; rtime < ttime; rtime++)
    {
        for(xhi = 1; xhi < 8; xhi++)
            for(xlo = 0; xlo < 256; xlo = xlo + 2)
            {
              outportb(0xB,xlo);   /*y scan */
              outportb(0xA,xhi);
              outportb(0x9,xlo);   /* x scan */
              outportb(0x8,xhi);
              }
         for(xhi = 1; xhi < 8; xhi++)
              for(xlo = 0; xlo < 256; xlo = xlo + 2)
              {
              outportb(0xB,xlo);    /* y scan */
              outportb(0xA,7+xhi);
              outportb(0x9,254-xlo); /* x scan 254 based on 2 */
              outportb(0x8,8-xhi);
```

```
            }
    }
    outportb(12,12);      /* blank beam */
}
```

```
/*------------------------------
| vlinem.c
| fabricate micro-"V"
| turning mirror
-------------------------------*/

#include "stdio1.h"

main()    /* draw a line in one scan */
{
    unsigned int xhi, xlo;
    unsigned int rtime, ttime;

    printf("Input scan time=");
    scanf("%d",&ttime);
    printf("Scan time = %d\n",ttime);

    outportb(85,192);        /*toggle relays to DACS*/
    outportb(12,0);          /* unblank beam */
    for(rtime = 0; rtime < ttime; rtime++)
    {
        for(xhi = 3; xhi < 13; xhi = xhi + 2)
        {
            for(xlo = 0; xlo < 256; xlo = xlo + 2)
            {
                outportb(0xB,xlo);   /* y scan */
                 outportb(0xA,xhi);
                 outportb(0x9,xlo);   /* x scan */
                 outportb(0x8,7);
            }
            for(xlo = 0; xlo < 256; xlo = xlo + 2)
            {
                outportb(0xB,xlo);    /* y scan */
                outportb(0xA,1+xhi);
                outportb(0x9,254-xlo);  /* x scan 254 based on 2 */
```

```
                outportb(0x8,7);
            }
        }
    }
    outportb(12,12);     /* blank beam */
}
```

VITA

Hongyu Ximen was born in Beijing, China on June 15, 1963. He received the Bachelor of Science degree in Mechanical Engineering from Peking University in Beijing, China, in July, 1985. In September 1985, he began his studies at Oregon Graduate Institute of Science and Technology and completed requirements for his Ph.D degree in Applied Physics in 1990.